COMPUTATIONAL MODELING
OF CONCRETE FRACTURE

J.G. ROTS

COMPUTATIONAL MODELING OF CONCRETE FRACTURE

COMPUTATIONAL MODELING OF CONCRETE FRACTURE

PROEFSCHRIFT

ter verkrijging van de graad van doctor aan de Technische Universiteit Delft, op gezag van de Rector Magnificus, prof. drs. P.A. Schenck, in het openbaar te verdedigen ten overstaan van een commissie door het College van Dekanen daartoe aangewezen, op maandag 26 september 1988 te 16.00 uur

door

JAN GERRIT ROTS

geboren te Aalten
civiel ingenieur

Dit proefschrift is goedgekeurd door de
promotor: Prof. dr. ir. J. Blaauwendraad

ACKNOWLEDGEMENTS

STELLINGEN

1

De onderstelling van verplaatsingscontinuïteit bij het modelleren van geometrische *dis*continuïteiten is een kunstgreep die leidt tot opgesloten spanningen binnen een eindige elementen configuratie. De consequenties zijn tot op heden onderschat en wettigen een herwaardering van het discrete scheurconcept.

2

Bij constructies met herverdeling van krachtswerking - bijvoorbeeld via stelsels van drukbogen met trekbanden - is een interpretatie in hoofdspanningen te verkiezen boven een interpretatie in schuifspanningen. Dit bepaalt het succes van scheurmodellen in het roterende hoofdassenstelsel (impliciete schuifterm) ten opzichte van scheurmodellen in een gefixeerd assenstelsel (expliciete schuifterm).

3

Numerieke simulaties onthullen dat de breuk in de 'directe mode II proef' van Bazant en Pfeiffer noch direct, noch van het type mode II is.
Bazant Z.P., Pfeiffer P.A., RILEM Mat. & Struct. 19, 111-121 (1986)

4

Binnen de hedendaagse stapelmechanica voor metselwerk en prefabconstructies is - vanwege de voorkeursrichting, bepaald door de voegen - het discrete scheurconcept met vooraf gedefiniëerde scheurvlakken bij uitstek toepasbaar.

5

DIANA is een bundelend programma, meer dan een kapstokprogramma. Voortzetting van de ontwikkeling van dit programma binnen een netwerk van samenwerkingsverbanden stelt hoge technische en organisatorische eisen teneinde te voorkomen dat flexibiliteit ontaardt in bureaucratie, modulariteit in versnippering en continuïteit in incompatibiliteit.

6

Technologiebeleid fixeert zich op marktgerichte toepassingen en heeft te weinig oog voor het op termijn instandhouden van de technisch-wetenschappelijke infrastructuur (onderhoud, beheer en ontwikkeling van basisgereedschap).

7

De kracht van geavanceerd numeriek gereedschap voor de civieltechnische construc-
tieleer ligt in de toepassing voor bijzondere constructies, het ondersteunen van expe-
rimenteel onderzoek en het onderbouwen van voorschriften. Voor toepassingen in de
bouwpraktijk van alledag zijn relatief eenvoudige elementtypen en modellen met een
beperkt aantal invloedsparameters gewenst.

8

Het toenemend specialistische karakter van de numerieke mechanica in combinatie
met de teruglopende studieduur wettigt een onderzoek naar nieuwe vormen van ken-
nisoverdracht, zoals expertsystemen en gidsen welke de incidentele gebruiker
adviseren bij het uitvoeren van elementenmethode-berekeningen.

9

Schuurman overschat in zijn cultuurfilosofische analyse de rol van wetenschappers en
technici. Zij krijgen zo te veel de schuld van de negatieve aspecten in de ontwikkeling
van de cultuur. Cultuurkritiek dient zich te richten op het onzorgvuldig introduceren
en te materialistisch consumeren van de produkten van wetenschap en techniek.
Schuurman E., Techniek: middel of moloch?, 2e druk, Kok, Kampen (1980)

10

Auteurslijsten van publicaties uit samenwerkingsverbanden dreigen lang te worden,
danwel in gebreke te blijven. Het bereikte compromis is meer een weerspiegeling van
psychologische eigenschappen en ambities van onderzoekers en managers, dan een
gewogen rangschikking van hun wetenschappelijke inbreng.

11

De randvoorwaarden zijn belangrijker bij congressen dan bij trekproeven aan beton.

J.G. Rots
Delft, 26 september 1988

CONTENTS

1. INTRODUCTION

1.1 Aims and scope

Fracture is one of the pressing issues in modeling civil engineering materials like concrete, mortar, brick, rock and clay. The pursuit of genuine fracture properties has posed a continuous challenge to materials scientists, and, to date, we observe that the pool of data on properties like tensile strength and fracture energy still extends. As a fruitful result hereof, a significant number of *constitutive models* has been put forward which set out to describe the material behavior under tensile loading.

Despite these efforts, the number of constitutive models that has been implemented successfully into computational simulators is relatively small. This is not only due to the inherent complexity of the problem, involving brittleness and softening, but also to the lack of clearness in the mechanics of *crack concepts* in which constitutive models are embedded. The proposed approaches range from discrete crack concepts, either with or without remeshing, to various types of smeared crack concepts, either with fixed or with rotating fracture planes. In many cases, the computational outcome turns out to depend not only on the constitutive model inserted into the concept, but also on the merits and demerits of the concept itself. An example is the disease of the smeared crack concept to generate spurious stresses, which affect the final result irrespective of the constitutive model applied. And even if the analyst has the disposal of sophisticated concepts and rational constitutive models, he may loose the achievements thereof by shortcomings of the *computational setting* in which they are implemented. For instance, misuse of finite element formulations and solution strategies may disturb the final result, especially if softening is involved.

Above three key notions have been introduced: constitutive models, crack concepts and computational aspects. It is the intent of this study to clarify a part of the relations between them. To this end, models and concepts will be reviewed, developed and embedded in a finite element environment, the integrated result of which will be judged for research problems as well as practical engineering problems.

Attention is focused on localized failure of the material under tension and tension-shear conditions without significant lateral compression. In such cases the cohesive properties of the material dominate over the frictional properties and the corresponding failure mode exhibits fracture in the form of separation bands rather than friction along shear bands. Furthermore, attention will be confined to concrete, although fracture in mortar, brick, rock and other cohesive materials can be analyzed along similar lines.

1

The central theme in the tensile fracture of a cohesive matrix-aggregate composite like concrete is its tension-softening behavior, which means that the load-displacement characteristics of a representative material volume exhibit a descending branch after peak-load. This phenomenon is due to progressive micro-cracking, tortuous debonding and other processes of internal damage, eventually coalescing into a traction-free macroscopic fracture plane. A major consequence of softening is that the material can neither be assumed to behave elastic-perfectly plastic nor elastic-perfectly brittle. Instead, we must utilize an elastic-softening formulation, which was first recognized by Hillerborg et al.[Hill 76] and Bazant & Oh[Baza 83a]. The theory has now advanced to the stage at which the basic possibilities and limitations are gradually becoming clear. Demonstrations thereof will be presented in this thesis.

A second feature of concrete and similar materials is their capability to transmit shear forces across the rough crack surfaces due to interlocking of the aggregate particles. In a numerical model the allowance for shear tractions across cracks involves that the axes of principal stress may rotate after crack formation. Here, the model of shear retention for fixed cracks has been widely accepted, but it begins to emerge that this may overestimate strength and stiffness during the fracture process. As a remedy, strategies have been put forward which provide for multi-directional cracks or rotating cracks, but to date their performance for softening conditions of tension-shear has remained largely unexplored. A purpose of the present study is to scrutinize this issue.

In structural practice, fracture is of course highly undesirable. As a remedy, designers frequently stabilize concrete structures by adding reinforcement. The underlying idea is that, while the concrete softens, the reinforcement compensates for the loss of tensile load carrying capacity via bond between concrete and reinforcing bars. Most existing tools for the analysis of concrete structures adopt the assumption of overall perfect bond. For problems of localized fracture, this assumption is unsafe and techniques that incorporate local bond-slip are required. Some work has been done in this area, but a consistent combination with novel tensile softening models is lacking. A third principal objective of the present study is to rejuvenate bond-slip research with the achievements of elastic-softening fracture mechanics.

1.2 Contents

The thesis starts with an overview of crack concepts for numerical analysis. After introducing a concept of discrete cracks with predefined orientations, the main part of the chapter is directed towards smeared concepts, which conceive the cracked solid to be a continuum. The treatment puts fixed, fixed multi-directional and rotating cracks into the same framework.

Chapter 3 addresses constitutive models for fracture of cohesive materials. A transparent model is obtained by assuming elasticity for the solid material and softening for the crack, which corresponds to an elastic-softening formulation for the cracked material. Particular forms of tension-softening and shear-retention functions are put forward for fixed, multi-directional as well as rotating cracks. The performance hereof is investigated for a tension-shear model problem that covers stress rotation beyond fracture.

Chapter 4 aims at formulating guidelines for use of finite elements in fracture analysis. Several computational aspects of smeared crack analysis are addressed, the most important of which are the danger of spurious kinematic modes and stress-locking as a consequences of displacement compatibility. For discrete cracking and bond, the chapter compares two classes of interface elements, comprising lumped and continuous representations of the interface.

The remaining part of the thesis is concerned with an investigation of the possibilities and limitations of the three tools (concepts, models and finite element discretizations) for predicting structural fracture.

Chapter 5 explores the possibilities and limitations of tension-softening models for simulating uncurved mode-I separation bands in plain concrete. Cases of direct tension as well as indirect tension are scrutinized and conclusive comments are made on the crucial issue as to whether there exists a sound set of elastic-softening properties for predicting mode-I type fracture.

Chapter 6 is devoted to curved mode I fracture in plain concrete. The misalignment of the lines of the mesh with the lines of the fracture involves local mode II shear effects. The axes of principal stresses will consequently rotate, which asks for a careful examination of the performance of the various crack concepts. The examination is focused on two illustrative examples and leads to surprising conclusions.

Chapter 7 broadens the scope of the study by adding reinforcement. It presents three approaches of decreasing degree of precision towards fracture and bond in reinforced concrete. First, the micro-mechanisms in the vicinity of a reinforcing are resolved from the viewpoint of fracture mechanics. Next, the bond-slip behavior obtained is lumped into interface elements, which consider the problem at an intermediate level with a view to predicting the spacing and width of localized cracks in reinforced members. Finally, a brief excursion is made into the field of distributed fracture for diffusely reinforced concrete.

Chapter 8 completes the study with two examples, integrating the aspects of crack concepts, softening models and bond. One example involves the simulation of a deep beam, whereas the other relates to an anchorage problem of engineering practice.

2. CRACK CONCEPTS

Crack concepts can be categorized into discrete concepts and smeared concepts. The former approach models a crack as a geometrical discontinuity, whereas the latter imagines a cracked solid to be a continuum. This chapter reviews and develops both approaches with prime attention to the class of smeared crack concepts. The treatise is given in incremental form using matrix-vector notation, whereby we consider the general case of a three-dimensional configuration. Whenever stiffness moduli appear, their meaning will remain abstract since the correlation with the underlying material properties is postponed until the next chapter.

2.1 Discrete crack concept

In the early days of finite element analysis cracks were modeled by means of a separation between element edges[NgoS 67,Nils 68]. The approach suffers from two drawbacks. First, it implies a continuous change in nodal connectivity, which does not fit the nature of the finite element displacement method. Secondly, the crack is constrained to follow a predefined path along the element edges, which puts doubts on the fidelity of the approach. The drawbacks are generally considered to be serious and attempts to eliminate them have been reported only sporadically. Prominent amongst these are the introduction of graphics-aided algorithms of automatic remeshing[Ingr 85a] and of techniques which permit discrete cracks to extend through finite elements[Blaa 81,Blaa 85]

A class of problems exists, however, whereby the orientation of the discrete crack is not necessarily the prime subject of interest. One may think of mode I fracture in the form of a straight separation band, the location of which is known in advance, or of discrete cracks along the interface between concrete and reinforcement. Furthermore, engineering problems exist whereby a mechanism of discrete cracks can be imagined to occur in a fashion similar to yield line mechanisms. For such cases, the above drawbacks vanish and one may use a simple form of discrete cracks with a predefined orientation.

In this study numerical experiments will be undertaken using a concept of predefined locations of potential cracking. To this end, interface elements are incorporated within the original mesh. The initial stiffness of the elements is assigned a large dummy value in order to simulate the uncracked state with rigid connection between overlapping nodes. Upon violating a condition of crack initiation, for instance a maximum stress condition, the element stiffness is changed and a constitutive model for discrete cracks is mobilized.

Defining a vector Δu which monitors the incremental relative displacement between two points of separation, and considering the (very small) initial displacements as elastic deformation, we decompose this vector into an elastic part Δu^{el} and a part Δu^{cr} that is associated with the crack displacements,

$$\Delta u = \Delta u^{el} + \Delta u^{cr} \tag{2.1}$$

For a two-dimensional configuration the relative displacement vectors consist of a mode I opening component and a mode-II sliding component, while a mode III sliding component is added in case of a third dimension. In a similar fashion, the tractions between two separated surfaces are assembled in a vector Δt, comprising a mode I traction and mode-II and/or mode-III shear tractions.

The tractions are related to the elastic relative displacements by

$$\Delta t = C^{el} \Delta u^{el} \tag{2.2}$$

where C^{el} represents the initial stiffness at locations of potential cracking. When cracking is mobilized, they are similarly related to the crack displacements by

$$\Delta t = C^{cr} \Delta u^{cr} \tag{2.3}$$

where C^{cr} represents phenomena like tension-softening and aggregate interlock. Combining (2.1), (2.2) and (2.3) yields

$$\Delta t = [C^{el} - C^{el}[C^{el} + C^{cr}]^{-1}C^{el}]\Delta u \tag{2.4}$$

which serves as a simple framework for constitutive relations of discrete cracks.

In this study the above formulation has been pursued to perform comparative studies with smeared crack approaches. Other capabilities relate to the possibility of predefining the potential cracks not only at a limited number of locations, but anywhere in between the solid elements. The resulting configuration then corresponds to a set of elastic blocks bonded together by potential discrete cracks and the fracture is allowed to propagate anywhere in between the blocks. This approach resembles the distinct element method pioneered in geomechanics[Cund 79] and gaining popularity in fracture research[Roel 85,Baza 86b,Lori 87].

2.2 Smeared crack concept

2.2.1 Essentials

The counterpart of the discrete crack concept is the smeared crack concept, in which a cracked solid is imagined to be a continuum. The approach, introduced by Rashid[Rash 68], starts from the notion of stress and strain and permits a description in

5

terms of stress-strain relations. It is sufficient to switch from the initial isotropic stress-strain law to an orthotropic law upon crack formation, with the axes of orthotropy being determined according to a condition of crack initiation. The procedure is attractive not only because it preserves the topology of the original finite element mesh, but also because it does not impose restrictions with respect to the orientation of the crack planes, i.e. the axes of orthotropy. It is for these two reasons that the smeared concept quickly replaced the early discrete concepts and came into widespread use during the 1970s.

Ever since cracking has been modeled, the discrete concept and the smeared concept have been the subject of much controversy. The discrete concept fits our natural conception of fracture since we generally identify fracture as a true, geometrical discontinuity. Conversely, it has been stated that a smeared representation might be more realistic considering the "bands of micro-cracks" that blunt fracture in matrix-aggregate composites like concrete. The width of such bands, which occur at the tip of the visible crack, has even been claimed to be a material property[Baza 83a]. At present, however, it is difficult to judge these arguments since experimental detections of crack tip related micro-mechanical processes in matrix-aggregate composites are scarce and contradictory as far as the question is concerned whether these processes occur in a discrete manner or not[Diam 85,Tait 86]. In this study the application of the smeared concept to cases of localized fracture is therefore considered to be an artifice for computational convenience[‡].

The arguments change when we consider distributed fracture. Examples are the diffuse crack patterns in large-scale shear walls or panels due to the presence of densely distributed reinforcement. Such cases provide a true physical basis for smeared concepts, at least if the scale of the representative continuum is large compared to the crack spacing. Even stronger, the smeared concept seems to be the only rational approach towards distributed fracture since the use of a discrete concept, which considers each individual crack as though "under a magnifying glass" then becomes clearly unwieldy. With the exception of section 7.3, this thesis will not touch on distributed fracture.

[‡] It is curious that the controversy generally centers around the processes *ahead* of the crack tip. In a practical analysis of localized fracture also the portion of the crack *behind* the tip is essential. In that respect, the smeared concept is definitely an artifice. An excellent demonstration is provided by the picture of Fig. 8.1, which shows genuine separation.

6

Smeared crack concepts can be categorized into fixed and rotating smeared crack concepts. With a fixed concept the orientation of the crack is fixed during the entire computational process, whereas a rotating concept allows the orientation of the crack to co-rotate with the axes of principal strain. This section addresses these two classes of concepts as well as the intermediate option of a fixed multi-directional smeared crack concept. Recent routes of modeling smeared cracks within the framework of plasticity[Onat 87,Cris 87,Will 87] are left out of consideration.

2.2.2 Standard fixed smeared crack concept

Traditionally, the stress-strain law for smeared cracking has been set-up with reference to fixed principal n,s,t-axes of orthotropy, where n refers to the direction normal to the crack (mode I) and s,t refer to the directions tangential to the crack (mode II and mode-III),

$$
\begin{bmatrix} \sigma_{nn} \\ \sigma_{ss} \\ \sigma_{tt} \\ \sigma_{ns} \\ \sigma_{st} \\ \sigma_{tn} \end{bmatrix} = \begin{bmatrix} E_{nn} & E_{ns} & E_{nt} & 0 & 0 & 0 \\ E_{ns} & E_{ss} & E_{st} & 0 & 0 & 0 \\ E_{nt} & E_{st} & E_{tt} & 0 & 0 & 0 \\ 0 & 0 & 0 & G_{ns} & 0 & 0 \\ 0 & 0 & 0 & 0 & G_{st} & 0 \\ 0 & 0 & 0 & 0 & 0 & G_{nt} \end{bmatrix} \begin{bmatrix} \varepsilon_{nn} \\ \varepsilon_{ss} \\ \varepsilon_{tt} \\ \gamma_{ns} \\ \gamma_{st} \\ \gamma_{tn} \end{bmatrix}
\tag{2.5}
$$

which is defined by nine independent stiffness moduli.

In the earliest versions[Rash 68,Cerv 70,Vall 72] E_{nn}, E_{ns}, E_{nt}, G_{ns} and G_{nt} were set equal to zero, involving the crack normal stress σ_{nn} and the crack shear stresses σ_{ns} and σ_{tn} to abruptly drop to zero upon crack formation. This is a crude approximation of reality as cracks in heterogeneous materials may well be capable of transmitting tension stresses in mode I and shear stresses in mode-II due to tortuous debonding and interlock. Moreover, the sudden switch from the initial isotropic linearly-elastic law to an orthotropic law with zero stiffness moduli implies a strong discontinuity which turned out to amplify numerical difficulties[Schn 72]. For these reasons, researchers reinserted the initial isotropic stiffness moduli with some percentage of reduction. For instance, Suidan & Schnobrich[Suid 73] reinserted G_{ns} and G_{nt} as a percentage of the initial linear-elastic shear modulus G. The corresponding reduction factor was called the shear stiffness reduction or shear retention factor β. Bazant & Oh[Baza 83a] broadened the concept by reinserting the stiffness E_{nn} normal to the crack as a percentage of the initial Young's modulus E, whereby they also introduced non-zero off-diagonal stiffness

7

moduli so as to incorporate Poisson's effect after cracking. In the 1980s the following incremental relation evolved into a popular orthotropic law for a two-dimensional configuration[Leib 86,Rots 84]:

$$
\begin{bmatrix} \Delta\sigma_{nn} \\ \Delta\sigma_{tt} \\ \Delta\sigma_{nt} \end{bmatrix} = \begin{bmatrix} \dfrac{\mu E}{1-v^2\mu} & \dfrac{v\mu E}{1-v^2\mu} & 0 \\ \dfrac{v\mu E}{1-v^2\mu} & \dfrac{E}{1-v^2\mu} & 0 \\ 0 & 0 & \dfrac{\beta E}{2(1+v)} \end{bmatrix} \begin{bmatrix} \Delta\varepsilon_{nn} \\ \Delta\varepsilon_{tt} \\ \Delta\gamma_{nt} \end{bmatrix}
\tag{2.6}
$$

E is Young's modulus, v is Poisson's ratio, μ is the reduction factor for the mode I stiffness which is negative in case of softening, and β is the shear retention factor.

2.2.3 Fixed smeared crack concept with strain-decomposition

The strain-vectors in (2.5) and (2.6) represent an overall strain of the cracked solid, which includes the strain due to cracking as well as the strain of the solid material between the cracks. The resulting stress-strain laws correspond to a smeared-out relation for the cracked solid, without making any distinction between the cracks and the solid material in between the cracks. The disadvantage is that particular crack laws, which start from the notion of crack strain rather than total strain, can not be incorporated in a transparent manner. Indeed, a gap tended to develop between the sophisticated crack models developed by materials scientists and the coarse smeared crack concepts employed by structural analysts. For instance, the choice of the shear retention factor was often made arbitrarily without reference to aggregate-interlock models.

A solution to this deficiency is to decompose the total strain $\Delta\varepsilon$ of the cracked material into a part $\Delta\varepsilon^{cr}$ of the crack and a part $\Delta\varepsilon^{co}$ of the solid material (superscript co of concrete) between the cracks,

$$
\Delta\varepsilon = \Delta\varepsilon^{cr} + \Delta\varepsilon^{co}
\tag{2.7}
$$

The importance of the decomposition has been recognized by a number of researchers[Litt 74,Baza 80,deBo 85,Rots 85a,Riggs 86‡]. It is in essence an attempt to come closer to

---

‡ The first smeared crack concept with strain-decomposition was probably proposed by Litton[Litt 74] in 1974. Although he considered mode I (crack opening) effects only, he demonstrated that the approach was consistent and easily extendible to include multi-directional cracking. Litton's ideas, however, have not been published in conference proceedings or international journals, which may partly explain why similar concepts have been proposed only ten years later.

the discrete crack concept which completely separates the solid material from the crack by using separate finite elements.

The strain vectors in (2.7) relate to the global coordinate axes and for a three-dimensional configuration they have six components. The global crack strain vector reads

$$\Delta\varepsilon^{cr} = \left[\begin{array}{cccccc} \Delta\varepsilon_{xx}^{cr} & \Delta\varepsilon_{yy}^{cr} & \Delta\varepsilon_{zz}^{cr} & \Delta\gamma_{xy}^{cr} & \Delta\gamma_{yz}^{cr} & \Delta\gamma_{zx}^{cr} \end{array} \right]^{T} \tag{2.8}$$

where x,y and z refer to the global coordinate axes and the superscript T denotes a transpose. When incorporating crack traction-crack strain laws it is convenient to set up a local n,s,t-coordinate system which is aligned with the crack, as shown in Fig. 2.1. In the local system, we define a local crack strain vector Δe^{cr},

$$\Delta e^{cr} = \left[\begin{array}{ccc} \Delta\varepsilon_{nn}^{cr} & \Delta\gamma_{ns}^{cr} & \Delta\gamma_{nt}^{cr} \end{array} \right]^{T} \tag{2.9}$$

where ε_{nn}^{cr} is the mode I crack normal strain and γ_{ns}^{cr}, γ_{nt}^{cr} are the mode II and mode III crack shear strains respectively. The three remaining crack strain components in the local system do not have a physical meaning and can be omitted.
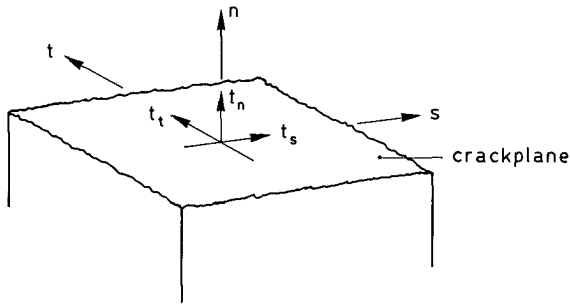
Fig. 2.1. Local coordinate system and tractions across a crack.

The relation between local and global crack strains reads

$$\Delta\varepsilon^{cr} = N \Delta e^{cr} \tag{2.10}$$

with N being a transformation matrix reflecting the orientation of the crack. A fundamental feature of the present concept is that N is assumed to be *fixed* upon crack formation, so that the concept belongs to the class of fixed crack concepts. For a three-dimensional configuration N reads

$$
N = \begin{bmatrix}
l_x^2 & l_x l_y & l_z l_x \\
m_x^2 & m_x m_y & m_z m_x \\
n_x^2 & n_x n_y & n_z n_x \\
2 l_x m_x & l_x m_y + l_y m_x & l_z m_x + l_x m_z \\
2 m_x n_x & m_x n_y + m_y n_x & m_z n_x + m_x n_z \\
2 n_x l_x & n_x l_y + n_y l_x & n_z l_x + n_x l_z
\end{bmatrix}
\tag{2.11}
$$

where l_x, m_x and n_x form a vector which indicates the direction of the local n-axis expressed in the global coordinates[‡]. In accordance with this convention, the direction cosines with subscript y indicate the local s-axis and those with subscript z indicate the local t-axis. For a plane-stress configuration the third column and the third, fifth and sixth row of (2.11) vanish, rendering a 3*2 matrix, while for axi-symmetric and plane-strain configurations the third column and the fifth and sixth row of (2.11) vanish, rendering a 4*2 matrix. Here, the reduced number of rows corresponds to the reduced number of global strain components, while the reduction from three to two columns arises from the fact that the mode III component vanishes.

In the local coordinate system, we define a vector Δt^{cr} of incremental tractions across the crack

$$
\Delta t^{cr} = \begin{bmatrix} \Delta t_n^{cr} & \Delta t_s^{cr} & \Delta t_t^{cr} \end{bmatrix}^T
\tag{2.12}
$$

in which Δt_n^{cr} is the mode I normal traction and Δt_s^{cr}, Δt_t^{cr} are mode II and mode III shear traction increments, as shown in Fig. 2.1. The relation between the global stress increment $\Delta \sigma$ and the local traction increment can be derived to be

$$
\Delta t^{cr} = N^T \Delta \sigma
\tag{2.13}
$$

To complete the system of equations, we need a constitutive model for the intact concrete and a traction-strain relation for the smeared cracks. For the concrete between the cracks a relationship is assumed of the following structure

---

‡ Considering (2.10), N can be set-up by extracting three *columns* from the full matrix for a strain-transformation from the local n,s,t axes to the global x,y,z axes. However, in the computer code it is more convenient to consider a transformation from the global x,y,z axes to the local n,s,t axes rather than vice-versa. To this end, consider (2.13) which represents a stress transformation with the global quantities on the right side and the local quantities on the left side. N can then be set-up by extracting three *rows* from the full global/local stress-transformation matrix. The transpose of the outcome is given in Eq. (2.11).

$$\Delta\sigma = D^{co}\Delta\varepsilon^{co} \tag{2.14}$$

with the matrix D^{co} containing the instantaneous moduli of the concrete. In a similar way, a relation is inserted between the local crack strain and the local tractions,

$$\Delta t^{cr} = D^{cr}\Delta e^{cr} \tag{2.15}$$

with D^{cr} a 3*3 matrix incorporating the mode I, mode II, mode-III and mixed-mode properties of the crack.

By properly combining Eqs. (2.7), (2.10), (2.13), (2.14) and (2.15) the overall stress-strain relation for the cracked concrete with respect to the global coordinate system can be developed. To this end, (2.10) is substituted into (2.7), and subsequently (2.7) into (2.14), which yields

$$\Delta\sigma = D^{co}[\Delta\varepsilon - N\Delta e^{cr}] \tag{2.16}$$

Pre-multiplying (2.16) by N^T and substituting (2.15) and (2.13) into the resulting left side of (2.16) yields the link between local crack strain and global strain,

$$\Delta e^{cr} = [D^{cr} + N^T D^{co} N]^{-1} N^T D^{co}\Delta\varepsilon \tag{2.17}$$

Finally, the overall relation between global stress and global strain is obtained by substituting (2.17) into (2.16),

$$\Delta\sigma = [D^{co} - D^{co} N [D^{cr} + N^T D^{co} N]^{-1} N^T D^{co}]\Delta\varepsilon \tag{2.18}$$

The expression between the outer brackets will be referred to as D^{crco} in the sequel (superscript crco of cracked concrete).

The incremental formulation of the concept entails two complications. First, (2.18) implies a linearization around the current state, which means that the stress increment computed holds exactly only if D^{co} as well as D^{cr} remain constant during the current strain increment. If either of these matrices is non-constant, which for instance occurs if the concrete model involves plasticity or if the crack model involves nonlinear fracture functions, (2.18) only serves as a first order approximation. A corrective procedure then becomes necessary in order to circumvent drifting from either the concrete or the crack stress-strain law. This study considers the case of nonlinear fracture functions, i.e. nonlinearity in D^{cr}. A possible corrective procedure is then provided by an inner iteration loop that repeatedly evaluates (2.17) and (2.15), starting from a predictor using tangent crack stiffness moduli and proceeding by correctors using secant crack stiffness moduli, as detailed before[Rots 86]. Such a forward-Euler scheme performed adequately with the examples considered in this thesis. However, in case of strong discontinuities (e.g. very steep softening) the method may sometimes fail and extensions along the line of sub-increments or other techniques are required that accommodate a more rigorous return to the fracture functions.

Secondly, an incremental simulation involves the state of the solid to be subject to change, owing to initiation, closing and re-opening of cracks. To handle state changes we employ a procedure that subdivides the strain path. When the criteria of initiation, closing and re-opening indicate a change of state during the current load increment, the total strain increment $\Delta\varepsilon$ is split into a pre-transition part $\Delta\varepsilon^a$ and a post-transition part $\Delta\varepsilon^b$,

$$\Delta\varepsilon = \Delta\varepsilon^a + \Delta\varepsilon^b \tag{2.19}$$

The stress increment is subsequently computed from different stress-strain relations for the pre- and post-transition parts respectively. In this way, the transition from the uncracked state to the cracked state, which occurs when a new crack initiates or when a closed crack re-opens, gives

$$\Delta\sigma = D^{co}\Delta\varepsilon^a + D^{crco}\Delta\varepsilon^b \tag{2.20}$$

whereas the transition from the cracked state to the uncracked state, which occurs when a crack closes, gives

$$\Delta\sigma = D^{crco}\Delta\varepsilon^a + D^{co}\Delta\varepsilon^b \tag{2.21}$$

Locating the state transition point is a straightforward operation when D^{co} and D^{cr} are constants. If they are not, an inner iteration loop should be invoked to scale $\Delta\varepsilon^a$, so as to satisfy the initiation, closing or re-opening conditions with reasonable accuracy.

Criteria of closing and re-opening are generally defined in terms of total local crack stress or total local crack strain. As the fixed crack concept assumes the local crack axes to remain unaltered, these quantities are readily available in the form of an accumulation of previous increments. This *permanent memory of damage orientation* is the prominent feature of fixed smeared crack concepts.

2.2.4 Multi-directional fixed smeared crack concept

A further advantage of the decomposition of total strain into concrete strain and crack strain is that it allows for a sub-decomposition of concrete strain and crack strain on their turn. A sub-decomposition of the concrete strain[deBo 86] will not be considered here, but we will concentrate on a sub-decomposition of the crack strain into the separate contributions from a number of multi-directional cracks that simultaneously occur at a sampling point, i.e.

$$\Delta\varepsilon^{cr} = \Delta\varepsilon_1^{cr} + \Delta\varepsilon_2^{cr} + \ldots\ldots\ldots \tag{2.22}$$

where $\Delta\varepsilon_1^{cr}$ is the global crack strain increment owing to a primary crack, $\Delta\varepsilon_2^{cr}$ is the

12

global crack strain increment owing to a secondary crack and so on.

The idea of a sub-decomposition of the crack strain was advocated by Litton[Litt 74], de Borst & Nauta[deBo 85] and Riggs & Powell[Rigg 86]. The essence of their approach is that each (fixed) crack is assigned its own local crack strain vector e_i^{cr}, its own traction vector t_i^{cr} and its own transformation matrix N_i according to (2.9), (2.12) and (2.11) respectively. They furthermore demonstrated that it is convenient to assemble these single-crack vectors and matrices into

$$\Delta \hat{e}^{cr} = \left[\Delta e_1^{cr} \ \Delta e_2^{cr} \ \ldots\ldots \right]^T \tag{2.23}$$

$$\Delta \hat{t}^{cr} = \left[\Delta t_1^{cr} \ \Delta t_2^{cr} \ \ldots\ldots \right]^T \tag{2.24}$$

$$\hat{N} = \left[N_1 \ N_2 \ \ldots\ldots \right] \tag{2.25}$$

in which ^ denotes an assembly of multi-directional cracks. Repeated substitution of (2.10) into (2.22) yields

$$\Delta \varepsilon^{cr} = \hat{N} \Delta \hat{e}^{cr} \tag{2.26}$$

which is the multiple-crack equivalent of (2.10). In a similar way, the single-crack traction-strain relations can be expanded into a multiple-crack equivalent of (2.15),

$$\Delta \hat{t}^{cr} = \hat{D}^{cr} \Delta \hat{e}^{cr} \tag{2.27}$$

or, in the elaborated form,

$$\begin{bmatrix} \Delta t_1^{cr} \\ \Delta t_2^{cr} \\ \ldots \end{bmatrix} = \begin{bmatrix} D_{11}^{cr} & D_{12}^{cr} & \ldots \\ D_{21}^{cr} & D_{22}^{cr} & \ldots \\ \ldots & \ldots & \ldots \end{bmatrix} \begin{bmatrix} \Delta e_1^{cr} \\ \Delta e_2^{cr} \\ \ldots \end{bmatrix}$$

which is a very general relation since it allows for interaction between the cracks via the off-diagonal submatrices.

Repeating the procedure of the previous section, we end up with the analogy of (2.18) for multi-directionally cracked concrete:

$$\Delta \sigma = [D^{co} - D^{co} \hat{N} [\hat{D}^{cr} + \hat{N}^T D^{co} \hat{N}]^{-1} \hat{N}^T D^{co}] \Delta \varepsilon \tag{2.28}$$

The assembled matrices $\hat{N}$ and $\hat{D}^{cr}$ are inserted instead of the single-crack matrices N and D^{cr}.

Considering sampling points with multi-directional cracks, the issue of state changes becomes increasingly pressing and sometimes even failure of the implementation was reported for this reason$^{Cris\ 87}$. In the present study, the procedure of transition points, as outlined in the preceding for single cracks, has been unambiguously extended to include state changes for multi-directional cracks. Considering a current configuration of i unclosed cracks, and dividing the strain-increment $\Delta\varepsilon$ into a pre-transition part $\Delta\varepsilon^a$ and a post-transition part $\Delta\varepsilon^b$, the state change due to initiation of a new crack or re-opening of a closed crack gives

$$\Delta\sigma = \hat{D}_i^{crco}\Delta\varepsilon^a + \hat{D}_{i+1}^{crco}\Delta\varepsilon^b \tag{2.29}$$

whereas the state change due to closing of one of the cracks gives

$$\Delta\sigma = \hat{D}_i^{crco}\Delta\varepsilon^a + \hat{D}_{i-1}^{crco}\Delta\varepsilon^b \tag{2.30}$$

where $\hat{D}_{i-1}^{crco}$, $\hat{D}_i^{crco}$ and $\hat{D}_{i+1}^{crco}$ denote the overall stress-strain matrices of (2.28) for configurations of $i-1$, i and $i+1$ unclosed cracks respectively, which are based on the underlying assembled local traction-strain matrices $\hat{D}_{i-1}^{cr}$, $\hat{D}_i^{cr}$ and $\hat{D}_{i+1}^{cr}$ of (2.27) and on the underlying assembled transformation matrices $\hat{N}_{i-1}$, $\hat{N}_i$ and $\hat{N}_{i+1}$ of (2.25). Consequently, whenever a new crack initiates or a closed crack re-opens $\hat{D}^{cr}$ and $\hat{N}$ are expanded to include the associated submatrices, while they are compressed on crack closure to delete the associated submatrices. The magnitude of the pre-transition strain increment $\Delta\varepsilon^a$ must be scaled so as to satisfy the initiation, closing or re-opening condition with reasonable accuracy.

A state change for one of the cracks promotes state changes of the others. For instance, the initiation of a new crack encourages existing cracks to close. If such multiple state changes occur during the current strain increment, the "most critical" state change should be traced and handled first, while subsequent state changes should be treated by splitting $\Delta\varepsilon^b$ on its turn. Depending on the particular crack closing condition, this procedure may become elusive and it may be more convenient to allow only one crack to change its state, while possible state changes of other cracks are postponed until the next stage of the incremental simulation. In the latter case, inconsistencies cannot entirely be avoided, since postponing crack closing involves the crack normal strain to temporarily become negative, which is physically meaningless.

The significance of the multi-directional crack concept is obvious in conditions of biaxial or triaxial tension. Here, we expect two or three *orthogonal* cracks, the behavior of each of which can be monitored separately keeping record of memory. This option is particularly relevant with axi-symmetric and plane-strain analysis, where numerous points may be cracked longitudinally as well as transversely.

A second important field of application is given by conditions of tension-shear, which is typical of fracture propagation problems with the fracture starting in tension (mode I) and subsequently proceeding in tension-shear (mixed-mode). This behavior implies that the axes of principal stress rotate after crack formation, which leads to an increasing discrepancy between the axes of principal stress and the fixed crack axes. It is for this reason that the fixed single-crack concepts become increasingly subject to criticism[Will 87,Cris 87,Koll 87]. Pending the treatment of the rotating crack concept, which rigorously eliminates the phenomenon by enforcing coaxiality between principal axes and crack axes, it is noted that the fixed multi-directional crack concept provides an alternative. Whenever the angle of inclination between the existing crack(s) and the current direction of principal stress exceeds the value of a certain *threshold angle,* a new crack is initiated. In this way, we end up with a system of *non-orthogonal* cracks as pioneered by de Borst & Nauta[deBo 85].

2.2.5 Rotating smeared crack concept

The misalignment of principal directions and crack directions, as adhering to fixed crack concepts, prompted Cope et al.[Cope 80] to co-rotate the axes of material orthotropy with the axes of principal strain. The approach subsequently evolved into the rotating crack concept. The concept is attractive from an engineering point of view, since the analyst can suffice to specifying non-linear stress-strain curves for the principal directions, without having to resort to abstract theories.

Bazant[Baza 83b] raised a number of objections to the earliest versions of the concept. One of them relates to the fact that the assumption of material orthotropy generally implies the rotation of principal stress to deviate from the rotation of principal strain. Consequently, when the axes of material orthotropy co-rotate with the axes of principal strain, they will cease to coincide with the axes of principal stress. The direct use of principal stress-strain curves then becomes inconsistent, unless transformation rules are included in the derivation of the tangential stiffness moduli.

Although he did not pursue this issue further, Bazant[Baza 83b] also outlined an important condition that enforces coaxiality between principal stress and strain. To illustrate this, consider a 2D configuration of initial coaxiality, with the principal 1,2 directions of stress, strain and material orthotropy being aligned. By virtue of Mohr's strain circle, a small increment of shear strain causes the direction of principal strain to rotate by an angle $\Delta\theta_\varepsilon$ according to

$$\tan 2\Delta\theta_\varepsilon = \frac{\Delta\gamma_{12}}{2(\varepsilon_{11}-\varepsilon_{22})} \tag{2.31}$$

if $|\Delta\gamma_{12}| \ll |\varepsilon_{11}-\varepsilon_{22}|$. Here, $\Delta\gamma_{12}$ is the shear strain increment in the 1,2 reference frame and $\varepsilon_{11}, \varepsilon_{22}$ are the initial principal strains. In a similar fashion, Mohr's stress circle indicates that a small increment of shear stress causes a principal stress rotation by an angle $\Delta\theta_\sigma$ according to

$$\tan 2\Delta\theta_\sigma = \frac{\Delta\sigma_{12}}{(\sigma_{11}-\sigma_{22})} \tag{2.32}$$

if $|\Delta\sigma_{12}| \ll |\sigma_{11}-\sigma_{22}|$. Preserving coaxiality between principal stress and strain requires $\Delta\theta_\varepsilon = \Delta\theta_\sigma$. Using the orthotropic law of (2.5) in the principal 1,2 reference frame, we observe that this condition is satisfied if and only if the tangential shear modulus G_{12} is given by

$$G_{12} = \frac{(\sigma_{11}-\sigma_{22})}{2(\varepsilon_{11}-\varepsilon_{22})} \tag{2.33}$$

The linearized form of the tangential stress-strain law for a consistent rotating crack concept then becomes

$$\begin{bmatrix} \Delta\sigma_{11} \\ \Delta\sigma_{22} \\ \Delta\sigma_{33} \\ \Delta\sigma_{12} \\ \Delta\sigma_{23} \\ \Delta\sigma_{31} \end{bmatrix} = \begin{bmatrix} \dfrac{\partial\sigma_{11}}{\partial\varepsilon_{11}} & \dfrac{\partial\sigma_{11}}{\partial\varepsilon_{22}} & \dfrac{\partial\sigma_{11}}{\partial\varepsilon_{33}} & 0 & 0 & 0 \\[2ex] \dfrac{\partial\sigma_{22}}{\partial\varepsilon_{11}} & \dfrac{\partial\sigma_{22}}{\partial\varepsilon_{22}} & \dfrac{\partial\sigma_{22}}{\partial\varepsilon_{33}} & 0 & 0 & 0 \\[2ex] \dfrac{\partial\sigma_{33}}{\partial\varepsilon_{11}} & \dfrac{\partial\sigma_{33}}{\partial\varepsilon_{33}} & \dfrac{\partial\sigma_{33}}{\partial\varepsilon_{33}} & 0 & 0 & 0 \\[2ex] 0 & 0 & 0 & \dfrac{\sigma_{11}-\sigma_{22}}{2(\varepsilon_{11}-\varepsilon_{22})} & 0 & 0 \\[2ex] 0 & 0 & 0 & 0 & \dfrac{\sigma_{22}-\sigma_{33}}{2(\varepsilon_{22}-\varepsilon_{33})} & 0 \\[2ex] 0 & 0 & 0 & 0 & 0 & \dfrac{\sigma_{33}-\sigma_{11}}{2(\varepsilon_{33}-\varepsilon_{11})} \end{bmatrix} \begin{bmatrix} \Delta\varepsilon_{11} \\ \Delta\varepsilon_{22} \\ \Delta\varepsilon_{33} \\ \Delta\gamma_{12} \\ \Delta\gamma_{23} \\ \Delta\gamma_{31} \end{bmatrix} \tag{2.34}$$

where the derivatives $\partial\sigma_{11}/\partial\varepsilon_{11}$ etc. can be inserted directly since the shear terms guarantee coaxiality between principal stress and strain.

16

Eq. (2.34) was developed in a more elegant way by Willam et al.[Will 87]. An alternative formulation was derived by Gupta & Akbar[Gupt 84] and Crisfield & Wills[Cris 87], who started from a description in a fixed x,y coordinate system.

It is intriguing to examine the parallels between the fixed multi-directional crack concept and the rotating crack concept. While the fixed multi-directional concept controls the formation of subsequent cracks via the threshold angle, the rotating concept assumes the crack orientation to change continuously. Assuming the threshold angle for multi-directional cracks to vanish, a new fixed crack arises at the beginning of each stage of the incremental process. In doing so, we observe that the fixed multi-directional concept reduces to the rotating concept, provided that

— the condition of a vanishing threshold angle is the *only* condition that controls the orientation of subsequent cracks, i.e. it is not augmented by a maximum stress condition as was done in a previous study[deBo 85],

— previous cracks are rigorously made inactive and erased from memory upon activation of the new crack, so that we invariably have only one active crack which is unique to the loading phase,

— the local traction-strain law (2.15) of the active crack is filled in such a way that (a) the memory of previous defects is accounted for, (b) the overall shear modulus ensures coaxiality according to (2.33).

In the present study, rotating cracks will be conceived in this fashion. The three listed conditions will be elaborated in section 3.3. Strictly speaking, the term 'rotating crack' no longer applies since *we consider a collection of fixed tiny defects of different orientation, each of them having its own local traction-strain law, rather than a single rotating crack with a rotating principal stress-strain relation.* As an advantage, a second objection against rotating crack concepts raised by Bazant[Baza 83b], namely that rotating defects against the material is unacceptable from a physical point of view, no longer applies either. Besides, with distributed fracture the notion of fixed defects of gradually rotating orientation is supported by experimental evidence[Vecc 86,Bhid 87,Koll 87]. With localized fracture such experimental justification does not seem to exist, but there is little argument that mixed-mode crack tip processes involve fixed defects of gradually rotating orientation.

A further advantage of conceiving the rotating crack approach as the limiting case of the fixed multi-directional crack approach is that it maintains decomposition of total strain into concrete strain and crack strain. This permits the concrete material law (e.g. elasticity) to be satisfied exactly. With other versions of the rotating crack concept this is not necessarily true as these models sometimes lose Poisson's effect after cracking[Gupt 84,Milf 84,Bala 87,Cris 87]. The strain-decomposition is also essential for a

17

consistent combination of smeared cracking with plasticity, creep and thermal loading$^{deBo\,87}$.

Since (2.34) is given in incremental form, a corrective procedure must be added in order to suppress drifting from the coaxiality condition as induced by evaluating (2.34) for finite increments of strain. To this purpose an inner iteration loop has been employed, whereby (2.34) is repeatedly evaluated using the initial tangential shear term $(\sigma_{11}^0-\sigma_{22}^0)/2(\varepsilon_{11}^0-\varepsilon_{22}^0)$ in the first inner iteration (predictor) and updated tangential shear terms $(\sigma_{11}^i-\sigma_{22}^i)/2(\varepsilon_{11}^i-\varepsilon_{22}^i)$ in subsequent iterations (correctors). Here, the superscript ^{0} refers to the initial state which is coaxial (except for previous inaccuracies), and ^{i} refers to the calculated state from the previous iteration. The procedure replicates the treatment of nonlinear fracture functions$^{Rots\,86}$ and shows fast convergence provided that the load increments are taken sufficiently small to prevent the stresses from rotating heavily. For the example problems in this thesis, a coaxiality norm of 0.1 degrees was easily achieved within less than five inner iterations.

2.2.6 Discussion

It has been shown that fixed single, fixed multi-directional and rotating smeared crack concepts can be put into one framework. The rotating crack concept is thereby conceived as the limiting case of the fixed multi-directional crack concept. The key to this unification is a consistent decomposition$^{Litt\,74,Baza\,80,deBo\,85,Rots\,85a,Riggs\,86}$ of the strain into concrete strain and crack strain. Furthermore, procedures have been outlined that handle state changes owing to initiation, closing and re-opening of cracks.

The fundamental difference between the three variants lies in the orientation of the crack, which is either kept constant (fixed single), updated in a stepwise manner following a threshold angle (fixed multi-directional), or updated continuously (rotating). Hence, the fixed crack concept preserves permanent memory of the damage orientation, whereas the rotating crack concept does not. This implies that with the rotating crack concept inactive defects cannot be re-activated during a subsequent stage of the loading process, which has consequences when the loading process is non-proportional.

A further difference relates to the possibility of incorporating shear effects from e.g. aggregate interlock models. The fixed crack concepts fit the nature of such models since these also refer to a fixed crack plane. On the one hand, this is an advantage. On the other hand, the use of any crack shear relation for fixed cracks also *complicates* the analysis because it is responsible for an often uncontrollable rotation of the axes of principal stress, which cease to coincide with the axes of principal strain. With the

18

rotating crack concept these considerations hold in a converse manner. This concept accommodates a unique shear term that enforces coaxiality between principal stress and strain, which introduces simplicity, but it inherently abandons the possibility of incorporating different crack shear models since the crack always occurs in a principal direction, i.e. in mode I. The latter issue does not seem to have been recognized widely. Little is known about the implications for conditions where shear transfer and dilatancy across cracks dominate the response.

Nevertheless, recent years have witnessed a revival of rotating crack concepts[Gupt 84,Milf 84,Vecc 86,Will 87,Cris 87,Koll 87,Bala 87,Bhid 87], stimulated by the arbitrariness in shear retention factors for fixed cracks and the complexities involved in fixed multi-directional cracks. The majority of these studies revealed realistic predictions for rotating cracks, while fixed cracks tended to behave too stiff. These studies were invariably directed towards distributed fracture and were mostly concerned with single-element tests. For localized fracture and element assemblies, comparisons between the various concepts have received much less attention. This poses a challenge for the present study.

19

3. ELASTIC-SOFTENING CONSTITUTIVE MODEL

Having treated the crack concepts, the present chapter proceeds with embedding constitutive models into the concepts. For tension and tension-shear dominated problems an adequate model is constructed by assuming elasticity for the concrete and softening for the crack. The objective is to present a rational formulation of the softening component for fixed single, fixed multi-directional and rotating cracks successively.

The overwhelming amount of possibilities makes that we have to assume and postulate in order to achieve transparency. The assumptions will be verified and justified for a tension-shear model problem that covers the crucial issue of stress rotation after fracture.

3.1 Single-crack parameters

3.1.1 Essentials

Prior to cracking, concrete is represented sufficiently accurately as an isotropic, linear-elastic material. The parameters are Young's modulus E and Poisson's ratio v. Upon crack initiation, the strain decomposition according to (2.7) is mobilized and for the concrete we continue with linear elasticity, while (2.3) or (2.15) is inserted for the crack. Eq. (2.3) relates the traction increment Δt^{cr} to the crack displacement increment Δu^{cr} for discrete cracks via C^{cr}, whereas (2.15) relates the traction increment to the crack strain increment Δe^{cr} for smeared cracks via D^{cr}. In the present study, these matrices are assumed to be of the form:

$$C^{cr} = \begin{bmatrix} C^I & 0 & 0 \\ 0 & C^{II} & 0 \\ 0 & 0 & C^{III} \end{bmatrix} \tag{3.1}$$

and

$$D^{cr} = \begin{bmatrix} D^I & 0 & 0 \\ 0 & D^{II} & 0 \\ 0 & 0 & D^{III} \end{bmatrix} \tag{3.2}$$

where C^I, C^{II}, C^{III} and D^I, D^{II}, D^{III} are the mode I, mode II and mode III stiffness moduli for a discrete single crack and a smeared single crack respectively.

20

The assumption of zero off-diagonal terms in (3.1) and (3.2) implies that direct shear-normal coupling has been ignored. This assumption arises from three considerations:

— To date, experimental evidence for the importance of coupling terms exists only for the case of confined sliding along macro-cracks[e.g.Walr 80]. In that field, crack dilatancy theories with non-symmetric matrices have been proposed[Walr 80,Baza 80]. In the present study the focus is placed on initiation and propagation of the crack rather than on sliding along an existing crack. For such cases, experimental data on shear-normal coupling are not yet available and any choice of the coupling terms would remain a guess.

— Although (3.1) and (3.2) ignore direct shear-normal coupling, this effect may be obtained indirectly, by
  (a) allowing subsequent, non-orthogonal cracks to form,
  (b) relating the diagonal terms of C^{cr} and D^{cr} not only to their associated displacement and strain component respectively, but also to the others (for instance, the shear modulus D^{II} can be made a function of the crack normal strain).

— It is instructive to start from simple models and a posteriori discuss whether the simplifications are justified, or whether more complicated models are required. This discussion is provided at the end of the chapter and will highlight the technique of indirect coupling via non-orthogonal cracks.

A salient feature of the model components presented in the sequel is that they assume fracture to be initiated in mode I, whereas mode II or mode III shear effects only enter upon subsequent rotation of the principal stresses. This hypothesis is supported by experimental evidence with respect to static loading conditions of tension and tension-shear[e.g.Arre 82]. Contrary experimental results have been reported only for dynamic loadings[Harm 82] and for very particular static loadings with a high mode II[Baza 86a] or mode III[Baza 88] intensity. Such cases are beyond the scope of the present study.

The feature implies that distinction between mode II and mode III becomes irrelevant, so that notation will be confined to mode II.

3.1.2 Mode I parameters

Traditionally, a set of strength parameters has been introduced to control fracture initiation. These parameters locate a tension cut-off condition in the principal stress space. When the combination of principal stresses violates this condition, the crack is initiated. In the present study attention is confined to only one strength parameter, viz. the uniaxial tensile strength f_{ct}, involving the tension cut-off to reduce to a maximum

stress condition. When tensile cracking is not accompanied by significant lateral compression this postulate is justified[Kupf 69]. Upon initiation, the crack is assumed to be oriented perpendicular to the direction of the major principal tensile stress, which is accepted[Nils 82] and correct[Kupf 69] in the absence of significant lateral compression.

Less agreement has settled over the years as to the existence of a proper set of parameters controlling fracture propagation. One might confine himself to the single strength parameter and assume a sudden stress-drop upon fracture initiation. However, these strength criteria have been criticized by Bazant & Cedolin[Baza 79] for they suffer from non-objectiveness. Other attempts aimed at extending the principles of linear elastic fracture mechanics and elastic-plastic fracture mechanics to cementitious materials, but were judged to be inadequate either since the pursuit of unique critical stress-intensity factors, J-integrals and R-curves largely remained without success.

To date, the most versatile alternative in finite element analysis is to use a mode I fracture function that embodies tensile softening[Hill 76,Baza 83a]. The parameters are the fracture energy G_f, which is defined as the amount of energy required to create one unit of area of a mode I crack, and the shape of the tensile-softening diagram. These two parameters are assumed to be fixed material properties. With respect to G_f this postulate is justified since experimental data show that the energy required to fracture mode I specimens is fairly proportional to the surface area generated[‡]. Typical values lie in the range between 50 and 200 J/m^2, depending on concrete quality.

There is no consensus on the question whether the tensile-softening diagram is a material property. Although experimental results show uniformity in their identification of a concave curve with a steep decline just after the peak, the softening diagrams employed currently vary from linear and bilinear to several types of nonlinear diagrams. We will mainly employ the nonlinear, exponential diagram proposed by Reinhardt et al.[Rein 86] (Fig. 3.1). A justification is given in chapter 5.

---

‡ The postulate is justified if experiments render G_f independent of specimen geometry and specimen size. With respect to specimen geometry, Petersson[Pete 81] demonstrated a switch from notched beams to direct tension specimens to affect G_f by less than 3 percent. Similar slight discrepancies on using different geometries were found at Delft University[Hord 87]. With respect to specimen size, Petersson[Pete 81] reported only a 23 percent increase of G_f upon a four-fold increase of size for notched beams, while Hilsdorf & Brameshuber[Hils 85] encountered no more than a 20 percent increase of G_f upon an eight-fold (!) increase of size. This trend was confirmed, not strengthened, in a recent round-robin test[Hils 85a] and is attributable to tortuosity of cracks and dissipation of energy outside the fracture zone.

Considering the unpredictable nature of heterogeneous materials, the above trends and discrepancies are not dramatic. They remain tolerable compared to the scatter in accepted properties like tensile strength and compressive strength. For instance, the 20 percent difference between cube strength and cylinder strength has not prevented these properties from gaining popularity in design codes. The objections raised against G_f at recent conferences are therefore thought to be exaggerated.
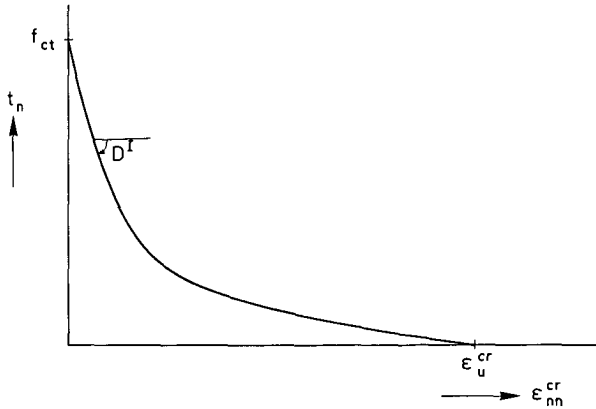
Fig. 3.1. Nonlinear mode I tensile softening relation between crack normal traction and crack normal strain[Rein 86].

The question of non-uniqueness in softening parameters relates to the fact that softening is partly a structural phenomenon, since it is apparently impossible to strain material samples homogeneously into the post-peak regime [Kots 83,Read 84,VanM 84]. To date, the consequences hereof are far from obvious and Kotsovos[Kots 83] even proposed to abandon the entire softening concept for this reason, while van Mier[VanM 84] raised similar statements. We will amply comment on this issue in chapter 5 and investigate whether they overstate or not.

Finally, the crack stiffness moduli must be expressed in terms of the strength parameter, the energy parameter and the shape of the softening diagram. For a fixed single crack the definition of G_f gives

$$G_f = \int t_n^{cr} \, du_n^{cr} \qquad (3.3)$$

which corresponds to the area under the softening curve for a discrete crack. Here, t_n^{cr} is the crack normal traction and u_n^{cr} is the crack normal displacement. Evaluation of (3.3) simply results in a tangential softening modulus for a single discrete crack

$$C^I = -\frac{1}{k} \frac{f_{ct}^2}{G_f} \qquad (3.4)$$

with k reflecting the shape of the softening diagram ($k=2$ for linear softening and $k=0.74$ for the initial slope of the nonlinear softening diagram of Fig. 3.1).

For smeared cracks, the fracture is distributed over a crack band width h, which is related to the particular finite element configuration. Consequently, the energy should be released over this width in order to obtain results that are objective with regard to

23

mesh refinement[Baza 79]. Assuming a constant strain distribution over the crack band gives $u_n^{cr}=h\,\varepsilon_{nn}^{cr}$. This leads to

$$D^I = -\frac{1}{k}\frac{f_{ct}^2 h}{G_f} \tag{3.5}$$

The assumption of constant crack strain over the crack band is justified for lower order elements and for particular cases of symmetry[Rots 85a]. It does not hold for higher order elements, but the error introduced is offset by different aspects, such as the necessity to specify the crack band width a priori, as will be demonstrated in chapter 4. These difficulties arise from the fact that the introduction of h into D^I constitutes only a first step towards a non-local softening model. Mathematically consistent types of non-local models that incorporate the micro-structure of continua are currently being pursued[Baza 86b].

The stress-free strain ε_u^{cr} at softening completion (Fig. 3.1) is not conceived as a separate material property. ε_u^{cr} is a consequence of the crack band width h and the three properties in the model (tensile strength, fracture energy and softening diagram).

3.1.3 Mode II parameters

With the discrete crack applications in this thesis, both the shear traction and the shear stiffness after cracking have been set equal to zero. This is justified because these applications focus on pure mode I cracking, i.e. the potential discrete crack elements will be pre-aligned with the expected orientation of the principal tensile stresses. Shear tractions then only result from the inability to align the discrete elements with the principal tensile stresses exactly. Consequently, the shear tractions at the onset of cracking will be insignificant, which justifies setting them to zero. The stress rotations occur in the elastic elements at either side of the discrete crack elements.

For smeared cracks, the crack shear modulus D^{II} has in the past been assigned a constant value, which corresponds to a linear ascending relation between shear stress and shear strain across the crack. Apart from the arbitrariness involved in the particular choice for this value, the approach suffers from the drawback that the shear stress can increase indefinitely, and, hence, the principal stresses in the cracked elements rotate ceaselessly ($D^{II}=0$ of course constitutes an exception).

An improvement is obtained by making the shear stiffness after cracking a decreasing function of the crack normal strain[Cedo 77,Kolm 84,Rots 84]. The model accounts for the fact that the interlock of aggregate particles diminishes with increasing crack opening. This phenomenon has been observed for macro-cracks[Walr 80] and is likely to occur also when the "crack" is in the softening stage.

24

In this study numerical experiments will be undertaken with a power law:

$$D^{II} = \frac{\left[1 - \dfrac{\varepsilon_{nn}^{cr}}{\varepsilon_{u}^{cr}}\right]^{p}}{1 - \left[1 - \dfrac{\varepsilon_{nn}^{cr}}{\varepsilon_{u}^{cr}}\right]^{p}}\, G \tag{3.6}$$

in which ε_{nn}^{cr} is the crack normal strain at the beginning of the load increment, ε_{u}^{cr} is the stress-free crack normal strain (Fig. 3.1), p is a constant and G is the elastic shear modulus. Eq. (3.6) gives a degradation of D^{II} from infinite upon initiation to zero at the stage where the softening is completed, i.e. where the micro-cracks coalesce into a macro-crack. Fig. 3.2a shows the relation for $p=1$. An interpretation in terms of the traditional shear retention factor is given in section 3.1.5, along with Fig. 3.2b.
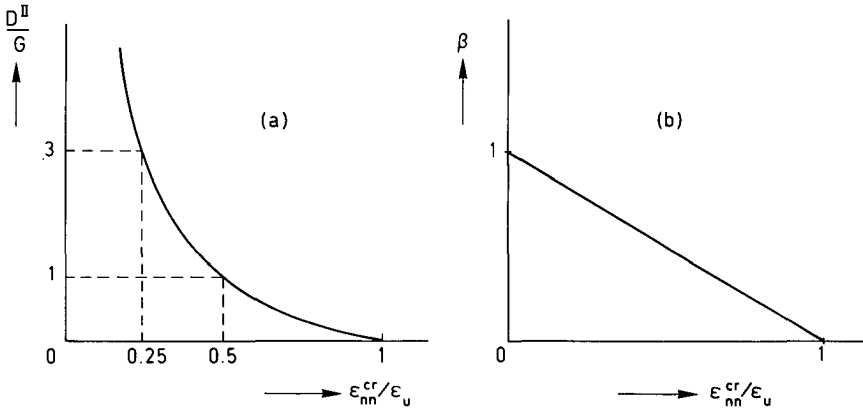

Fig. 3.2. (a) Mode II shear modulus of (3.6) which decreases with increasing crack strain.
(b) The corresponding shear retention function β of (3.8).

Recalling the motives of the beginning of the chapter, (3.6) is seen as an effort towards implicit coupling between shear and normal components. The fact that (3.6) gives zero shear stiffness beyond ε_{u}^{cr} implies that shear stiffness from aggregate inter-lock across macro-cracks is ignored. This implication does not have consequences for the present study since we concentrate on the stage in which the crack comes into being and not on the confined sliding along an existing crack, or, put differently, on the stage in which the crack normal stress is tensile instead of compressive.

An advantage of (3.6) is that it is *objective with respect to mesh refinement*, since ε_{u}^{cr} is adapted to the crack band width. The traditional procedures do not meet this requirement, with the exception of recent work by Ottosen & Dahlblom[Otto 86].

25

3.1.4 Unloading and reloading

Fig. 3.3 shows the two extremes of elastic and secant type of unloading/reloading options. For elastic unloading, the crack closes immediately upon a strain reversal, whereafter further strain-decomposition is terminated and a rigorous return is made to elastic behavior. Strictly speaking, the term closing does not apply since the crack strain·is irreversible. It is more correctly to speak of an inactive crack or an arrested crack. For secant unloading, the crack normal strain is reversible and upon reaching the origin of the diagram the crack truly closes, i.e. $\varepsilon_{nn}^{cr}=0$, whereafter elastic behavior is recovered.
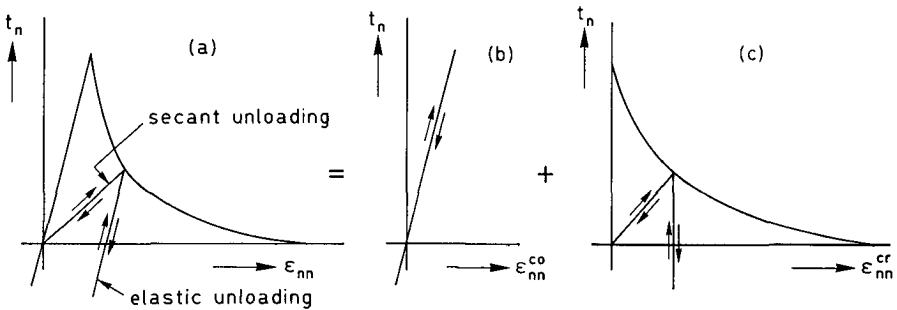

Fig. 3.3. Secant and elastic unloading in mode I elastic-softening model.
Normal stress versus total strain (a), concrete strain (b) and crack strain (c).

Neither of the two extremes constitutes an accurate approximation of reality, since cyclic tests reveal hysteresis[Rein 86]. The present study does not consider cyclic or non-proportional loading, but it employs the procedures for capturing non-proportional straining involved in fracture localization. In the latter case, it is of more importance *that* we distinguish between active cracks and arrested cracks than *how* we distinguish between them. For that purpose, the two extremes serve as a useful tool.

An advantage of elastic unloading is that the pre-transition part of the incremental strain at "closing", as introduced in (2.19), disappears, which keeps the computer code robust. Furthermore, since the crack "closes" abruptly, it no longer contributes to D^{crco}, which saves computational costs. Secant unloading is less attractive from this point of view. On the other hand, secant unloading somewhat accounts for the decrease of compliance with increasing crack opening strain[Rein 86], whereas elastic unloading always provides the same unloading stiffness E, even beyond ε_u^{cr}. The judge of these arguments depends on the type of application.

26

Upon closing, the stresses, crack strains as well as the orientation of the fixed single crack are stored in order to check for re-opening during a subsequent stage of the loading process. A closed crack will be assumed to re-open if the stress normal to it exceeds the stress which existed upon closing. In this way, re-opening is a stress-controlled process, similar to crack initiation.

A further key-aspect is that unloading and reloading appear as mode I dominated processes. The mode II behavior is assumed to be independent of the mode I status, so that it is possible for a crack to be active in mode I and inactive in mode II, inactive in mode I and active in mode II, active in both modes, or inactive in both modes. The precise handling of all state combinations is a delicate matter, not only because the crack shear strain need not vanish upon closing but also because the crack shear stress upon mode I re-opening may well differ from the crack shear stress which existed upon closing owing to stress rotations during the closed state. A proper and numerically stable procedure has been detailed in a separate paper[Rots 87e].

3.1.5 Relation with traditional parameters

It is recalled from section 2.2.1 that traditional smeared crack formulations represent the overall shear stiffness of a cracked solid in terms of the shear retention factor β[Suid 73] which reduces the elastic shear modulus G to βG upon cracking. β can be related to the crack shear modulus D^{II} of the present model by considering that the stiffness βG is associated with the total strain, and that D^{II} is solely associated with the crack strain. By virtue of the strain decomposition of (2.7) concrete and crack act like springs connected in series, so that the following stiffness relation holds

$$\frac{1}{\beta G} = \frac{1}{G} + \frac{1}{D^{II}} \qquad \rightarrow \qquad D^{II} = \frac{\beta}{1-\beta} G \qquad (3.7)$$

in case of elastic-cracked behavior. In this way, the classical shear retention factor is re-interpreted in the spirit of mode II crack shear. For instance, the power function of (3.6) can be rewritten as

$$\beta = \left[1 - \frac{\varepsilon_{nn}^{cr}}{\varepsilon_{u}^{cr}} \right]^{p} \qquad (3.8)$$

and we observe that the degradation of D^{II} from infinite (full interlock) to zero corresponds to a degradation of β from 1 (full retainment of elastic shear) to zero. Fig. 3.2 shows the functions for $p = 1$.

Along similar lines, the series arrangement provides us with a connection between the mode I softening modulus D^I and the overall (negative) stiffness μE of the elastic softening continuum, as introduced in section 2.2.1,

$$\frac{1}{\mu E} = \frac{1}{E} + \frac{1}{D^I} \qquad \rightarrow \qquad D^I = \frac{\mu}{1-\mu} E \qquad (3.9)$$

Eq. (3.9) sheds light on the condition of snap-back instability at local integration point level. We observe that μE becomes infinite or, put differently, the softening diagram reduces to a sudden stress-drop if

$$D^I = -E \qquad (3.10)$$

Together with (3.5) this yields a maximum crack band width below which the softening maintains a negative slope[Baza 83a],

$$h \leq k \frac{G_f E}{f_{ct}^2} \qquad (3.11)$$

where k again reflects the shape of the softening diagram (see Eq. 3.4), which is critical at the peak if the curve is concave. If the crack band width exceeds this limit[‡], the local stress-strain relation shows a snap-back[Carp 86,Cris 84] and the condition of invariant fracture energy is no longer satisfied unless we resort to reduction of the strength limit in combination with a sudden stress drop[Baza 79]. Indeed, in the present study the strength limit has been automatically reduced once (3.11) was violated. For very large size parameters the behavior even becomes that brittle that the results approach those from linear-elastic fracture mechanics[Hill 76,Carp 86,Baza 86b].

The above parallels with the traditional smeared crack formulation can be drawn even further, since the orthotropic law of (2.6) can be demonstrated to be a special case of the strain-decomposition approach. To this end, we elaborate (2.18) in the crack coordinate system, so that for a 2D-configuration N reads

$$N = \begin{bmatrix} 1 & 0 \\ 0 & 0 \\ 0 & 1 \end{bmatrix} \qquad (3.12)$$

‡ It is often suggested that this only occurs with large-scale structures. However, in chapter 7 it will be demonstrated that steep softening is also paramount in axi-symmetric analyses, where the crack band width for longitudinal cracks increases with increasing distance from the axis of rotation.

According to Hooke's law we have for the elastic concrete

$$D^{co} = \frac{E}{1-v^2} \begin{bmatrix} 1 & v & 0 \\ v & 1 & 0 \\ 0 & 0 & \dfrac{1-v}{2} \end{bmatrix} \tag{3.13}$$

Furthermore, according to (3.2), (3.7) and (3.9) the crack constitutive matrix reads

$$D^{cr} = \begin{bmatrix} \dfrac{\mu}{1-\mu}E & 0 \\ 0 & \dfrac{\beta}{1-\beta}G \end{bmatrix} \tag{3.14}$$

where $G = E/2(1+v)$. Substituting the above expressions for N, D^{co} and D^{cr} into (2.18) yields an overall stress-strain relation which matches the orthotropic law of (2.6)[Rots 85a]. It is concluded that (2.6) is a special case of the strain-decomposition concept for an elastic-cracked material.

3.2 Multidirectional-crack parameters

3.2.1 Essentials

The traction-strain law for multi-directional cracks was introduced in (2.27) in the form of a constitutive matrix $\hat{D}^{cr}$ that relates the traction increment $\Delta \hat{t}^{cr}$ to the local crack strain increment $\Delta \hat{e}^{cr}$, whereby $\hat{}$ denotes an assembly. Ideally, this law should reflect interaction between the individual cracks via off-diagonal submatrices. However, the particular submatrices to be used in such an approach are not obvious, while it is not unthinkable that inclusion of them increases the level of sophistication to such an extent that it detracts from the practical usefulness of the concept. For this reason, the off-diagonal submatrices have been equated with zero. Consequently, $\hat{D}^{cr}$ reduces to a block-diagonal matrix[deBo 85,Rigg 86]

$$\hat{D}^{cr} = \begin{bmatrix} D_1^{cr} & 0 & \cdots \\ 0 & D_2^{cr} & \cdots \\ \cdots & \cdots & \cdots \end{bmatrix} \tag{3.15}$$

where D_i^{cr} denotes the local stress-strain matrix for crack number i. The above arguments parallel those that led to the non-coupled format of (3.2) for a single crack.

29

A further assumption is that the non-coupled format for a single crack will be maintained for each multi-directional crack, i.e. each submatrix D_i^{cr} is given zero off-diagonal terms according to (3.2). Consequently, the block-diagonal matrix reduces to a diagonal matrix.

Considering orthogonal cracks in multi-axial tension, the assumptions are justified since the state of a crack does not affect the state of an orthogonal crack. For instance, the strength limit f_{ct} is attainable in all directions[Kupf 69], while it is also plausible that the full fracture energy G_f can be consumed for each orthogonal crack. These characteristics allow each submatrix D_i^{cr} to be filled in accordance with the single-crack rules derived in the preceding section.

For non-orthogonal cracks, the situation is less obvious and the concept bears on the way in which the damage accumulated in previous cracks is transferred to the constitutive relation for the new crack. As the block-diagonal structure of $\hat{D}^{cr}$ abandons *explicit* coupling, this transfer must be provided in an *implicit* way, by assuming the properties underlying submatrix D_2^{cr} in (3.15) to depend on the state of crack 1. This section aims at deriving transparent expressions for such implicit coupling, which is an extension to the pioneering study by de Borst & Nauta[deBo 85] who isolated the material law for a certain crack from the state of previous cracks.

3.2.2 Some simplifications

The use of a non-zero shear retention factor for fixed cracks implies that the axes of principal stress rotate after crack formation. The inclined principal tensile stress may well increase although the fixed crack correctly shows softening, and it must be decided whether or not a subsequent crack is initiated. To this end, four criteria can be distinguished:

(a) the inclined principal tensile stress σ_1 again violates the maximum stress condition, i.e. $\sigma_1 = f_{ct}$,

(b) the inclination angle between the principal tensile stress and the existing crack(s) exceeds the value of a threshold angle α,

(c) both condition (a) as well as (b) are violated,

(d) either condition (a) or (b) is violated.

Although condition (a) correctly limits the maximum tensile stress, it does not limit the total number of cracks. For high values of β (e.g. $\beta=0.5$) it is imaginable that a new crack must be initiated in almost each stage of the loading process, which becomes inefficient when permanent memory is retained. The threshold-angle condition (b) obviates this deficiency, but, conversely, does not keep control of the

30

maximum tensile stress, especially for high values of α (e.g. $\alpha=60^o$). The same argument holds for condition (c), which was exemplified by a case whereby the principal tensile stress temporarily amounted to three times the tensile strength while the threshold angle condition was still not violated[Rots 85c].

To clarify this issue we need further simplifications in addition to the assumption that $\hat{D}^{cr}$ is diagonal. A first simplification is achieved by adopting elastic unloading for inactive cracks (Fig. 3.3). As explained in section 3.1.4, this option excludes inactive defects from being incorporated in $\hat{D}^{crco}$. This is attractive because experimental data reveal that only the most recently initiated defect of a system of non-orthogonal defects is active, while previous defects have become inactive[Vecc 86,Bhid 87]. Using the elastic unloading option, it becomes feasible to consider a large number of (inactive) cracks, or, put differently, to keep the threshold angle low[‡]. Assuming that all previous cracks indeed unload, the elastic unloading option implies that the block diagonal matrix $\hat{D}^{cr}$ reduces to the single-crack matrix of (3.2) for the most recently initiated defect, which in the sequel will be referred to as the *currently-active crack*.

Once a defect has become inactive, the only motive for keeping memory of its direction is to check for re-activation during a subsequent stage of the loading process. For low values of the threshold angle this approach becomes impracticable. As an alternative to re-activating an existing defect, one may decide to activate a new defect. In doing so, defect orientations can be erased from memory altogether, which provides a second simplification. As a compromise between computational costs and degree of sophistication, the threshold angle below which memory of defect orientations has been omitted was put to 30 degrees in the current implementation. For a 2D-configuration this corresponds to a maximum storage of 6 fixed cracks.

3.2.3 Implicit coupling between non-orthogonal cracks

With the above two simplifications the identification of a proper set of multi-directional crack parameters that determine the traction-strain matrix (3.2) for the currently-active crack, becomes feasible. We will propose mode I parameters (condi-

---

‡ For secant and any other type of unloading, not only the active crack but also the inactive cracks must be incorporated in $\hat{D}^{crco}$, unless they are fully closed. Considering a 2D configuration with a threshold angle of 15 degrees, a stress rotation up to 180 degrees involves 12 cracks, probably 11 of which have become inactive. The dimensions of $\hat{N}$ and $\hat{D}^{cr}$ then increase up to 3*24 and 24*24 respectively, and inverting $[\hat{D}^{cr}+\hat{N}^t\hat{D}^{co}\hat{N}]$ in (2.28) becomes computationally expensive. For 3D configurations, the approach becomes even less attractive.

tion of crack initiation, fracture energy, shape of the softening diagram) and mode II parameters successively.

The simplifications enable us to adopt the most tight condition of crack initiation, that is condition (d) of section 3.2.2, which maintains both stress control as well as orientation control. If the crack is "stress-critical", that is if it arises due to a violation of the maximum stress condition, its initial traction f_0 equals the tensile strength f_{ct}. If the crack is "threshold-critical", that is if it arises due to a violation of the threshold angle condition, f_0 is lower than f_{ct}, as indicated in Fig. 3.4. In the latter case, f_0 no longer occurs as an explicit parameter, but it is dictated by the threshold-angle condition.
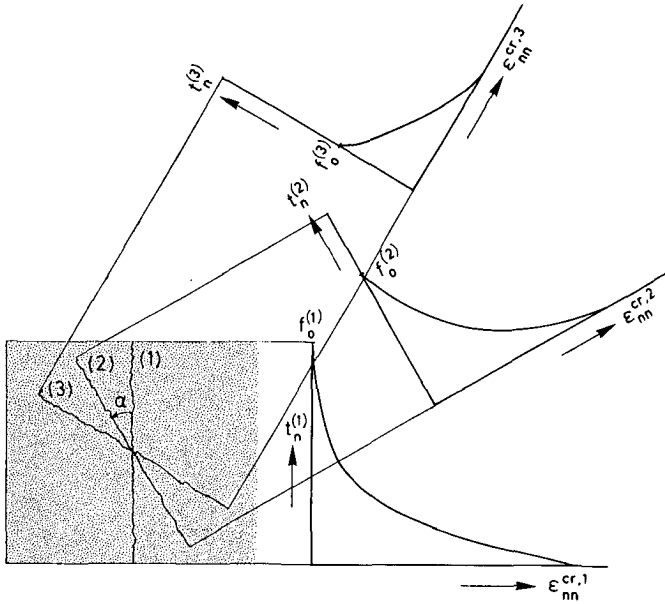
Fig. 3.4. Memory transfer in mode I softening for multi-directional cracks.
The available energy and the peak stress decrease with increasing crack number.

The fracture energy consumed in previous defects is subtracted from the energy available for the currently-active defect. The energy g_f consumed in a system of n inactive defects reads

$$g_f = h \sum_{i=1}^{i=n} \int_0^{\varepsilon_{nn}^{cl,i}} t_n^i \, d\varepsilon_{nn}^{cr,i} \tag{3.16}$$

where $\varepsilon_{nn}^{cr,i}$ is the normal strain of crack i, $\varepsilon_{nn}^{cl,i}$ is the normal strain of crack i at closing, t_n^i is the normal traction of crack i and h is the crack band width which is

32

assumed to be the same for all cracks. The energy available for crack $n+1$ is then assumed to be $(G_f - g_f)$. This procedure, which is illustrated in Fig. 3.4, does not relate the fracture energy to a particular orientation, i.e. G_f is not conceived to be a vector as previously suggested[deBo 86]. When full memory is retained, (3.16) can be readily evaluated since tractions and strains for all cracks, including arrested ones, are permanently available. When full memory is omitted, (3.16) must be stored and updated by adding the contribution of the preceding-active crack before making it inactive and erasing it from memory. In the latter case, the storage of (3.16) serves as "overall memory" of the damage accumulated in the system.

The shape of the softening diagram for subsequent cracks has been defined as the residual portion of the "mother" diagram, i.e. that portion of the initial, single crack diagram that lies beyond f_0. This scheme is sketched in Fig. 3.4 and is essential with concave-shaped softening. When each subsequent crack would be assigned the same diagram as the first crack, the softening would always start with a steep slope. Such would be incorrect because it prevents the tail of the concave diagram from being effectuated.

In a previous study the shear stiffness across active cracks as well as inactive cracks was reduced, resulting in a rapid decrease of the overall shear capacity of the multiply-cracked system[deBo 85]. Adopting elastic unloading, only the shear stiffness across the active crack is reduced, while across the inactive cracks elastic shear capacity is re-inserted. In this case, application of a constant shear retention factor β, or, equivalently, a constant crack shear modulus D^{II}, would not account for the damage accumulated via previous cracks. It is more correctly to assume β for the currently-active crack to be a function of the crack history. To this end, the crack strain accumulated in inactive defects is recorded:

$$\varepsilon^{cr,inactive} = \sum_{i=1}^{i=n} N_i e_i^{cr} \tag{3.17}$$

where n is the number of inactive defects. From this vector, we calculate the principal tensile crack strain ε_{11}^{cr}, which serves as an overall damage indicator, like g_f of (3.16). Following the procedure for a fixed single crack the shear retention factor for the currently-active crack is made a decreasing function of ε_{11}^{cr}. For instance, the multiple crack analogy of (3.8) becomes

$$\beta = \left[1 - \frac{\varepsilon_{11}^{cr}}{\varepsilon_u^{cr}} \right]^p \tag{3.18}$$

where ε_{11}^{cr} replaces ε_{nn}^{cr}. When ε_{11}^{cr} exceeds ε_u^{cr}, the shear retention factor of (3.18) vanishes and the principal stress ceases to rotate. This scheme implies the crack to be

truly fixed upon mode I softening completion, i.e. upon the stage where the micro-cracks coalesce into a continuous macro-crack. The subtle difference with a single crack lies in the fact that the shear stress across the latest multiple crack is only small, while the shear stress accumulated across a single crack may be significant.

3.3 Rotating-crack parameters

Having constructed constitutive relations for multi-directional cracks, the step towards the coaxial rotating crack concept as the limit of the fixed multi-directional concept becomes straightforward. Specifically, we assume

— a zero-threshold angle, and
— rigorous elastic unloading for inactive cracks,

which leads to a situation of a continuously rotating active crack. Again, overall memory of fracture energy is preserved and the mode I relation for the currently-active crack is set up along the above lines.

The deviation now lies in the use of a specific mode II relation for the currently-active crack. As indicated in section 2.2.4, the overall shear stiffness βG which enforces coaxiality between principal stress and strain for the 2D rotating crack con-cept is

$$\beta G = \frac{(\sigma_{11} - \sigma_{22})}{2(\varepsilon_{11} - \varepsilon_{22})} \tag{3.19}$$

According to (3.7) this leads to the following crack shear modulus for the currently-active crack:

$$D^{II} = \frac{(\sigma_{11} - \sigma_{22})\,G}{2(\varepsilon_{11} - \varepsilon_{22})G - (\sigma_{11} - \sigma_{22})} \tag{3.20}$$

It is recalled from section 2.2.5 that an inner iteration loop is employed to prevent drifting from the coaxiality condition as induced by finite increments of strain. In the first inner iteration the principal 1,2 indices refer to the configuration at the beginning of the load step, i.e. to the current crack axes. In subsequent inner iterations they refer to the configuration beyond the previous inner iteration.

Conditions of multi-axial tension with shear may involve multiple rotating cracks. Since coaxiality is preserved, such cracks are by definition mutually orthogonal since they follow the axes of principal strain. The memory indicators of (3.16) and (3.17) must then be stored for each rotating crack direction. By virtue of the strain-decomposition, a shear reduction for two orthogonal cracks implies βG to be given by

34

$$\frac{1}{\beta G} = \frac{1}{G} + 2\frac{1}{D^{II}} \tag{3.21}$$

As βG again must satisfy (3.19), the crack shear moduli D^{II} for the two orthogonal rotating cracks must be taken twice the value required for a single rotating crack in order to enforce coaxiality.

While previous defects are assumed to unload elastically, possible unloading of the current (latest) defect need not be assumed to be elastic. Unloading of the current defect occurs if the continuum with the rotating crack undergoes overall unloading. We identify such a case if the crack strain increment for the current defect is calculated to be negative. When elastic unloading is assumed, all information can then be erased from memory, except for the current principal tensile stress which is stored in order to check for initiation of a new defect during a subsequent stage. Coaxiality is automatically preserved because subsequent behavior is elastic. When secant or any other type of unloading is assumed, the defect is treated in the same manner as an active defect. Hence, the coaxiality-enforcing mode II relation must be maintained during the unloading phase, as well as during a possible re-loading or re-softening phase. The mode I softening relation is replaced by the unloading relation and the negative crack strain increment for the defect gives rise to a decrease of the overall principal crack strain ε_{11}^{cr}.

It is no longer necessary to reserve the term "rotating crack" for models that preserve coaxiality between principal stress and strain. This is because the fixed multi-directional crack concept covers a wide spectrum of stepwise-rotating non-orthogonal cracks, which also permits crack shear relations different from the one enforcing coaxiality to be employed. The objections[Baza 83b] raised against rotating crack models with loss of coaxiality do not hold when such models are conceived as a special case of the multi-directional fixed crack concept[deBo 86]. This is because each fixed crack is assigned a stress-strain relation in its own fixed coordinate system, rather than using a rotating principal stress-strain relation.

3.4 Tension-shear model problem

To verify the elastic-softening formulations for single cracks, multi-directional cracks and rotating cracks, reference is made to the plane-stress model problem of biaxial tension and shear depicted in Fig. 3.5. It concerns an elastic-softening continuum of unit dimensions with Young's modulus $E=10000$ N/mm^2, Poisson's ratio $\nu=0.2$, tensile strength $f_{ct}=1.0$ N/mm^2 and a linear strain-softening diagram with an ultimate strain ε_u^{cr} which equals three times the elastic strain at peak-strength, i.e. $\varepsilon_u^{cr}=0.0003$,

corresponding to a fracture energy G_f=0.15 J/m^2 over unit crack band width h=1.0 mm. The elastic unloading option has been adopted. Initially, the continuum is subjected to tensile straining in the x-direction accompanied by lateral Poisson contraction in the y-direction, i.e. $\Delta\varepsilon_{xx} : \Delta\varepsilon_{yy} : \Delta\gamma_{xy} = 1 : -\nu : 0$. Immediately after cracking, a switch is made to combined biaxial tension and shear according to $\Delta\varepsilon_{xx} : \Delta\varepsilon_{yy} : \Delta\gamma_{xy} = 0.5 : 0.75 : 1$, involving the axes of principal strain to continuously rotate after crack formation as is typical of fracture propagation in smeared finite element models. This scheme was inspired by work of Willam et al.[Will 87].
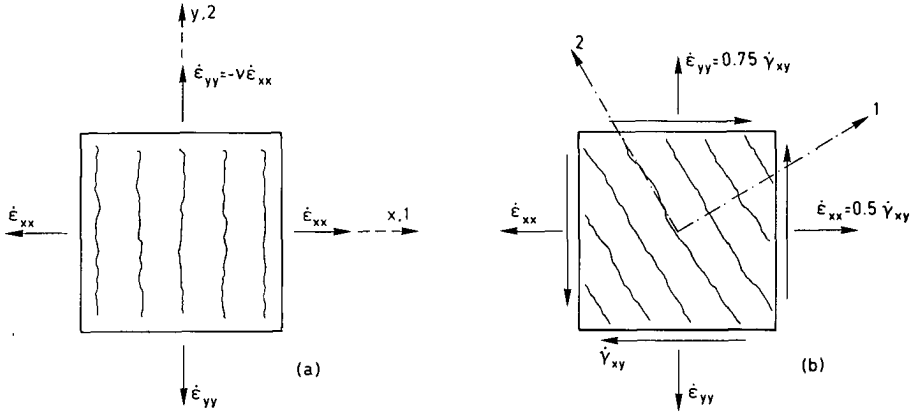
Fig. 3.5. Lay-out of tension-shear model problem.
(a) tension up to cracking; (b) biaxial tension with shear beyond cracking

The focus is placed on a variation of the threshold angle α, while the mode II relation across the currently-active crack is kept fixed in the form of a quadratic degradation of β with increasing principal tensile crack strain according to (3.18) with p=2. The adopted values of α range from 0, 7.5, 15, 30, 45 up to 90 degrees. The extreme of α=0° corresponds to a continuously rotating crack (not maintaining coaxiality, however) and the other extreme of α=90° corresponds to a fixed single-crack. In addition, the problem was analyzed using the coaxial rotating crack model, i.e. for threshold angle α=0° and β enforcing coaxiality according to (3.19).

The nominal $\tau_{xy} - \gamma_{xy}$ shear response predicted is shown in Fig. 3.6. The two computations for a zero threshold angle provide the most flexible response, whereby the condition of coaxiality gives rise to an even lower maximum shear stress than the crack-strain decreasing shear retention function. In addition, these two computations show curves that are nicely smooth as a result of the continuously changing orientation of the crack. Upon increasing the threshold angle the response becomes less flexible and we observe increasing discontinuity as a result of the interval adaptation of the currently-active crack orientation to the continuous rotation of principal stress.
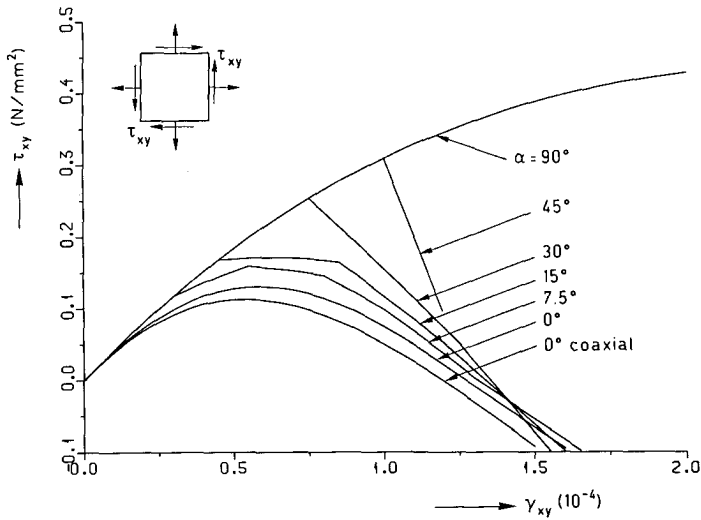
36

Fig. 3.6. Shear stress-strain response in x,y direction, for different
threshold angles α between multi-directional cracks.

For threshold angles beyond 45° the initiation of inclined cracks is postponed
even further and the solution approaches the fixed single-crack solution for $\alpha=90^o$,
which is extremely stiff.

The observation of stiff behavior for fixed-single cracks corresponds to previous
findings[Will 87,Cris 87,Koll 87,Rots 87e]. The present results indicate that a crack-strain decreas-
ing shear retention function does not provide a remedy. It is intriguing that the results
in Fig. 3.6 for threshold angles less than 90^0 invariably do display shear softening
along the x,y-plane of initial cracking. *This shear softening occurs implicitly,* as a
consequence of the threshold-angle control of multi-directional cracking and of the
transfer of crack memory to the softening law for the currently-active crack[†].

The discrepancies further become manifest on plotting the principal tensile stress
σ_{11} against the principal tensile strain ε_{11}, as shown in Fig. 3.7. Note that the direc-
tions of these identities are not aligned, except for the coaxial rotating crack result.
The fixed-single crack curve ($\alpha=90^o$) is very illustrative as it shows σ_{11} to decrease
only slightly beyond crack initiation, whereafter it re-starts to increase and amply

---

† When maintaining the concept of fixed single cracks, the unpleasant feature of stiff behavior can
only be eliminated by adding *explicit* shear-softening, i.e. by prescribing a mode II shear softening
diagram for the fixed plane[Rots 87e]. However, the result is then very critical to the particular diagram
adopted, which is unfortunate since experimental data are lacking. Crack rotation is to be preferred.
The associated *implicit* possibility of shear softening along the x,y-plane of initial cracking is driven
by the well-controlled principal stress/strain situation. The point is that it is more logical to
interpret shear stress as the 'consequence' than as the 'cause' of principal stress.
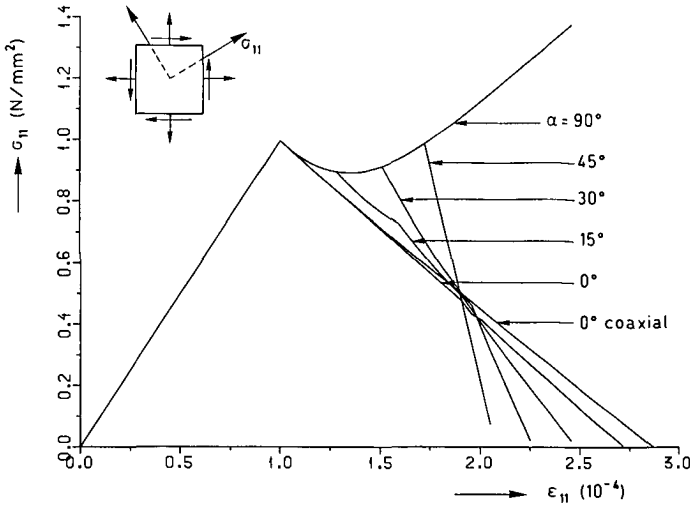
37

Fig. 3.7. Principal tensile stress-strain response in 1,2 direction, for different threshold angles α between multi-directional cracks.

exceeds the tensile strength. On decreasing the threshold angle, inclined cracks arise and the tensile strength is correctly kept under control, which is reflected by the truncation of the fixed single crack curve. The curve for coaxial rotating cracks replicates the input softening diagram[‡], which indicates that *the present conception of the coaxial rotating crack concept as the limit of the fixed multi-directional crack concept correctly resembles the approach of rotating principal stress-strain relations whereby the softening is monitored explicitly in the principal axes.*

The associated $\sigma_{xx}-\varepsilon_{xx}$ response normal to the plane of initial cracking is shown in Fig. 3.8. Here, the fixed-single crack result instead of the coaxial rotating crack result replicates the input softening diagram[‡] since it monitors the softening explicitly in the fixed crack axes whereby the shear component does not affect the normal component because of zero off-diagonal terms in D^{cr}. For threshold angles less than 90° shear-normal coupling occurs implicitly due to inclined cracking, which results in a rapid degradation of σ_{xx} beyond peak stress. *This demonstrates that crack rotation, either stepwise or continuous, offers an attractive alternative to the complicated issue of assessing direct shear-normal coupling terms for a fixed single crack.*

---

‡ It is curious that the ultimate *total* strain computed shows a slight deviation from the input value of the ultimate *crack* strain $\varepsilon_u^{cr}=0.0003$. Obviously, the *concrete* strain ε_{nn}^{co} normal to the crack has become slightly negative, which is due to the fact that Poisson's effect is fully retained after cracking.
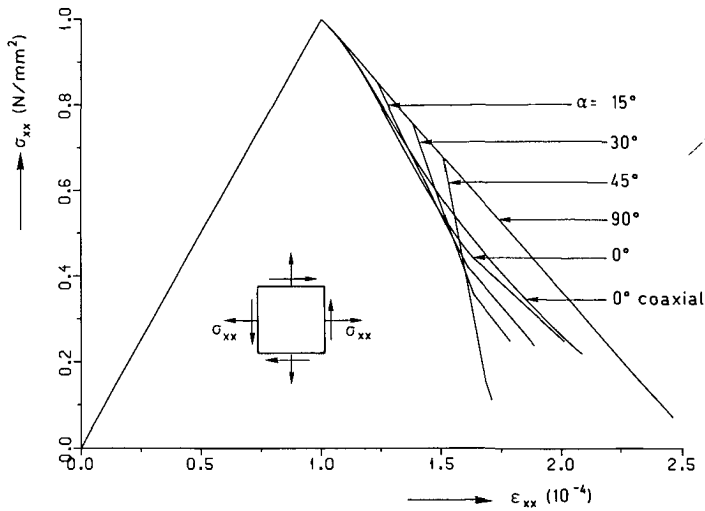
38

Fig. 3.8. Normal stress-strain response in x direction, for different
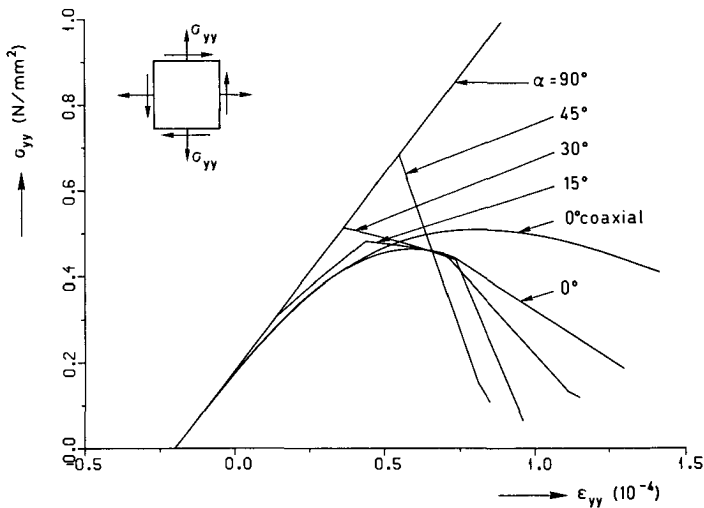threshold angles α between multi-directional cracks.

Fig. 3.9. Normal stress-strain response in y direction, for different
threshold angles α between multi-directional cracks.

The $\sigma_{yy} - \varepsilon_{yy}$ response in the lateral direction is shown in Fig. 3.9. Again, the fixed
single-crack result forms an upperbound, which partially explains the observation of
excessive orthogonal cracking in smeared analyses[Leib 86]. Crack rotation, either step-
wise or continuously, removes this behavior and correctly shows degradation of
strength in the lateral direction.

39
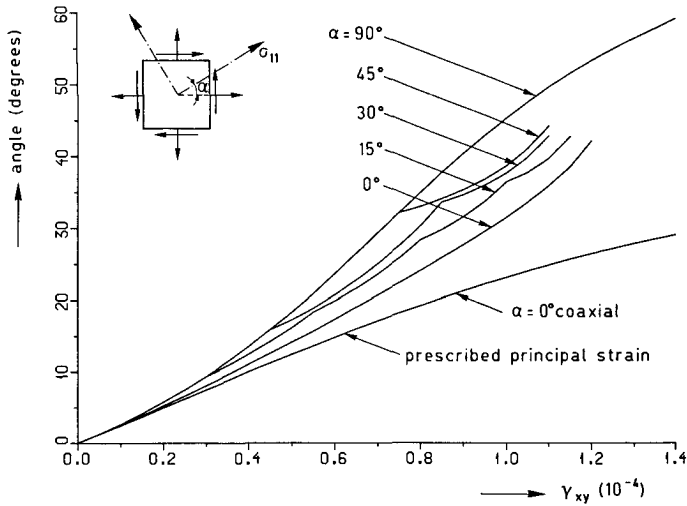
Fig. 3.10. Rotation of principal tensile stress axis, for different
threshold angles α between multi-directional cracks.

Fig. 3.10 compares the rotation of principal stress to the prescribed rotation of principal strain. Only for the coaxial rotating crack concept the axes of principal stress and strain coincide, while for all other computations the principal stress rotates much quicker than the principal strain. The fixed single-crack result provides the extreme.

It is interesting to a posteriori extract the equivalent shear retention function from the output for the coaxial rotating crack result, i.e. the development of the $(\sigma_{11}-\sigma_{22})/2(\varepsilon_{11}-\varepsilon_{22})$ history with increasing straining. The result is shown in Fig. 3.11 and indicates β not only to rapidly decrease, but even to become negative, which explains the flexible response predicted. It underlines that the shear softening occurs implicitly as a result of the principal stress and strain situation.

From among the variety of mode II relations and threshold angles to be inserted, some additional combinations were examined. For instance, the crack-strain decreasing shear retention function was replaced by a constant shear retention factor of 0.2 or 1.0, the latter one of which induces pure mode I defects along the line of Litton's model[Litt 74]. However, these analyses suffered from lack of realism since the principal stress continued to excessively rotate, also beyond the stage where the fracture energy was fully exhausted. Another combination investigated was the coaxiality-enforcing mode II relation of (3.17) with a non-zero threshold angle instead of a zero threshold angle. This attempt remained without success either, since the drift from the coaxiality condition could not be kept under control.
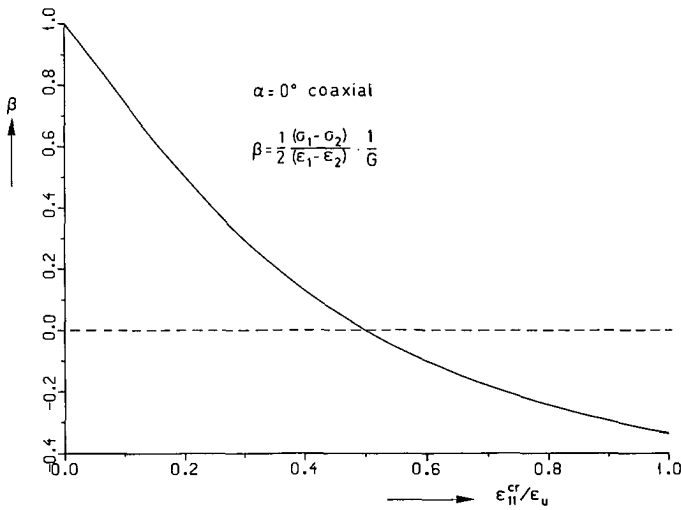
40

$\alpha = 0°$ coaxial

$$\beta = \frac{1}{2} \frac{(\sigma_1 - \sigma_2)}{(\varepsilon_1 - \varepsilon_2)} \cdot \frac{1}{G}$$

Fig. 3.11. Development of equivalent shear retention factor β for coaxial rotating
crack result (extracted a posteriori according to Eq. 3.19).

3.5 Conclusions

Constitutive formulations have been presented of tensile softening and shear reten-
tion for fixed single, fixed multi-directional and rotating cracks. Their performance
has been verified for an elementary tension-shear model problem that covers the cru-
cial issue of stress rotation after fracture. The main conclusions are:

— When proper transfer of damage memory is included, the fixed multi-
   directional crack concept provides the bridge between the two extremes of
   the fixed single-crack concept and the coaxial rotating crack concept.
— Fixed single cracks produce stiff response, even if the shear retention factor
   decreases with increasing crack normal strain.
— Multi-directional cracks and rotating cracks produce flexible response and
   correctly keep the maximum tensile stress under control.
— Multi-directional cracks and rotating cracks can implicitly provide for shear
   softening across the plane of initial cracking.
— Multi-directional cracks and rotating cracks justify the assumption of zero
   off-diagonal terms in the crack matrix of (3.2), because they provide for
   shear-normal coupling implicitly.

The next step is to proceed with the verification for fracture in element assemblies.
This extension is made in chapter 6.

41

4. ISSUES OF FINITE ELEMENT APPROXIMATION

In the present study, the behavior of cracked continua is approximated by means of finite element discretization. The term *approximation* should be stressed since the outcome for the discretized system is affected by the types of finite elements, interpolation schemes, integration schemes and by the arrangement of the mesh. When softening models are utilized, wrong choices easily disturb the solution or make it overly mesh-sensitive.

The aim of this chapter is to address these issues and to provide guidelines for optimal use of finite elements in fracture analysis of heterogeneous materials. Attention is paid to smeared cracking as well as discrete cracking, including bond. Before that, general comments will be made on the adopted solution procedures. For the finite element formulations the reader is referred to text books[Zien 77,Bath 82] and documentation of the computer program[deWi 87,deWi 88].

4.1 Solution procedures

A finite element strategy interpolates the continuous displacement field with a finite number of nodal displacements, compiled in a vector a. Application of the principal of virtual work provides a set of equations that are nonlinear if material nonlinearities and/or geometrical nonlinearities are involved. The present study considers material nonlinearities, while it excludes geometrical nonlinearities. The latter assumption is justified since we do not consider slender beams or shells, but plane-stress and axi-symmetric problems.

An incremental-iterative procedure is required to solve the nonlinear equations. Within a load increment iterations are applied and the incremental displacement vector Δa_{i-1} in iteration number $i-1$ is improved to give Δa_i after the i th iteration via the correction δa_i:

$$\Delta a_i = \Delta a_{i-1} + \delta a_i \tag{4.1}$$

The correction follows from (e.g.[Cris 81,Ramm 82,deBo 86])

$$\delta a_i = K_{i-1}^{-1} \left[\Delta\lambda_i q + p_{i-1} \right] \tag{4.2}$$

In (4.2), K_{i-1} is the stiffness matrix[Zien 77,Bath 82] after the previous iteration, $\Delta\lambda_i$ is the value of the load increment, q is a normalized load vector, and p_{i-1} is the total load vector at the end of the previous loading step minus the vector of internal forces at the end of the previous iteration. The value of q is fixed while p_{i-1}^i depends on a via the nonlinear constitutive laws. The iterative process is repeated until p_{i-1} balances $\Delta\lambda_i q$

within some convergence tolerance.

A first way of controlling the process is to prescribe the increment $\Delta\lambda_i q$. A disadvantage of such *load-control* is that it cannot pass limit points of horizontal tangent in the load-displacement space. As a remedy, one may use *direct displacement-control* and increment certain components of a. The prescribed components are transferred to the righthand-side, while the other components and the load level are solved from the reduced set which is generally well-conditioned. The approach suffers from a lack of generality since only a limited number of engineering problems permit modeling via prescribed displacements. Furthermore, direct displacement control is incapable of passing limit points of vertical tangent ('snap-backs').

The *arc-length* method, introduced by Riks[Riks 79], overcomes the deficiencies. It treats the load increment parameter $\Delta\lambda_i$ as an additional variable, the value of which is determined from a constraint equation on the incremental displacements. In order to prevent the banded symmetry of the system from being destroyed, a two-stage solution strategy has been proposed[Cris 81, Ramm 82]. First, δa_i is decomposed into two parts:

$$\delta a_i = \Delta\lambda_i \delta a_i^I + \delta a_i^{II} \tag{4.3}$$

δa_i^I belongs to the first righthand-side vector of (4.2),

$$\delta a_i^I = K_{i-1}^{-1} q \tag{4.4}$$

and δa_i^{II} belongs to the second righthand-side vector of (4.2),

$$\delta a_i^{II} = K_{i-1}^{-1} p_{i-1} \tag{4.5}$$

Subsequently, $\Delta\lambda_i$ is solved by substituting δa_i^I and δa_i^{II} into the constraint equation.

The importance of arc-length schemes for softening analyses of localized fracture was noticed by Crisfield[Cris 82] and de Borst[deBo 86]. Recommendations for the constraint equation show a departure. Crisfield[Cris 81] uses the norm of the incremental displacements as the constraint equation:

$$\Delta a_i^T \Delta a_i = \Delta l^2 \tag{4.6}$$

where Δl is the arc-length of the equilibrium path in the displacement space. Ramm[Ramm 82] linearized (4.6) so as to iterate on a "normal plane" instead of on a "spherical arch". Updating the normal plane after each iteration gives

$$\Delta a_{i-1}^T \delta a_i = 0 \tag{4.7}$$

Substitution of (4.3) into (4.7) yields the load parameter as the quotient of two inner products:

$$\Delta\lambda_i = -\frac{\Delta a_{i-1}^T \delta a_i^{II}}{\Delta a_{i-1}^T \delta a_i^{I}} \tag{4.8}$$

De Borst[deBo 86,deBo 87a] reported (4.8) to fail in case of strong localizations. As an alternative, he constructed the iterative plane from only a selected number of the components of a_i. In doing so, limit points and even very sharp snap-backs associated with localized failure were traceable. In problems of fracture propagation an adequate selection is often provided by two displacement components at either side of the active crack, preferably at its tip. Subtracting these components leads to the Crack Opening Displacement (COD) as a scalar control parameter. Equation (4.8) then becomes

$$\Delta\lambda_i = -\frac{\delta COD_i^{I}}{\delta COD_i^{II}} \tag{4.9}$$

This constraint has been employed with most examples in this thesis. It is necessary in the load step that passes a limit point, whereas on an ascending or descending path (4.8) is often adequate. The use of constraints like (4.9) is in essence a return to the incremental displacement algorithm by Batoz & Dhatt[Bato 79] and the name *indirect displacement control* has been coined for the procedure[deBo 86].

In the preceding, the term limit-point was introduced. Such a peak in the load-displacement space may occur when the determinant of the tangential stiffness matrix becomes zero,

$$\det(K) = 0 \tag{4.10}$$

or, equivalently, if at least one eigenvalue of K vanishes. With incremental analyses of discretized systems, such a point where the stiffness matrix becomes exactly singular is extremely unlikely to occur. Instead, one will always *pass* a limit point and notice that the lowest eigenvalue has become negative. Such cases are warned for during the Gaussian triangularization of the stiffness matrix, since at least one negative pivot will be signaled (provided that the matrix is symmetric). In conjunction with an arc-length scheme the load must be subsequently decremented in order to trace the descending path. When the limit point corresponds to a valley in the response, these considerations hold in a converse manner.

A negative eigenvalue of K does not necessarily imply the pass of a limit point. It may also imply the pass of a bifurcation point, i.e. a point where the uniqueness of the solution ceases to hold[Riks 79,Ramm 82,Cris 82,deBo 86]. In some cases, these bifurcations are explainable from the constitutive model in conjunction with the boundary conditions, whereas in other cases they relate to spurious finite element behavior.

K_{i-1} in (4.2) may be either updated after each iteration (Newton-Raphson) or fixed after the first iteration (Modified Newton-Raphson). In the vicinity of limit points, the former method turns out to be essential, while on an ascending or descending path the modified method is often adequate. In "times of trouble" due to alternative equilibrium states or spurious modes, it may be sensible to temporarily freeze the stiffness matrix, or to employ some positive definite matrix that is inconsistent with the righthand-side vector, for instance the linear-elastic matrix or a matrix that is composed of the positive unloading moduli instead of the negative softening moduli. For reinforced concrete problems[Cedo 77,Rots 85a] and rotating crack problems[Milf 84] such techniques have been reported, but care should be taken since they ignore not only spurious snaps, but also possible snaps of a physical nature. Unless specifically mentioned, these techniques will not be resorted to.

4.2 Finite elements in smeared crack analysis

We consider a typical problem whereby the crack propagates through the mesh in a zig-zag manner. It concerns a Crack-Line-Wedge-Loaded Double-Cantilever-Beam (CLWL-DCB) which has been tested by Kobayashi et al.[Koba 85] (Fig. 4.1). The specimen of 50.8mm thickness is assumed to be in a state of plane stress, and is subjected to a wedge load F_1 as well as a diagonal compression load F_2. The ratio of the diagonal force to the wedge force is kept approximately constant at 0.6 until a predetermined diagonal force of 3.78 kN is reached, whereafter the diagonal force is kept constant and only the wedge force alters. The diagonal force is applied under load control and the wedge load under direct wedge opening displacement control[‡]. The loading scheme implies that the notch tip is in a state of tension-tension. The fracture propagates in mode I from the notch towards the upper-right corner[Koba 85] (Fig. 4.1b).

Comparisons between the various concepts and constitutive formulations will be made in chapter 6. Here, invariably the rotating smeared crack concept has been adopted, with the nonlinear softening function of Fig. 3.1, a tensile strength f_{ct}=3.0 N/mm^2 and a fracture energy G_f=100 J/m^2. The elastic properties have been assumed to be Young's modulus E=30000 N/mm^2 and Poisson's ratio ν=0.2.

---

‡ Pilot computations[Rots 87b] were performed using the arc-length scheme, which is capable of passing snap-back phenomena, either spurious or not. Those computations did not detect a non-spurious snap-back in the sense of catastrophic or unstable softening, but showed a number of tiny, spurious snap-backs which appeared as a result of the finite element discretization. However, for the present problem the detection of these spurious snap-backs by arc-length schemes was judged to be a disadvantage rather than an advantage, since it would require each of these phenomena to be traced in a delicate manner by alternate incrementation and decrementation of the load. In the final computations we therefore preferred direct displacement control, which allows for the possibility of jumping over spurious snap-behavior.
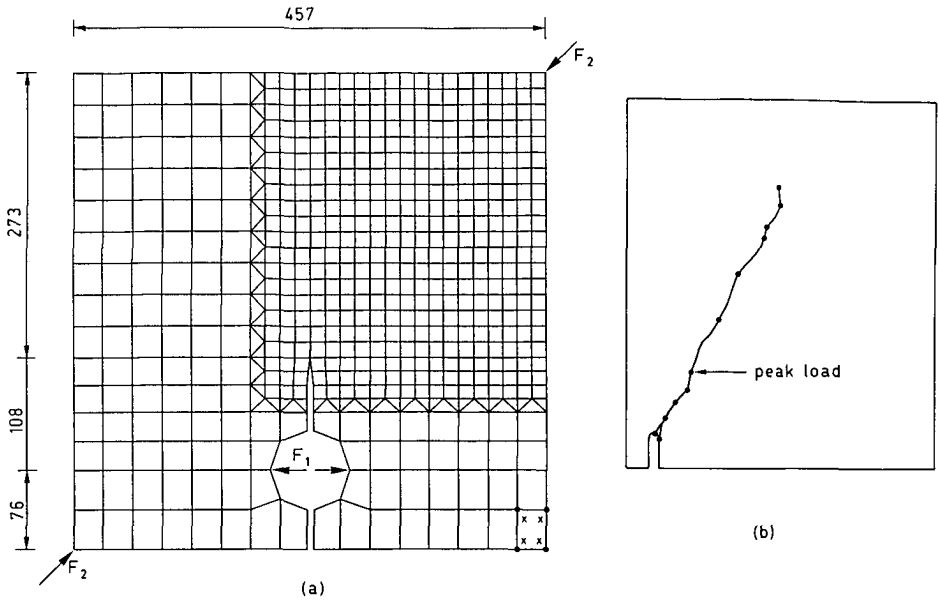
Fig. 4.1. (a) Four-node quadrilateral finite element idealization of notched CLWL-DCB specimen, dimensions in mm; (b) experimental result[Koba 85].

4.2.1 Element shape, interpolation and integration

The section compares four meshes, composed of four-node quadrilaterals with two-by-two Gaussian integration (Fig. 4.1), three-node constant-strain triangles with single-point integration, six-node linear-strain triangles with seven-point Gaussian integration and eight-node quadrilateral serendipity elements with three-by-three Gaussian integration. In order to avoid any discrepancies outside the fracture zone, the part of the mesh outside of the upper-right corner was kept unchanged. For all meshes, four-node quadrilaterals were used in this region. Only in the upper-right corner, that is in the refined part of the mesh of Fig. 4.1, the element type was varied, whereby the quadratic elements were taken twice as large as the linear elements in order to keep the computational costs fairly constant. Dependence relations were inserted to maintain compatibility along the transition lines between linear and quadratic elements.

Figs. 4.2 to 4.5 present computational results in the form of ultimate crack patterns and incremental deformations for the various meshes.

46
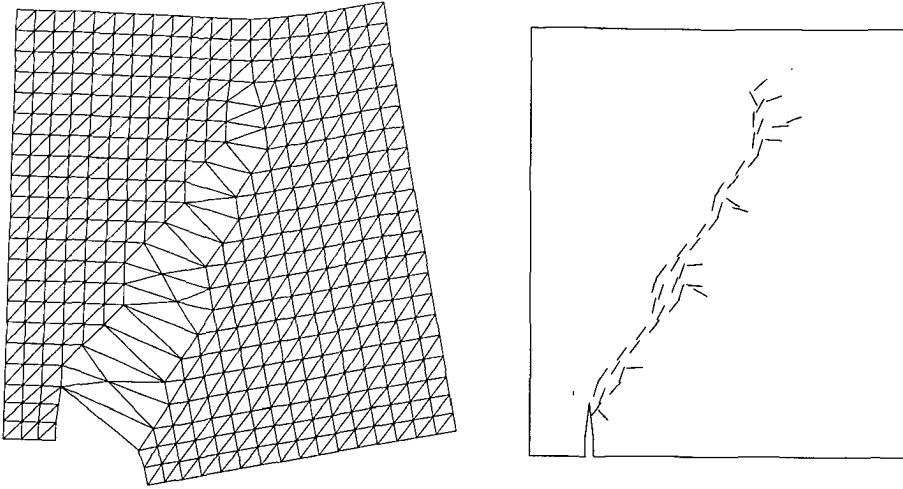
Fig. 4.2. Result for three-node triangles (CLWL-DCB specimen).
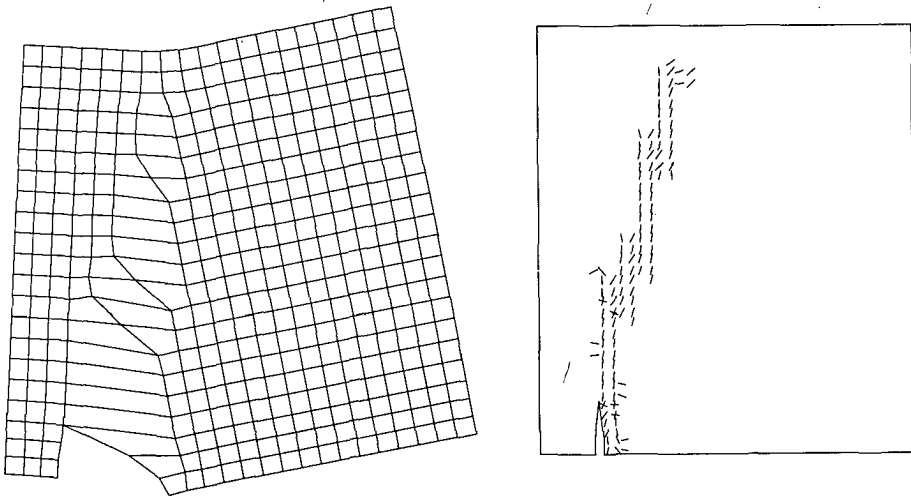
Fig. 4.3. Result for four-node quadrilaterals (CLWL-DCB specimen).

-degree of localization-

All element types are capable of simulating the fracture localization, whereby for similar computational costs, the lower order elements produce the most narrow failure band. The constant-strain triangles are adequate in this respect, because they can be integrated using a single-point scheme and because they permit the fracture to jump to adjacent rows of elements without spreading the corresponding deformation to a substantial neighboring area. Four-node quadrilaterals are slightly less attractive, owing to coupling between integration points and interlocking between the squares.

47
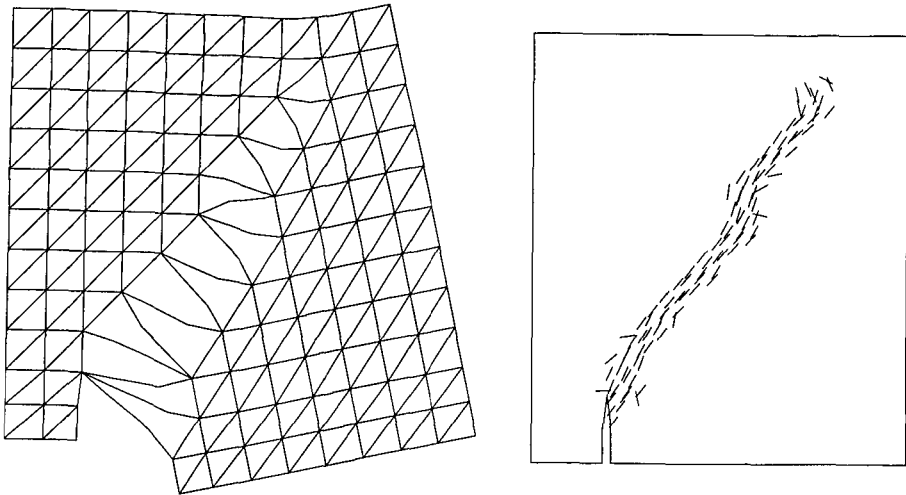
Fig. 4.4. Result for six-node triangles (CLWL-DCB specimen).
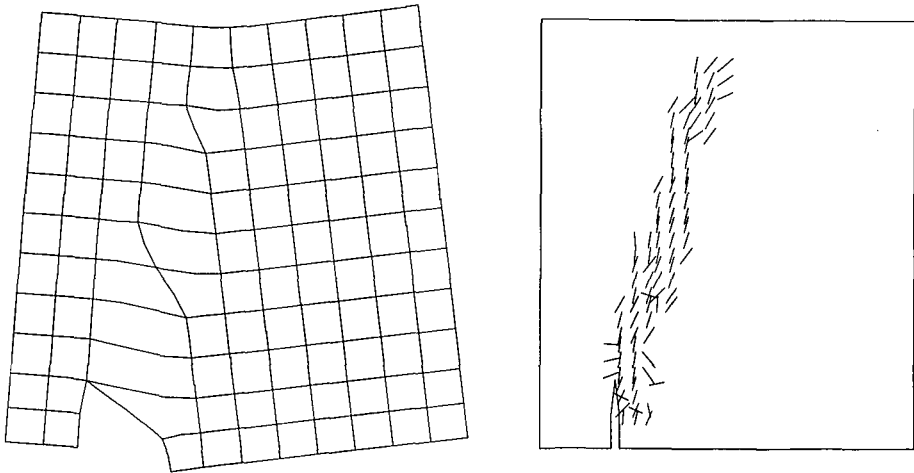
Fig. 4.5. Result for eight-node quadrilaterals (CLWL-DCB specimen).

The same holds true for quadratic elements, where the localization is smoothed over even more integration points. These differences relate to the fact that the smeared concept is an artifice that aims at imitating the limit of the discrete concept. Since a discrete crack involves "infinite strain over zero length", it is approximated more closely by constant strain over narrow bands (fine meshes with linear interpolations) than by linear strain over wider bands (coarse meshes with quadratic interpolations).

-magnitude of the crack band width-

It is recalled from section 3.1.2 that the smeared formulation of softening involves a crack band width h, which depends on the finite element configuration. In Figs. 4.2 to 4.5 this crack band width shows an effective increase at places where the fracture jumps into adjacent rows of elements. We must conclude that h is not well-defined when the fracture zig-zags through the mesh. Here, we face the fundamental consequence of the fact that softening may become manifest as an overall phenomenon for a group of integration points, rather than as a local property of an isolated integration point. It has been tried to solve this problem by incorporating the occurrence of zig-zag crack jumps in an automatic determination of h upon crack initiation[e.g.Otto 86]. However, such techniques not only tend towards over-sophistication considering current uncertainties in softening parameters[‡], but also become impracticable since they require exchange of information between neighboring elements which does not fit the nature of most existing finite element programs.

As an alternative, the spread of the softening zone was treated here in an averaged sense. We pre-specified a crude estimate of h and assumed this value to apply for all integration points along the fracture path. For the present problem, the optimal estimates of h are summarized in Table 4.I as a function of element size and type. These estimates have been found by trial-and-error fitting of the discrete crack result. The
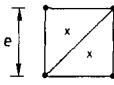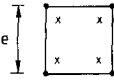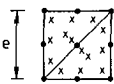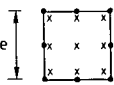
element type and integration	effective band width h for zig-zag fracture propagation through regular mesh (found by trial-and-error for present problem)
	e
	$e\sqrt{2}$
	$\dfrac{1}{2}e\sqrt{2}$
	e

Table. 4.I. Recommendations for estimating the crack band width.

---

‡ By virtue of (3.5), h quantitatively plays the same role as G_f. Section 5.2 demonstrates that the role of G_f is less important than the role of the two remaining softening properties (f_{ct} and the shape of the softening diagram). This alleviates the consequences of the errors and questions involved in h.
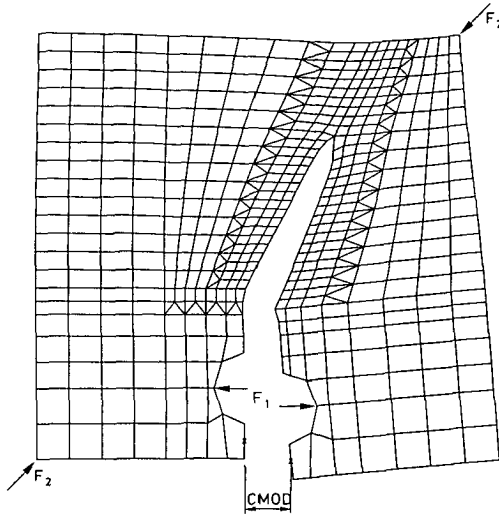
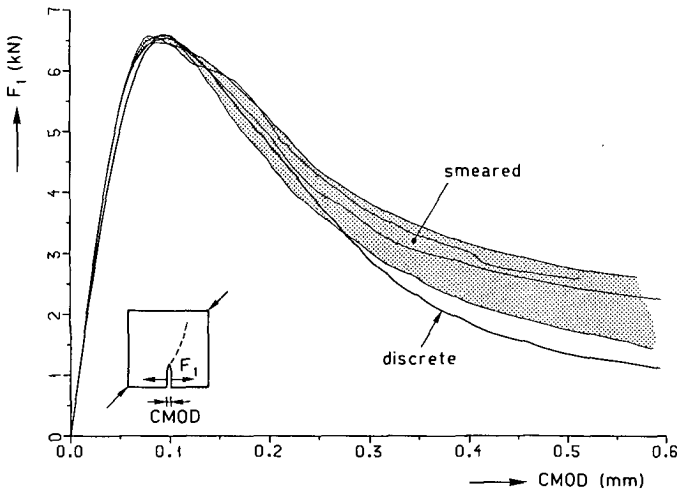Fig. 4.6. Result for predefined discrete crack (CLWL-DCB specimen).

Fig. 4.7. Load-CMOD response (CLWL-DCB specimen).

discrete crack result poses the objective reference since it releases the fracture energy exactly, without resorting to integration over a width. It was obtained for a predefined line-crack of 30° inclination (Fig. 4.6), while the material parameters were kept the same as for the smeared crack analysis. Following the guidelines of Table 4.I, the Load-CMOD curves for the four smeared crack analyses resemble the discrete crack reference fairly, as shown in Fig. 4.7. The load is the wedge load F_1, while the CMOD is the Crack Opening Displacement at the Mouth of the notch (Fig. 4.6).

50

In this thesis the coarse recommendations of Table 4.I have been followed, except for particular problems in which the fracture is aligned with the lines of the mesh. For such cases, refined recommendations[Rots 85a] have been followed.

-triangles versus quadrilaterals-

A salient feature of triangles is that their interpolations are based on complete polynomial expansions, whereas the interpolations for quadrilaterals involve surplus terms[Zien 77,Bath 82]. Since the completeness of polynomials avoids spurious strains and intrinsic directional bias, Bergan[Berg 84] motivated to favor triangles over quadrilaterals. The present experiences do not indicate this issue to be relevant, considering that the amount of spurious cracks induced by spurious strains was not appreciably higher for quadrilaterals than it was for triangles, while, in addition, the intrinsic directional bias turned out to be inferior to the extrinsic bias provided by the lines of the mesh, as will be shown in the next section.

-spurious kinematic modes-

All computations underwent critical stages in which convergence could hardly be achieved. At these stages, a negative pivot was signaled upon factorizing the tangent stiffness matrix. An eigenvalue analysis was performed subsequently, which detected a negative eigenvalue. The corresponding eigenmode represented a spurious mechanism, whereby a certain node ran out of control. This phenomenon occurred for *all* element types, as shown in Fig. 4.8.

The danger of spurious kinematic modes for softening type of constitutive models in smeared crack analysis has been noticed before. Initially, the phenomenon has been detected for quadrilaterals with reduced integration schemes[Dodd 82,deBo 85,Cris 86], while full integration schemes were thought to largely remedy the disease. More recently, spurious kinematic modes in conjunction with softening have also been reported for quadrilaterals with full integration schemes[Rots 87e,deBo 88b]. The present result supports this statement and unfortunately puts the three-node triangles with a single-point integration rule and the six-node triangles with a seven-point integration rule in the same position.

The current experiences suggest spurious modes to be susceptible for the constitutive model employed, whereby the steepness of the softening, the occurrence of multidirectional softening and the precise crack orientations play a major role. The fixed crack concept was found to be more sensitive to spurious modes than the rotating crack concept. This is explainable from the fact that a fixed direction of softening involves spurious modes to be fixed either, whereas for the rotating crack concept an existing spurious mode may well vanish in a later stage of the process owing to the continuously changing direction of material softening.
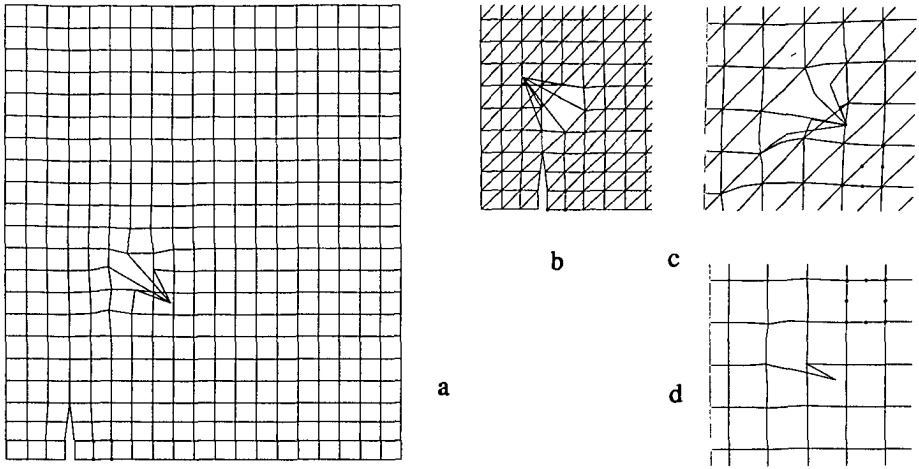
Fig. 4.8. Examples of spurious kinematic modes (CLWL-DCB specimen).
(a) four-, (b) three-, (c) six- and (d) eight-node elements.

In the latter case, problems can often, but not always, be circumvented by freezing the stiffness matrix during critical stages, whereas continuous use of the tangent stiffness scheme blows up the iterative procedure. Nonetheless, there is a strong need for stabilization techniques. The development hereof in conjunction with softening material laws is an open field of research.

The problem was re-analyzed using reduced integration techniques, like single-point integration for the four-node quadrilaterals, two-by-two Gaussian integration for the eight-node quadrilaterals and three-point integration for the six-node triangles. Unvariably, these analyses showed premature divergence as a result of hour-glass mechanisms propagating in an assembly of elements. Problems with spurious modes decrease with increasing ratio between the number of integration points versus the number of degrees of freedom. Unfortunately, this observation is at odds with the desire to spread the softening zone over as few integration points as possible.

4.2.2 Element size and orientation

In addition to the element characteristics, also their size and orientation in the mesh may have an impact on the outcome. This was recognized by Bazant & Cedolin[Baza 79] and remedied by Bazant & Oh[Baza 83a], who adapted the softening modulus D_{11}^{cr} to the crack band width in order to achieve mesh-objective results. They considered the special case of a separation band aligned with the lines of the mesh. For zig-zag crack

52

paths, objectivity studies have been reported only sporadically[Baza 83c, Rots 85a] and then the situation is less clear. This section discusses the issue for the three-node triangle, but the main conclusions also hold for the other element types.

First, twice as coarse a mesh was analyzed, so that the mesh lines are the same as for the mesh composed from six-node triangles (Fig. 4.4). The fracture localization closely resembled the localization for six-node triangles (Fig. 4.4), which is surprising since coarse meshes of three-node triangles have a bad reputation. Since the crack band width was taken twice as large as for the finer mesh, according to Table 4.I, the discrepancy between the global response for coarse and fine mesh remained within acceptable limits, as shown in Fig. 4.9. When the adaptation of the softening modulus to h is omitted, twice as much energy is consumed and the maximum load for the present problem turned out to be overestimated by 26 percent.
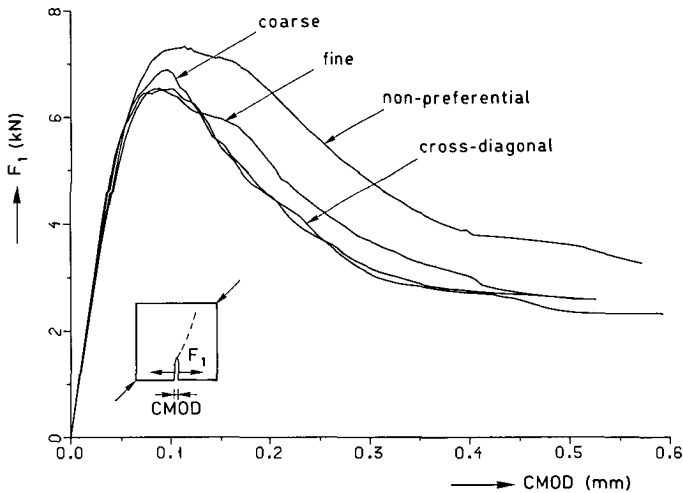

Fig. 4.9. Mesh-(in)sensitivity of Load-CMOD response for three-node triangles.

Less convincing is the objectivity with respect to element orientations. We return to the fine mesh and rotate the constant-strain triangles over 90 degrees. The direction of fracture propagation now entirely departs from the previous result, since it becomes vertical (Fig. 4.10a) instead of diagonal. We conclude that the fracture preferentially follows the lines of the mesh, which was demonstrated before for quadrilaterals[Rots 85a]. For the six-node triangles the same trend was observed. For quadrilaterals, directional bias was demonstrated to vanish upon mesh refinement[Rots 85a], but the present results do not reveal such a trend for triangles. Considering currently moderate computer facilities, the meshes considered belong to the category "fine", but the bias is unacceptable.
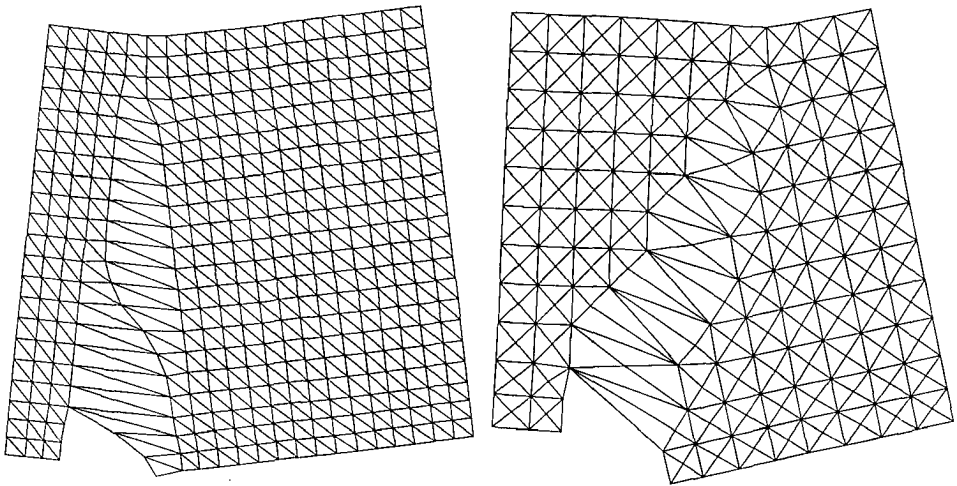
53

Fig. 4.10. Mesh-(in)sensitivity of fracture localization for three-node triangles.
(a) non-preferential mesh; (b) cross-diagonal mesh; compare to Fig. 4.2a.

Directional bias is due to the fact that strain discontinuities are represented at the element boundaries, i.e. at the lines of the mesh. A mesh composed from quadrilaterals provides only two lines, while a mesh composed from triangles provides three lines, the skew one of them being highly arbitrary however. Improvements are achieved by placing the triangles in a cross-diagonal pattern instead of a bisectional pattern, as shown in Fig. 4.10b. In doing so, symmetry is preserved and the number of lines increases up to four, which minimizes bias in locations of strain discontinuities.

4.2.3 Stress-locking as a consequence of displacement compatibility

From the Load-CMOD curves presented in the previous sections, it is concluded that the smeared crack results invariably exhibit too little overall softening. This phenomenon has been recognized before[Rots 87b] and was initially attributed to overstiffening provided by the fixed crack concept employed in that study. Extensions of the fixed crack concept by shear softening and multi-directional softening only partly remedied the disease, and the present results indicate that even the rotating crack concept - which provides the most flexible response according to the model problem of section 3.4 and further investigations in chapter 6 - overestimates the post-peak response.

To trace the underlying causes, the principal tensile stresses beyond fracture have been plotted in Fig. 4.11, both for one of the smeared crack analyses and for the discrete crack analysis. The smeared crack result corresponds to the mesh of four-

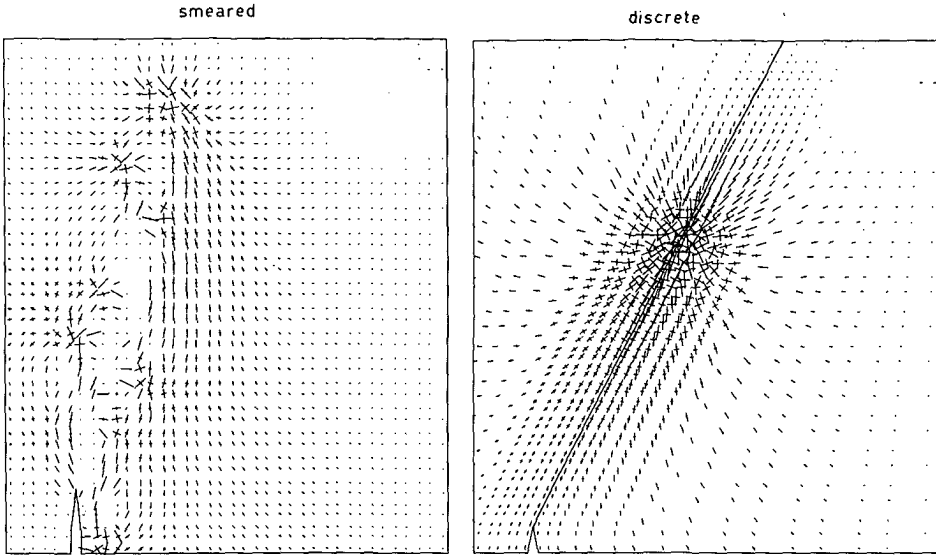smeared   discrete

Fig. 4.11. Principal tensile stress trajectories for smeared (rotating) crack result of Fig. 4.3
and discrete crack result of Fig. 4.6.

node quadrilaterals (Fig. 4.1), but it is emphasized that the other meshes produced a
very similar picture.

We observe that the discrete crack result displays a smooth stress pattern. It cap-
tures the stress rotations in the neighborhood of the crack tip with realism. Con-
versely, the smeared crack result displays a distorted pattern and does not properly
represent the stress rotations. Rather, it exhibits *locked-in stresses* at locations where
the stress should actually drop to zero.

The latter observation is a fundamental consequence of finite element displace-
ment compatibility in the smeared softening approach. If a certain element contains an
inclined crack, the strain imposed by this crack implies adjacent elements to be
strained as well, as illustrated in Fig. 4.12 where element 1 is subjected to tensile
straining due to the inclined crack at element 2. In other words, this means that ele-
ment 1 cannot be truly *separated* from element 2. Hence, while the stress at element 2
correctly softens, the stress at element 1, which is still in the elastic regime, increases.
Then, we have two possibilities: the stress at element 1 will either exceed the tensile
strength and start softening, or it will not. The former possibility is undesirable as it
discourages localization *(spurious cracking)*, but the latter possibility is undesirable
either, as the stress is locked-in *(spurious stiffening)*. Fig. 4.11 reveals the conse-
quences which are emphasized at places where the fracture zig-zags through the mesh.
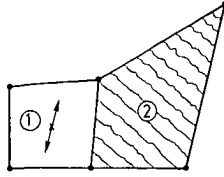
Fig. 4.12. Consequence of displacement compatibility in smeared cracking.
Strain of inclined crack at element 2 induces stress at element 1.

The above sketched behavior is obvious. Nevertheless, it has not been addressed in this way before, as far as the writer is aware of[‡]. With the present example, stress-locking becomes manifest in the post-peak regime, but for different problems like reinforced beams where several localizations occur, the phenomenon may disturb the solution already in the pre-peak regime. The phenomenon does not disappear on mesh refinement, since mesh refinement does not remove the fundamental assumption of displacement compatibility. Furthermore, stress-locking not only pertains to smeared cracking, but it may occur whenever a smeared softening approach (also softening plasticity) is used to simulate localization. For these reasons, the phenomenon is judged to be serious.

The solution must not be primarily sought in improvements of the softening laws or the smeared crack concepts, but in improvements of the finite element approximation. A possibility is to interactively align the elements with the lines of the fracture, or to remove fully strain-softened elements from the mesh, thus permitting adjacent elements to relax. However, in doing so the featuring advantage of smeared cracking as to maintaining the original finite element topology is lost, and one may quite as well resort to the discrete concept which predicts genuine separation and does not suffer from spurious stiffening since the elastic regions at either side of the discontinuity remain unstrained.

[‡] Smeared crack results are generally presented in terms of deformed meshes and crack patterns, whereas the reader is kept without detailed resolutions of stress fields. Although such presentations properly reveal localization, they hide spurious stiffening as a result of locked-in stresses.

4.2.4 Summary

The fact that the application of the smeared crack concept to cases of localized fracture is an artifice, has been shown to involve three major consequences in finite element approximations of softening and separation:

— directional bias,
— spurious kinematic modes,
— stress-locking.

These phenomena become manifest especially when the fracture zig-zags through the mesh, and occur independently of the element type (three-node and six-node triangles, as well as four-node and eight-node quadrilaterals were investigated).

The first problem must be tackled by employing very fine meshes in case of quadrilaterals[Rots 85a] and cross-diagonal patterns in case of triangles. The lower order versions of the elements provide the most economic prediction of a narrow failure band.

Techniques to overcome the latter two problems are to be developed. In the present study, the consequences are circumvented by making a predefined-discrete-crack analysis, after a smeared crack analysis has served as a predictor of the crack trajectory. Hereafter such an analysis will be referred to as discrete-crack-corrector analysis.

4.3 Interface elements for discrete fracture and bond

The modeling of geometrical discontinuities like discrete cracks in concrete, joints in rock and bond-slip layers in reinforced concrete asks for multi-purpose interface elements. We may classify these into

— continuous[Good 68,Dorr 78,deGr 81,Glem 84,Scha 75,Mehl 85,Rots 85c] interface elements, and
— lumped[NgoS 67] interface elements.

The former elements start from the notion of a continuous relative-displacement field, whereas the latter lump relative-displacement to the nodes. There is lack of clarity on the question which type of elements should be preferred. The continuous interface elements have been suggested to be superior[Nils 82], but this has not been accompanied by comparative studies.

The purpose of this section is to formulate and compare both element types. We will unfold an unpleasant deficiency of the continuous interface elements, which casts doubt on the above suggestion. Since it appeared necessary to subject the element stiffness matrices to an eigenvalue analysis, the derivation of these matrices goes into details.

4.3.1 Continuous interface elements

Consider the general case of a m-node 2D interface element which connects two solid elements, as shown in Fig. 4.13a. The element nodal displacement vector $\mathbf{a}^e$ lists $3m$ degrees of freedom,

$$\mathbf{a}^e = \left[u_n^{(1)} \ .. \ .. \ u_n^{(m)} \ u_t^{(1)} \ .. \ .. \ u_t^{(m)} \ u_s^{(1)} \ .. \ .. \ u_s^{(m)} \right]^T \tag{4.11}$$

in which $u_n^{(i)}$, $u_t^{(i)}$ and $u_s^{(i)}$ are the interface mode I (normal), mode-II (tangential) and mode-III (tangential) displacements of node i respectively.
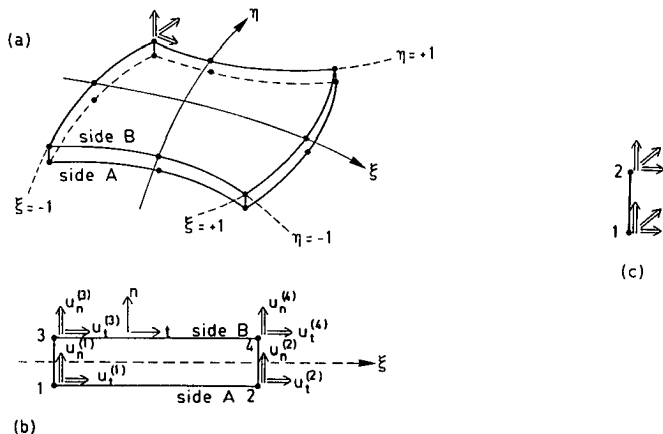

Fig. 4.13. Interface elements; (a) sixteen-node 2D interface element; (b) four-node 1D interface element; (c) two-node lumped 'point-interface' element.

The continuous displacement field $\mathbf{u}$,

$$\mathbf{u} = \left[u_n^{(A)} \ u_t^{(A)} \ u_s^{(A)} \ u_n^{(B)} \ u_t^{(B)} \ u_s^{(B)} \right]^T \tag{4.12}$$

with the superscripts A and B denoting the two interface sides, is interpolated as

$$\mathbf{u} = \mathbf{H}\mathbf{a}^e \tag{4.13}$$

$$\mathbf{H} = \begin{bmatrix} N & 0 & 0 & 0 & 0 & 0 \\ 0 & N & 0 & 0 & 0 & 0 \\ 0 & 0 & N & 0 & 0 & 0 \\ 0 & 0 & 0 & N & 0 & 0 \\ 0 & 0 & 0 & 0 & N & 0 \\ 0 & 0 & 0 & 0 & 0 & N \end{bmatrix} \tag{4.14}$$

In (4.14) the $1*(m/2)$ submatrix $\mathbf{N}$ comprises the interpolation polynomials which are most easily expressed in the normalized coordinates ξ and η along the interface[Zien 77,Bath 82].

Next, define the relative-displacement field $\Delta\mathbf{u} = [\ \Delta u_n\ \ \Delta u_t\ \ \Delta u_s\ ]^T$ as

$$\Delta\mathbf{u} = \mathbf{L}\mathbf{u} \tag{4.15}$$

with

$$\mathbf{L} = \begin{bmatrix} -1 & 1 & 0 & 0 & 0 & 0 \\ 0 & 0 & -1 & 1 & 0 & 0 \\ 0 & 0 & 0 & 0 & -1 & 1 \end{bmatrix} \tag{4.16}$$

Here, the interface elements deviate from continuum elements in that $\mathbf{L}$ contains digits instead of differential operators. It is noted that the notation Δ no longer denotes an increment, but a relative measure. Substitution of (4.13) into (4.15) yields

$$\Delta\mathbf{u} = \mathbf{B}\mathbf{a}^e \tag{4.17}$$

where the notation $\mathbf{B} = \mathbf{L}\mathbf{H}$ has been introduced for the relative displacement-nodal displacement matrix.

Finally, the constitutive matrix $\mathbf{C}$ is inserted which connects the tractions $\mathbf{t} = [\ t_n\ \ t_t\ \ t_s\ ]^T$ to the relative displacements along the lines of (2.2) to (2.4),

$$\mathbf{t} = \mathbf{C}\Delta\mathbf{u} \tag{4.18}$$

Following standard procedures[Zien 77,Bath 82], the substitution of (4.17) and (4.18) into the expression of virtual work yields the element stiffness matrix $\mathbf{K}$

$$\mathbf{K} = \int_S \mathbf{B}^T \mathbf{C}\mathbf{B}\ dS \tag{4.19}$$

with S representing the interface surface. Assuming the geometry to be interpolated in the same way as the displacements, i.e. considering an iso-parametric element, (4.19) can be rewritten as

$$\mathbf{K} = \int_{\xi=-1}^{\xi=+1} \int_{\eta=-1}^{\eta=+1} \mathbf{B}^T \mathbf{C}\mathbf{B}\ \mathrm{det}\mathbf{J}\ d\xi\ d\eta \tag{4.20}$$

with det$\mathbf{J}$ being the determinant of the $2*2$ Jacobian operator.

In the present study applications will be confined to 1D line-interfaces, involving the interpolation polynomials to reduce to functions of ξ only and the mode III

associated components of **H**, **L** and **B** to vanish. Eq. (4.20) then renders

$$K = b \int_{\xi=-1}^{\xi=+1} \mathbf{B}^T \mathbf{CB} \frac{\partial x}{\partial \xi} d\xi \tag{4.21}$$

with b denoting the interface width in the vanishing η-direction. As an example, assuming a constitutive matrix of the form

$$\mathbf{C} = \begin{bmatrix} k_n & 0 \\ 0 & k_t \end{bmatrix} \tag{4.22}$$

with k_n and k_t being constant along the interface, the stiffness matrix of the four-node continuous interface element of Fig. 4.13b with

$$\mathbf{N} = \begin{bmatrix} \frac{1}{2}(1-\xi) & \frac{1}{2}(1+\xi) \end{bmatrix} \tag{4.23}$$

can be explicitly evaluated to give

$$K = \frac{1}{6}bL \begin{bmatrix}
2k_n & k_n & -2k_n & -k_n & 0 & 0 & 0 & 0 \\
k_n & 2k_n & -k_n & -2k_n & 0 & 0 & 0 & 0 \\
-2k_n & -k_n & 2k_n & k_n & 0 & 0 & 0 & 0 \\
-k_n & -2k_n & k_n & 2k_n & 0 & 0 & 0 & 0 \\
0 & 0 & 0 & 0 & 2k_t & k_t & -2k_t & -k_t \\
0 & 0 & 0 & 0 & k_t & 2k_t & -k_t & -2k_t \\
0 & 0 & 0 & 0 & -2k_t & -k_t & 2k_t & k_t \\
0 & 0 & 0 & 0 & -k_t & -2k_t & k_t & 2k_t
\end{bmatrix} \tag{4.24}$$

Here, the degrees of freedom have been listed in the sequence of (4.1) according to the node numbering of Fig. 4.13b.

With a view to nonlinear applications (**C** being non-constant along the interface) numerical evaluation of (4.20) is preferable over explicit evaluation. The integral is replaced by a weighted sum of the values of $\mathbf{B}^T\mathbf{CB}\det\mathbf{J}$ at distinct sampling points. A two-point Gaussian scheme integrates the four-node element exactly and a three-point scheme the six-node.

4.3.2 Lumped interface elements

The essence of lumped interface elements (or 'bond-link' elements[NgoS 67]) is that the traction-relative displacement relation is evaluated at isolated node-sets instead of along an interpolated field. Considering the topology of Fig. 4.13b as an example, this means that there is no interrelation between node-set 1-3 and node-set 2-4, permitting the formulation to be confined to the smallest unit of a two-node 'point-interface' (Fig. 4.13c). The element nodal displacement vector (4.11) reduces to

$$\mathbf{a}^e = \left[\; u_n^{(1)} \; u_n^{(2)} \; u_t^{(1)} \; u_t^{(2)} \; u_s^{(1)} \; u_s^{(2)} \right]^T \tag{4.25}$$

in which the superscript (1) denotes node 1 and (2) node 2. The steps from (4.12) to (4.14) are now omitted, implying $\mathbf{B}$ to simply reduce to $\mathbf{L}$ of (4.16) which is a constant. Consequently, (4.19) can be elaborated to give

$$\mathbf{K} = A \; \mathbf{B}^T \mathbf{C} \mathbf{B} \tag{4.26}$$

with A denoting the tributary surface for the node-set.

The tributary surface A depends not only on the dimensions of the surrounding continuum elements, but also on their interpolations. The surface allocation follows the nodal allocation of a uniform surface load acting on a finite element, which for the particular case of undistorted rectangular elements corresponds to the well-known[Zien 77, Bath 82] schemes of 1/4,1/4 for the linear rectangle, 1/4,1/4,1/4,1/4 for the linear brick element, 1/6(corner node), 2/3(mid-side node), 1/6(corner node) for the quadratic rectangle and −1/12(corner node), 1/3(mid-side node), −1/12, 1/3, −1/12, 1/3 for the quadratic brick element. In an element assembly, the resulting contributions from all connected continuum elements should be added in order to ascertain the total tributary surface of the lumped point-interface element.

In the computer code it is virtually impossible to automatize surface allocation because such would require exchange of information between point-interface elements and neighboring continuum elements. Consequently, the user must somehow pre-process this operation manually which is not exactly simple for everyday applications, especially when the elements are of higher order and/or of distorted shape. It is preferable to construct lumped counterparts of the continuous interface elements as an assembly of point-interface elements. The surface tributaries can then be determined automatically, according to the shape functions which would exist for the continuous counterpart of the element. The node-sets, however, still act mutually independent and the stiffness matrix equals the sum of the individual stiffness matrices (4.26) for the underlying point-interface elements. For instance, the stiffness matrix of the lumped counterpart of the four-node 1D continuous interface element of Fig. 4.13b

can be elaborated to give

$$K = \frac{1}{2}bL \begin{bmatrix} k_n & 0 & -k_n & 0 & 0 & 0 & 0 & 0 \\ 0 & k_n & 0 & -k_n & 0 & 0 & 0 & 0 \\ -k_n & 0 & k_n & 0 & 0 & 0 & 0 & 0 \\ 0 & -k_n & 0 & k_n & 0 & 0 & 0 & 0 \\ 0 & 0 & 0 & 0 & k_t & 0 & -k_t & 0 \\ 0 & 0 & 0 & 0 & 0 & k_t & 0 & -k_t \\ 0 & 0 & 0 & 0 & -k_t & 0 & k_t & 0 \\ 0 & 0 & 0 & 0 & 0 & -k_t & 0 & k_t \end{bmatrix} \qquad (4.27)$$

The degrees of freedom have again been sequenced according to (4.11) with the node-numbering of Fig. 4.13b, and C has again been assumed to be given by (4.22). A comparison with the corresponding stiffness matrix (4.24) of the continuous counterpart shows that the number of zero off-diagonal terms increases even further owing to the absence of coupling between the individual node-sets in addition to the absence of mixed-mode coupling in C of (4.22).

4.3.3 A comparison

The performance of continuous versus lumped interface elements has been investigated for the notched beam of Fig. 4.14. The mesh is composed of four-node quadrilaterals and four-node interface elements (Fig. 4.13b) for the potential mode I discrete crack ahead of the notch. The comparison is focused on the linear solution, i.e. the solution whereby the interface elements are given a large dummy stiffness so as to represent the initial uncracked state. *The question is how large the dummy stiffness can and should be made.* The surrounding material was assumed to behave elastically with $E = 20000 \text{N/mm}^2$ and $v = 0.2$, such that the stiffness EA/l of the beam itself is of the order 10^{+2}N/mm^2. Hence, k_n was varied as 10^{+3}, 10^{+4} and 10^{+5} N/mm^3. The effect of k_t was suppressed by using dependence relations that prohibit mode II displacements.

Results are shown in Fig. 4.15 in terms of mode I traction profiles ahead of the notch. The results are compared to the rigid-connection solution which has been obtained by omitting the interface elements altogether.
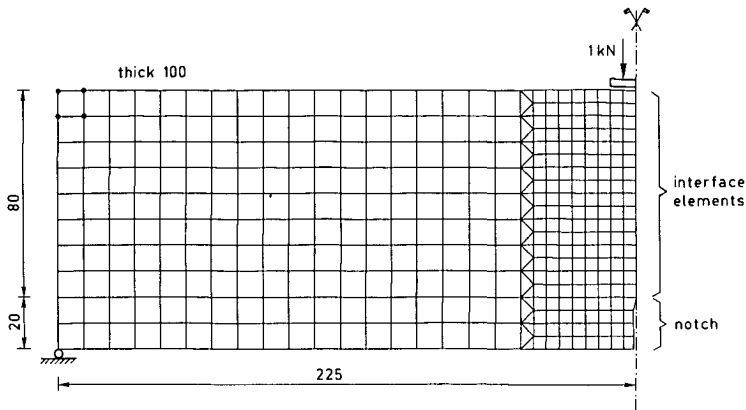
62

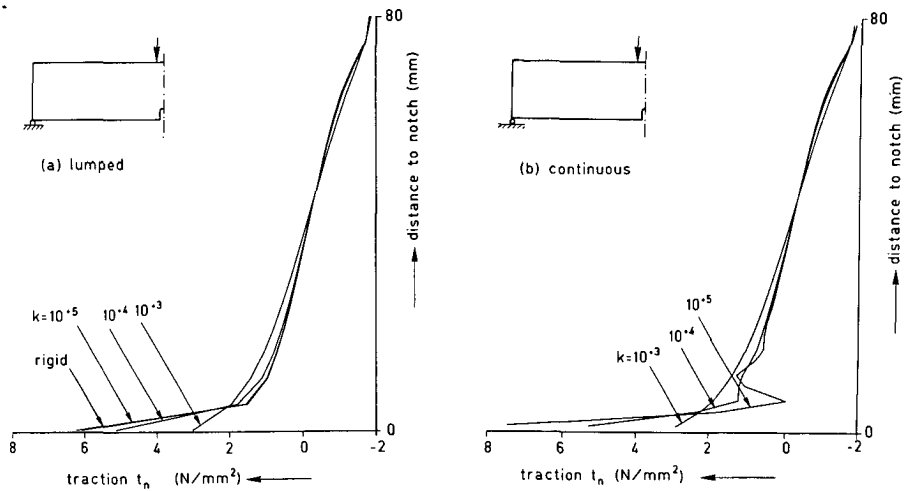Fig. 4.14. Mesh for linear interface analysis of notched beam (dimensions in mm).

Fig. 4.15. Traction profiles in front of the notch of the beam in Fig. 4.14.
(a) lumped interface elements; (b) continuous interface elements.

For the *lumped* interface elements, an increase of k_n shows the solution to smoothly converge towards the rigid-connection solution. For the highest value of $k_n=10^{+5}$ the deviation from the rigid connection solution is negligible. Hence, the object as to keeping the initial dummy separation negligible, while simultaneously capturing the high traction gradient ahead of the notch with accuracy, has been attained.

In contrast, the profiles obtained by use of *continuous* interface elements exhibit significant oscillation with increasing k_n. Here, it turns out that smooth and reliable

63

results can be obtained only for k_n-values less than 10^{+3}. However, the corresponding deviation from the rigid-connection solution, i.e. the initial dummy separation, is then unacceptable while the high traction gradient is not captured sufficiently accurately.

A similar trend has been found when applying the continuous interface elements to bond-slip problems, where moderate values of k_t (e.g. k_t=200N/mm^3) provided smooth bond shear traction-slip profiles, while high values (e.g. k_t=10^{+5}N/mm^3) induced oscillations at locations where the steel exits the concrete. In general, the maximum allowable k-value that prevents oscillations for continuous interface elements depends on the steepness of the traction gradient, on the element size and on the stiffness of the surrounding material. The quadratic version of the continuous interface element has been found to suffer from the same deficiency.

The oscillations for continuous interface elements are peculiar because similar elements have been previously reported to perform adequately or even excellently[Nils 82]. A review of previous applications reveals that the stiffness values adopted invariably fell into the lower range. For instance, in bond-slip applications the maximum value of k_t adopted was 1000[Scha 75], 2000[Dorr 80], 250[Mehl 85], or 200[deGr 81,Glem 84,Rots 85c] N/mm^3, in early rock mechanics applications[Good 68] k_n was mostly 47 N/mm^3, while in non-predefined discrete crack applications[Ingr 85a] the absolute value of k_n equals $f_{ct}^2/k\,2G_f$ which hardly ever exceeds 250 N/mm^3. Application of continuous interface elements to *predefined* discrete cracks does not seem to have been pursued before. Predefined discrete crack research has so far resorted to special-purpose techniques comparable to the use of lumped interface elements[Ngo 67,Nils 68,Hill 76,Carp 86,Gust 85,Lori 87]. On the other hand, in the field of contact problems continuous interface elements do have been used, namely as gap elements. Here, the underlying idea is to minimize overlap in compression which is essentially similar to minimizing initial separation in predefined cracks. In that field a bouncing behavior for large stiffness values has recently been reported[Simo 86].

The review calls for further clarification and it was decided to subject the element stiffness matrices to an eigenvalue analysis. Table 4.II summarizes the results for the four-node interface element of unit dimensions and unit stiffness, both in its continuous version and in its lumped version.

For both element versions a four-fold zero eigenvalue was found, the corresponding eigenmodes of which display Δu_n=0 and Δu_t=0 along the entire interface. These zero-energy modes correspond to the physical interpretation of interfaces. In an element assembly they cause no harm for they are suppressed by the surrounding continuum elements.

The *lumped* interface element furthermore has a four-fold eigenvalue equal to 1, the corresponding eigenmodes of which display non-uniform mode I separation, non-
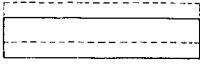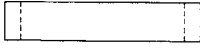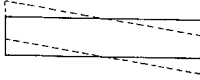
eigenmode	eigenvalue lumped	eigenvalue continuous	note
	0	0	zero-energy
	0	0	zero-energy
	0	0	zero-energy
	0	0	zero-energy
	1	1/3	non-uniform mode I
	1	1/3	non-uniform mode II
	1	1	uniform mode I
	1	1	uniform mode II
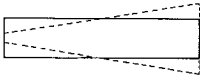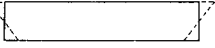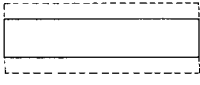
Table 4.II. Eigenvalue analysis for four-node lumped and continuous interface elements.

uniform mode-II sliding, uniform mode I separation and uniform mode-II sliding.

For the *continuous* interface element the subtle difference lies in the fact that the two eigenvalues corresponding to the non-uniform modes equal 1/3 instead of 1. This implies that non-uniform modes are triggered more easily for continuous elements than for lumped elements, which explains possible oscillation in traction profiles. The use of under- or over-integration did not resort any positive effect. Neither did the use of special tying schemes[deGr81] in an attempt to suppress the oscillations. The phenomenon requires further research.

It is concluded that in their present form, continuous interface elements should be employed with care. Problems that require large k-values should be approached with lumped interface elements. Note that these are not only contact problems and predefined discrete crack problems, but also bond-slip problems where power-law type[Noak78,Brug87] of traction-slip curves even produce infinite values of k_t.

65

5. UNCURVED MODE I FRACTURE

Having treated the crack concepts, constitutive models and the issues of finite element discretization, the present chapter marks the starting point for the scrutiny of structural fracture.

This chapter considers uncurved mode I fracture in plain concrete. This class of problems possesses a privileged position since the lines of the mesh can be adapted to the lines of the fracture, which eliminates stress rotation beyond fracture. As a consequence, the differences between fixed, multi-directional and rotating crack concepts, and even the difference between smeared and discrete concepts vanish.

Nevertheless, we will demonstrate that such cases are not obvious. Adopting the terminology of experimental research, we distinguish between cases of direct tension, whereby an attempt is made to stretch material samples homogeneously into the post-peak regime in order to create a well-defined separation band, and cases of indirect tension, whereby the separation is imposed indirectly via bending. The treatment is focused on the crucial issue whether the softening function may be regarded as a material property.

5.1 Direct tension[‡]

Direct tensile tests have been performed by Reinhardt, Cornelissen and Hordijk[Rein 86,Hord 87] on double-notched prisms 250 mm long, 60 mm wide and 50 mm thick (Fig. 5.1a). Using a closed-loop electro-hydraulic machine, they were able to record the complete softening response, as shown in Fig. 5.1b in terms of an averaged stress-deformation curve. The average stress is defined as the load divided by the net cross-sectional area ($50\times50\,mm^2$), while the deformation is the averaged result of ten extenso-meters, five at the front face and five at the back face of the specimen, as indicated by A to E in Fig. 5.1a. The gauge-length of the extenso-meters is 35 mm, which will serve as reference length throughout this section.

The diagram shows that the stress almost linearly increases with increasing deformation up to peak, whereafter a steep drop occurs which gradually evolves into a long tail. Although the load and the displacements in the softening regime could be controlled properly, there remains the curious observation of a pronounced 'bump' half way down the softening branch. Similar 'bumps' in softening curves have been reported amongst others by Willam et al.[Will 86] and Budnik[Budn 85].
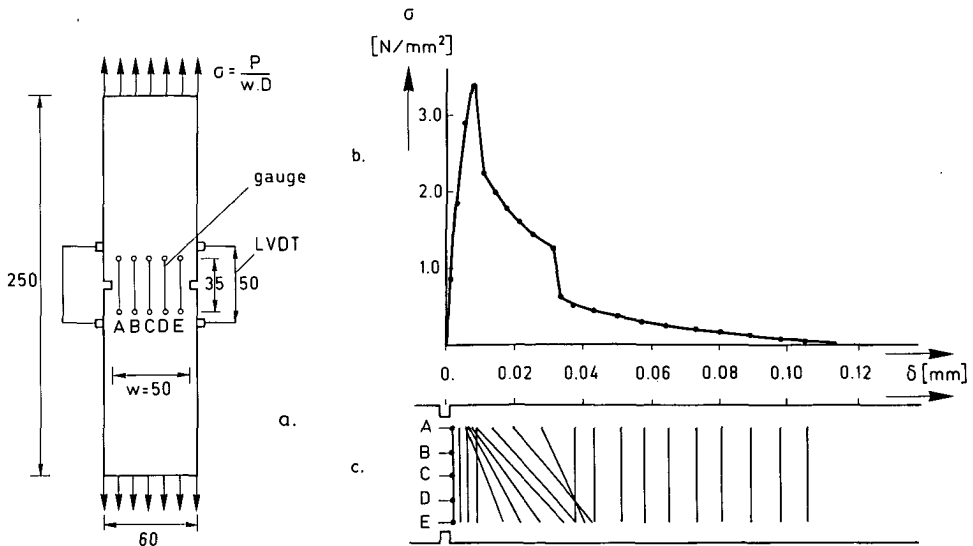

Fig. 5.1. Typical experimental result of direct tensile test[Rein 86,Hord 87].
(a) Specimen and instrumentation.
(b) Average stress-deformation curve over 35mm gauge-length.
(c) Distribution of deformations over the cross-section between the notches.

Another view of the experimental results is presented in Fig. 5.1c, where the separate readings of the extenso-meters A to E have been plotted for various stages of the deformation process. Prior to the peak stress the deformation distribution over the center-section appears to be symmetric, but immediately after passing the peak stress we observe non-symmetric deformations which reveal that the fracture tends to propagate from one side of the specimen to the other instead of propagating symmetrically. Non-symmetric tensile fracture modes have also been reported by Labuz et al.[Labu 85], although others claim to have observed symmetric modes, e.g., Gopalaratnam & Shah[Gopa 85].

The observation of a non-symmetric fracture mode is of utmost importance as it essentially suggests that the direct tensile test is not direct. This has also been recognized by van Mier[vanM 86] and Hordijk et al.[Hord 87], who advocated the idea that there might be an interrelation between the 'bump' and the non-symmetric localization. A sound explanation of these phenomena can be provided with aid of numerical simulations. Preliminary results were presented in 1987[Rots 87a].

Fig. 5.2 shows the computational set-up, which consists of four-node elements that were integrated using four-point Gaussian quadrature. An exception was made for the center elements between the notches, which were integrated using a reduced 2×1 point scheme$^{Rots\ 86}$. The lower boundary of the specimen was assumed to be fixed, while at the upper boundary a translational spring and a rotational spring were added in order to simulate the effect of the testing machine. The spring stiffnesses were specified as k_t=148000 N/mm and k_r=10^9 Nmm/rad. Dependence relations were added to ensure that the top of the specimen be kept straight. In this manner, the upper boundary could undergo a translation and a rotation but not a distortion.

In the experiment the load was applied at point G and was servo-controlled by a feed-back signal from two LVDT's mounted at the sides of the specimen (Fig. 5.1a). As a numerical analogy, the analysis was performed under 'indirect displacement control' (section 4.1), whereby the averaged crack opening displacement increment over the center elements (width 2.5mm) served as the control parameter. A full Newton-Raphson tangent stiffness scheme has been employed.

The elastic concrete properties were assumed to be: Young's modulus E=18000 N/mm^2 and Poisson's ratio ν=0.2, which corresponds to a lightweight concrete specimen$^{Rein\ 86}$. The softening parameters were taken as: tensile strength f_{ct}=3.4 N/mm^2 and fracture energy G_f=59.3 J/m^2, while the shape of the tensile softening diagram was assumed to be bilinear with the breakpoint located at $\varepsilon_{nn}^{cr}=\varepsilon_u/12$ and $t_n^{cr}=f_{ct}/3$. This diagram with its steep initial portion was adopted because it illustrates certain phenomena most clearly. The fracture was assumed to localize within the center band of elements with a width h=2.5 mm. The element in front of the right notch in Fig. 5.2 was given a material imperfection in the form of 1 percent reduction of G_f, the importance of which is explained afterwards.

-fracture localization-
Figs. 5.3 to 5.7 present key-events in the fracture localization process. Upon incrementing the load, the analysis started to predict symmetric deformations, as shown in Fig. 5.3 which gives the incremental deformations at an average stress σ=2.837 N/mm^2 (average stress as defined before). During the entire pre-peak regime of the load-displacement response the specimen appeared to be strained symmetrically, with both notches being active. A limit point was encountered at σ=2.856 N/mm^2 and the tangent stiffness matrix ceased to be positive definite. Indeed, a negative eigenvalue was calculated for the tangent stiffness matrix. Fig. 5.4 shows the corresponding eigenmode, which is identical to the incremental deformation field at the peak-load. It resembles strongly non-homogeneous and non-symmetric deformations. Obviously, the right notch with the small material imperfection suddenly becomes very active while the opposite side of the specimen unloads.
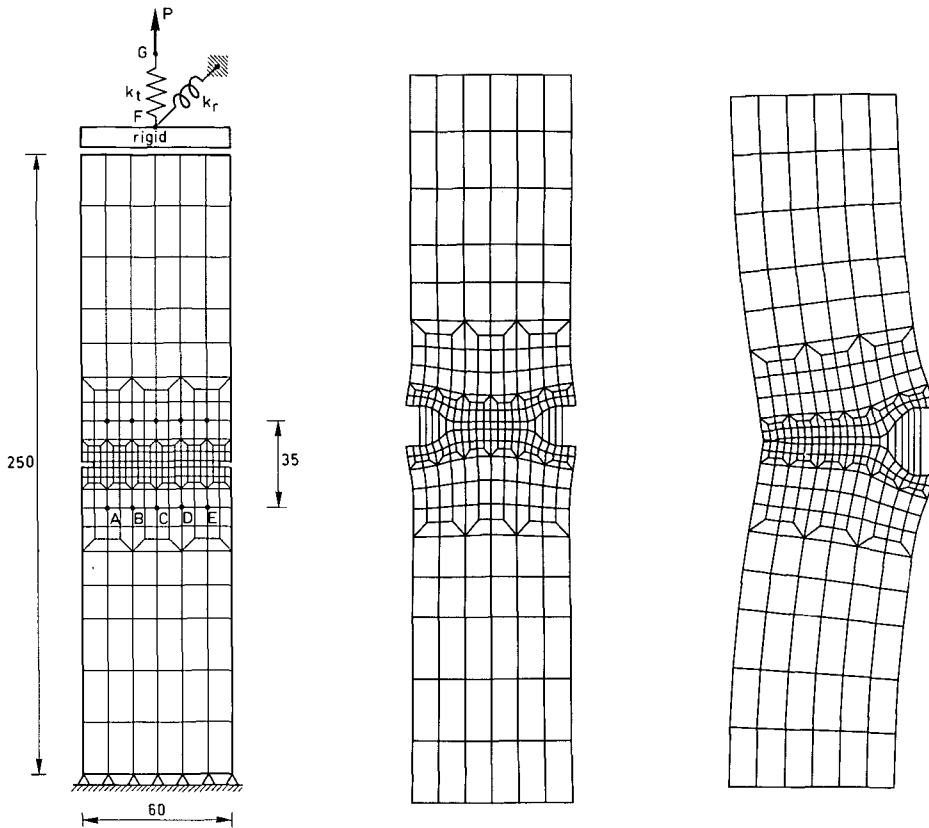
left: Fig. 5.2. Computational set-up for direct tensile test of Fig. 5.1.

center: Fig. 5.3. Incremental deformations, pre-peak, $\sigma=2.837 \text{N/mm}^2$.

right: Fig. 5.4. Incremental deformations, at-peak, $\sigma=2.856 \text{N/mm}^2$.

After locating the limit point, the load was decremented and a genuine equilibrium path could be obtained. The fracture propagates towards the opposite notch, as shown in Fig. 5.5 which gives the incremental deformations at a residual stress $\sigma=1.865 \text{ N/mm}^2$. Upon further decreasing the load the left notch became active again, while the right notch tended to unload temporarily (Fig. 5.6). Subsequently, the load had to be incremented again slightly to re-load the right notch and to stretch the specimen uniformly. This operation was successful and finally, all elements between the notches displayed softening so that the load could come down to zero under subsequent homogeneous deformation (Fig. 5.7).

The subsequent stages of incrementation and decrementation of the load can be recognized from Fig. 5.8, which gives the averaged stress-deformation curve (over the 35 mm gauge length). The figure compares the non-symmetric solution with the solution that is obtained by considering only a symmetric half of the specimen, thereby

69
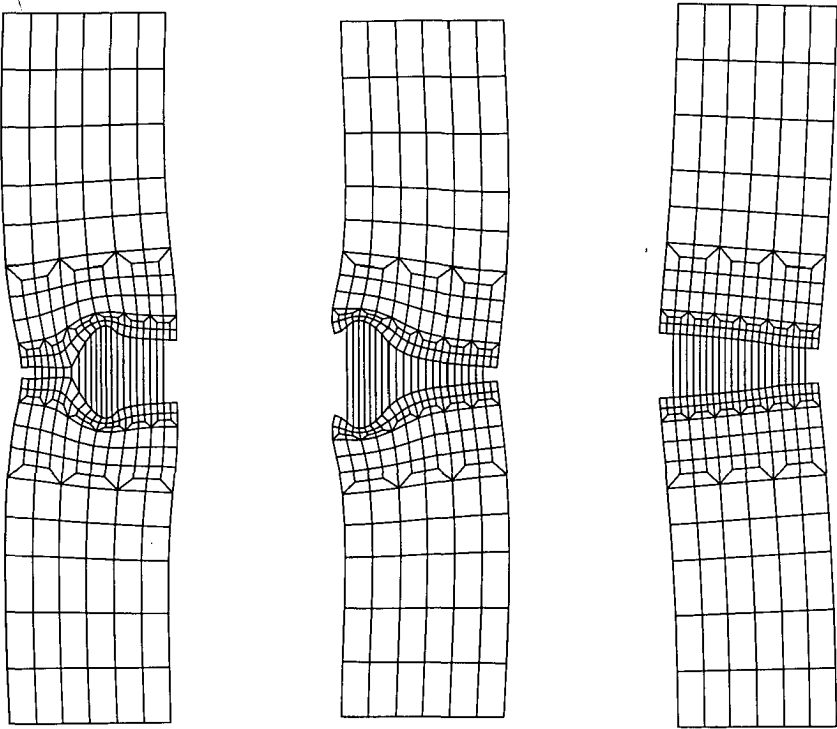
left: Fig. 5.5. Incremental deformations, post-peak, $\sigma=1.865 \text{N/mm}^2$.
center: Fig. 5.6. Incremental deformations, post-peak, $\sigma=1.101 \text{N/mm}^2$.
right: Fig. 5.7. Incremental deformations, post-peak, $\sigma=1.026 \text{N/mm}^2$.

enforcing symmetric crack propagation. It appears that non-symmetric deformations reduce the limit load and, even more interesting, have a strong impact on the post-peak part of the curve. While the symmetric solution describes a descending branch that reasonably resembles the bilinear input diagram, the non-symmetric solution exhibits a steeper drop after the peak stress and a significant bump. The agreement with the experimental measurements of Fig. 5.1b is evident and it proves that the bump is a direct consequence of the non-symmetric fracture mode.

-role of imperfection-
    The curve which is labeled as "non-symmetric" in Fig. 5.8 was obtained for the full specimen including a material imperfection. The curve which is labeled as "symmetric" in Fig. 5.8 was obtained for a symmetric half of the specimen without the imperfection. It is illustrative to discuss a third analysis involving the full specimen without the imperfection.
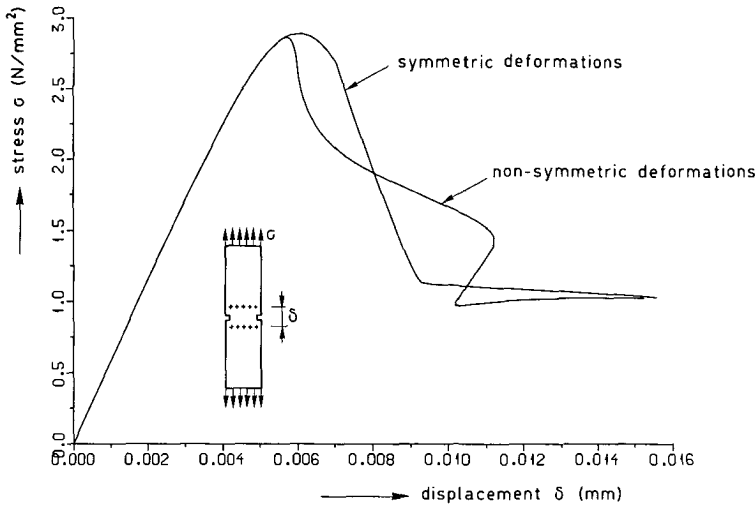
70

Fig. 5.8. Average stress versus average deformation for direct tensile test.

With this analysis the specimen continued to deform symmetrically in the soften-
ing regime. The softening curve was identical to the curve for the analysis on the sym-
metric half of the specimen. Yet, when analyzing the full specimen, uniqueness of the
solution is lost before the peak stress is attained. A negative eigenvalue was extracted
at $\sigma=2.866 \text{N/mm}^2$, with the corresponding eigenmode displaying non-symmetric
deformations. This so-called bifurcation point marks the beginning of an alternative
equilibrium path that involves non-symmetric deformations. Access to this path can
be enforced by adding a part of the eigenvector to the incremental displacement
vector[deBo 86,deBo 87a]. In the present calculation this possibility has not been pursued,
and further incrementation of the load resulted in continued symmetric deformations.
A second negative eigenvalue of the tangent stiffness matrix was encountered at
$\sigma=2.887 \text{N/mm}^2$. Beyond this stage, further incrementation of the load appeared to be
not possible and, consequently, the second negative eigenvalue is related to a limit
point. When only a symmetric half of the specimen is analyzed, the bifurcation point
of course vanishes and the analysis renders the limit point.

From the three analyses we conclude that the direct tension test involves a bifurca-
tion problem that can be transferred to a limit problem either via a material imperfec-
tion or via omitting a half of the specimen. The former method triggers the non-
symmetric mode and the latter the symmetric mode. Interesting parallels exist with
soil plasticity studies of shear band bifurcation[deBo 88a].

71

-consequence of non-symmetric deformations-

In the real world, imperfections always exist and for heterogeneous materials like concrete they will definitely exceed the 1 percent reduction of G_f which we employed here. Consequently, it is unimaginable that crack propagation will ever be symmetric in the direct tension test. An exception are perhaps very short specimens, where the role of the boundary conditions is so dominant that they prevent non-symmetric crack propagation. For non-short specimens the load-displacement response will always continue on the steepest post-peak curve with non-symmetric deformations.

We must conclude that a 'direct' tensile test on a heterogeneous material is generally not as direct as the name suggests. A consequence is that the softening curve measured from such tests does not represent true material behavior, but it represents a combination of material behavior, described by the elastic-softening parameters for the equivalent homogenized continuum, and structural behavior due to non-homogeneous deformations for the particular geometry and the particular set of boundary conditions. A quantification of this disturbance by the geometry (e.g. specimen length) and the boundary conditions (spring stiffnesses) has recently been given[Rots 88]. Experimentally, the phenomena have been investigated by Hordijk et al.[Hord 87].

-justification of softening models-

The role of structural effects in the descending branch has been recognized before and has culminated into pessimism against softening models[Kots 83,vanM 84,Read 84]. The present results do not support this pessimism. In contrast, they reveal that a proper elastic-softening material law is able to *predict* non-homogeneous deformations and associated structural phenomena. To that end, the introduction of a true, 'unnotched tensile strength' that exceeds the 'notched tensile strength', as well as the inclusion of a concave softening diagram with a steep drop just after peak are essential.

To demonstrate the need for the latter, the imperfect specimen was re-analyzed using a linear and a nonlinear[Rein 86] softening diagram (Fig. 3.1) instead of the bilinear diagram, the initial tangent softening moduli of which compare to each other as 1 : 2.71 : 3.33 respectively. Fig. 5.9 shows the impact on the global softening response. For the bilinear diagram, i.e. the diagram with the steepest slope, the deviation between local and global softening turns out to be most significant. For the nonlinear diagram the bump becomes less pronounced and for the linear diagram it even disappears. Obviously, the deviation between local and global softening and the associated non-symmetry decrease with decreasing softening modulus. For linear softening the output softening curve is perfectly smooth and, apart from the effect of the notches which rounds-off the peak and reduces the input 'unnotched' tensile strength to the 'notched' tensile strength, this curve replicates the input softening curve, which indicates that the fracture remains perfectly symmetric.
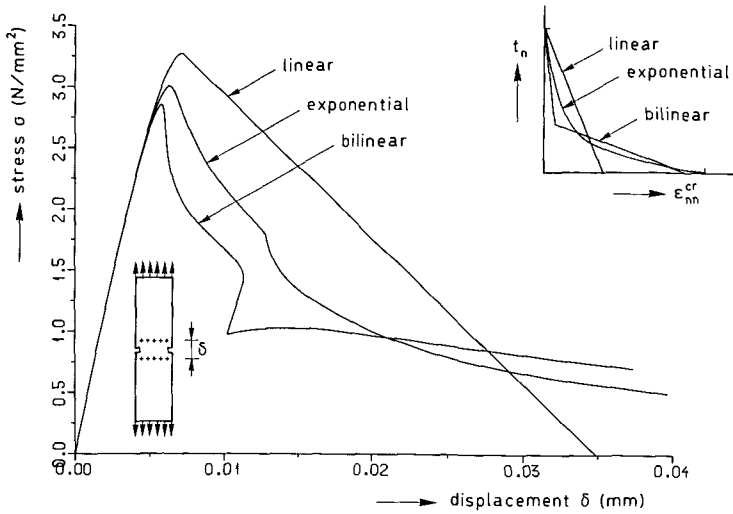
Fig. 5.9. Effect of local softening diagram on global softening response
in terms of average stress versus average displacement.

In none of the tests[Rein 86,Hord 87] symmetric deformations were observed, and it is concluded that the use of a linear softening diagram is incorrect. On the other hand, the bilinear diagram perhaps exaggerates the phenomenon, while the nonlinear diagram produces an intermediate result that most closely matches experimental data. The present results neither support the need for a reduction of G_f as suggested by van Mier[vanM 86], nor the need for a revival of the brittle stress-drop as suggested by Kotsovos[Kots 83].

Yet, some caution must be exercised in drawing quantitative conclusions, since the analyses were performed under the assumption of plane-stress, while in the experiment three-dimensional effects play a role with the crack front not only advancing from the left to the right, but also from the front to the back (or vice-versa)[Hord 87]. Hence, the experimental surface measurements differ from the plane-stress averaged computational results. Basically, this averaging process of non-homogeneous deformations over the cross-section introduces a further source of 'structural behavior' into the softening curve for plane-stress analysis.

-snap-back behavior-

A curiosity of the non-symmetric softening path in Fig. 5.8 (for the bilinear input diagram) is that while the left notch is re-activated, not only the load but also the displacement decreases. This snap-back behavior[Carp 86,Cris 86,deBo 86] or catastrophic softening[Dems 85,Roku 86] can be illustrated even better if we plot the stress-deformation over a gauge-length which is *longer* than the 35mm which furnished Fig. 5.8. To this

73

end, the averaged stress has been plotted against the total elongation of the specimen in Fig. 5.10, so that the reference length is now equal to 250 mm.
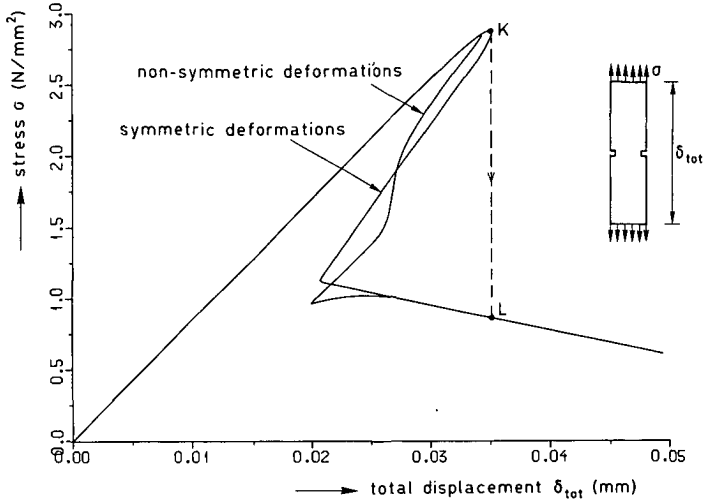

Fig. 5.10. Average stress versus total elongation for direct tensile test.
(bilinear softening; the curves correspond to those of Fig. 5.8)

Fig. 5.10 exhibits a pronounced snap-back after peak, which explains why indirect displacement control is required to stabilize the solution beyond peak load[deBo 86,deBo 87]. If the analysis had been carried out under direct displacement control at the top of the specimen, the quasi-static solution would have had to jump from K to L in Fig. 5.10, leaving the 'bump' undetected.

The results parallel the experimental findings from closed-loop tensile testing, where the importance of a proper feed-back signal over a short gauge-length encompassing the separation band has been emphasized[Gopa 85,Labu 85]. If the signal does not meet this requirement it monitors unloading outside the separation band rather than softening inside the separation band, which generates explosive response. Depending on the precise elastic-softening properties of the material even a gauge-length of 35 mm may not be small enough to avoid snap-back phenomena (Fig. 5.10 for bilinear softening). For the present calculations, the average displacement over a length of 2.5mm served adequately since it increased monotonically in time. A safe alternative is to control the analysis via the opening displacement of the currently-active notch rather than the average displacement over both notches.

5.2 Indirect tension

To gain further insight into the practical significance of the various softening parameters, reference is made to a bending problem of indirect tension in a notched beam. Such cases are representative for structural practice and less complicated than the research problem of 'direct' tension. The dimensions correspond to a specimen tested by Kormeling & Reinhardt[Korm 83] (Fig. 5.11a). The mesh was composed of four-node elements with 2×2 Gaussian integration. The center elements ahead of the notch were integrated using a reduced 2×1 point scheme in order to propagate a well-defined mode I smeared crack. Both the load F and the weight of the beam have been included.

The elastic parameters have been assumed as: E=20000N/mm^2 and ν=0.2. The analyses have been focused on a variation of the softening parameters, whereby the reference set was fixed as f_{ct}=2.4N/mm^2, G_f=113J/m^2 and the nonlinear (exponential) softening function (Fig. 3.1). When varying one of these parameters, the others were kept unaltered. We disturbed f_{ct} by -40% and +40%, G_f by -40% and +40%, while the exponential softening function was incidentally replaced by a power function[Rein 84] and by the linear function.

The effect is depicted numerically in Table 5.I in terms of maximum load data and sensitivity numbers, and graphically in Fig. 5.11 in terms of load-deflection response.

tensile strength [N/mm^2]	fracture energy [J/m^2]	softening function	maximum load [N]	notes
2.40	113	exponential	1370	reference set
3.36	113	exponential	1658	$S(f_{ct})$=0.53
1.44	113	exponential	973	$S(f_{ct})$=0.72
2.40	**158**	exponential	1464	$S(G_f)$=0.17
2.40	**68**	exponential	1220	$S(G_f)$=0.27
2.40	113	**linear**	1608	
2.40	113	**power law**	1154	

-S(α) is the change in percent in maximum load if α is changed by 1 percent[Hill 85b].
-exponential softening function according to Reinhardt et al.[Rein 86]
-power law according to Reinhardt[Rein 84]

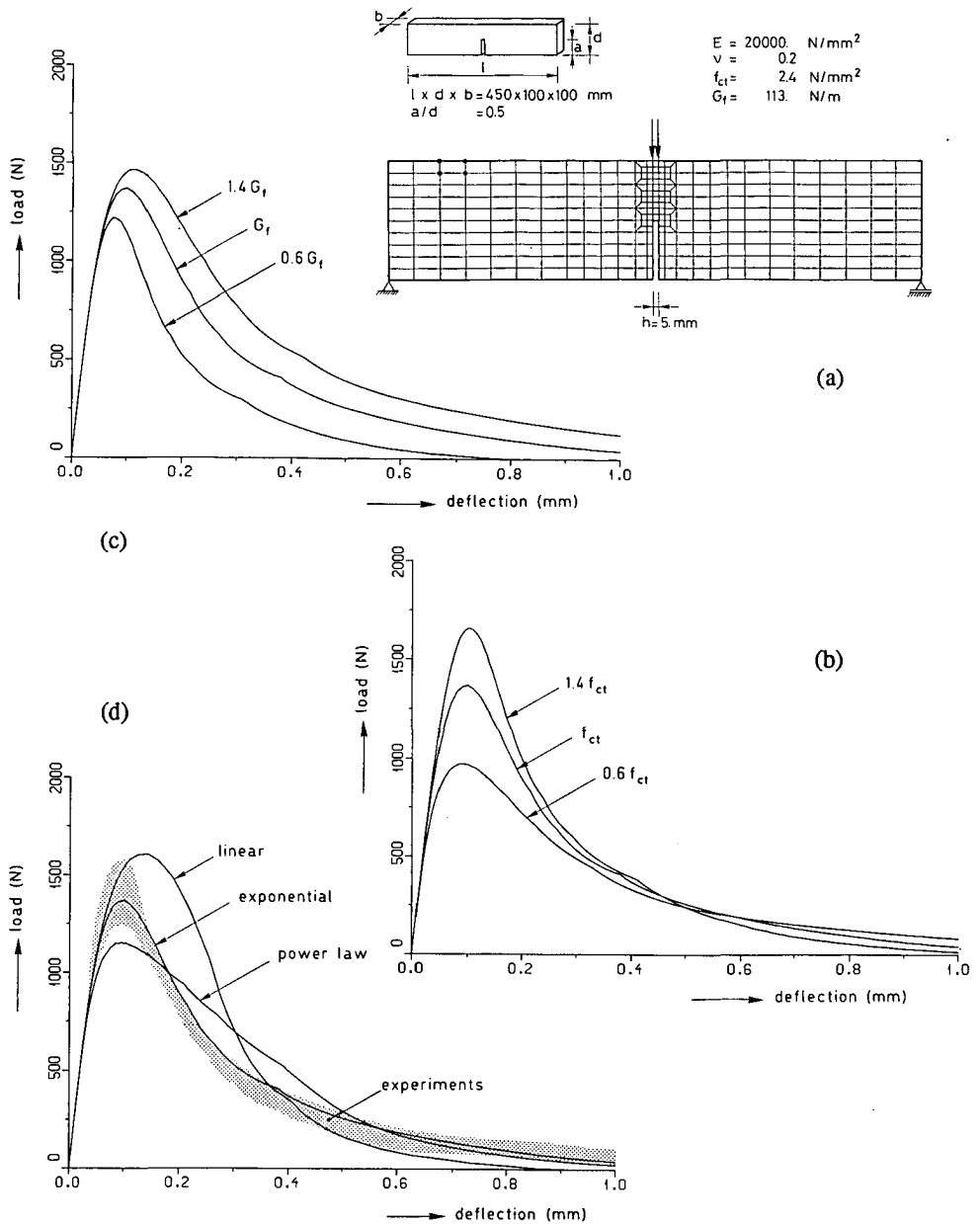Table 5.I. Maximum load data corresponding to sensitivity study of notched beam in Fig. 5.11.

Fig. 5.11. Sensitivity study of indirect tension fracture in a notched beam[Korm 83].

    (a) Finite element idealization.

    (b) Effect of tensile strength f_{ct} on load-deflection response.

    (c) Effect of fracture energy G_f on load-deflection response.

    (d) Effect of shape of softening diagram on load-deflection response.

Considering the maximum load data first, we observe that the role of the strength parameter f_{ct} overshadows the role of the energy parameter G_f. An increase of f_{ct} by 40 percent causes the maximum load to increase by 21 percent, while a similar increase of G_f causes the maximum load to increase by only 7 percent. Obviously, the sensitivity of the present beam with respect to f_{ct} is three times as large as it is with respect to G_f, which supports the assertion that the uncertainties involved in G_f are not dramatic. In contrast, the effect of the shape of the softening diagram is surprising. For instance, a replacement of the exponential function by the linear function affects the maximum load by 17 percent, which is of the same order of magnitude as the effect of the 40 percent increase of tensile strength.

Considering the post-peak response, we observe that the beam behaves less ductile, i.e. more brittle, if the tensile strength increases (Fig. 5.11b). Again, the value of the fracture energy is less essential (Fig. 5.11c), but the shape of the softening diagram is (Fig. 5.11d). In contrast to the results in the preceding section for 'direct' tension, the present results do not detect a correlation between the local softening diagram adopted and the global softening curve predicted, since the steeper the initial softening modulus is assumed, the flatter the global softening curve becomes. Fig. 5.11d is also of interest in that it demonstrates the exponential softening function (Fig. 3.1) to produce a concave-shaped response that nicely falls within the experimental scatter.

A major conclusion is that quantitative predictions of concrete fracture are contingent upon the subtle interaction between different softening parameters, neither of which may be ignored. In this light, the results cast doubt on the integrity of fitting maximum load data by use of linear softening diagrams[Baza 83a]. The search for a unique set of softening parameters should include the entire concave-shaped response in addition to the maximum load.

Considering that one should not pursue oversophistication for heterogeneous materials because of their inherent scatter in properties and because of the 'structural phenomena' involved in softening, it is tentatively concluded that the exponential softening function proposed by Reinhardt et al.[Rein 86] with a tensile strength in the range between 2.5–3.5N/mm^2 and a fracture energy in the range between 50–150J/m^2 serves as a fair set of mode I parameters for standard concrete qualities. This suggestion is supported by the curve-fit for the present beam and other beams[Rots 86], as well as by the results in the preceding section for 'direct' tension. Chapter 6 will provide additional justification for cases of uncurved fracture.

It is noted that for large-size structures the quantification of the softening parameters is less essential than for the laboratory-size specimens considered here. This is because the solution approaches the solution of linear-elastic fracture mechanics

which is dominated by the crack tip singularity. For large-size structures the error introduced by the use of e.g. a linear softening diagram instead of a concave diagram remains only small.

The key-interpretation of the elastic-softening theory is that the sensitivity to fracture is a matter of the available elastic strain energy accumulated in the system versus the fracture energy required to separate it into two pieces (G_f times the separation area generated). Consequently, in addition to the softening parameters also the value of Young's modulus is essential. The energy balance, which is reflected also in the condition of snap-back instability (3.9), explains the size-effect, i.e. the dangerous increase of brittleness with increase of structural dimensions. The underlying idea is that an increase of structural dimensions generally implies the strain energy to increase disproportionally compared to the increase of the separation area generated, so that the behavior becomes more brittle and often even involves snap-back. For particular geometries and particular assumptions regarding the softening parameters this knowledge has been transfered into 'size-effects' and 'brittleness numbers'[Hill 76, Baza 83a, Carp 86].

5.3 Conclusions

A discussion has been given of uncurved mode I tensile fracture. A new numerical approach towards the research problem of 'direct' tension has been presented, which provides the key to the fundamental issue of 'material behavior' versus 'structural behavior' in tensile strain-softening. The post-peak response in the direct tensile test involves strongly non-symmetric deformations which affect the softening curve. Yet, this disturbance should not tempt one to conclude that softening type material models should be abandoned. Instead, the results provide a positive justification of the use of such models since these are able to predict the non-symmetry and associated structural phenomena.

Quantitative investigations for indirect tension suggest a tensile strength f_{ct} in the range between 2.5–3.5N/mm^2, a fracture energy in the range between 50–150J/m^2 and a concave-shaped softening diagram[Rein 86] to be a proper set of parameters. Most examples in this thesis will follow this recommendation. The sensitivity of failure loads with respect to G_f is inferior to the sensitivity with respect to f_{ct} and the assumed shape of the softening diagram.

78

6. CURVED MODE I FRACTURE AND STRESS ROTATION

With uncurved fracture it is natural to align the lines of the mesh with the lines of the fracture. In general this is impossible as the final crack path will be not only curved, but also unknown a priori. It is here that smeared concepts have been claimed to be superior for they do not impose restrictions on the crack orientation. However, the associated zig-zag propagation through the regular mesh involves a complication as the issue of stress rotation beyond cracking enters.

It is recalled from the single-element problem of section 3.4 that the various smeared concepts then show large discrepancies, ranging from very stiff behavior for the fixed single crack concept to very flexible behavior for the coaxial rotating crack concept. The purpose of this chapter is to proceed with this investigation on structural level.

On purpose we do not utilize the terminology *mixed-mode fracture* since there is no consensus on the question whether such a phenomenon exists for heterogeneous materials. Interpretations of the few relevant experiments reveal that curved fractures are predominantly of the mode I type[Arre 82,Koba 84,Ing 85,Jenq 88,Rots 87e]. Contrary results have been reported only for dynamic loadings[Harm 82] and for very particular static loadings with either an extremely high mode II[Baza 86a] or mode III[Baza 88] intensity. These three cases are beyond the scope of the present study which considers separation for static loadings. Any terminology of mode II or mixed mode in this chapter therefore relates solely to the local integration point level.

6.1 CLWL-DCB specimen

Section 4.2 introduced a CLWL-DCB specimen. In that treatment the constitutive formulation was kept constant in the form of the coaxial, rotating smeared crack concept, while the effect of the finite element lay-out was investigated. Here, we will keep the finite element lay-out constant as we will only use the mesh of Fig. 4.1 with four-node quadrilaterals, and investigate the effect of constitutive formulations. Although the loading consists of a wedge load and a diagonal compression load, the crack tip is in a state of tension-tension and propagates primarily in mode I.

Stress rotations relate to the interaction between the crack shear formulation and the control of crack orientation. Following the model problem of section 3.4, the investigation has been focused on the shear retention function β and the threshold angle α. First, α was kept constant at 60°, which is that high that any memory transfer between multi-directional cracks has been omitted, while β was varied:

— fixed cracks, $\alpha=60°$, $\beta\approx0$ (in fact 0.001 to avoid numerical problems)
— fixed cracks, $\alpha=60°$, $\beta=0.05$
— fixed cracks, $\alpha=60°$, variable β according to (3.8) with $p=2$

Fig. 6.1 presents the load-CMOD responses and compares them with the two results that have been presented before in section 4.2:

— coaxial rotating cracks, i.e. $\alpha=0$, β enforcing coaxiality according to (3.19)
— predefined discrete crack, zero shear stiffness and zero shear tractions.

A curve-fitting of the experimental result[Koba 85] has not been undertaken, although this is no doubt possible by optimizing the mode I parameters. We will concentrate on an objective match between the smeared crack results and the discrete crack result, and keep the mode I parameters the same as in section 4.2.
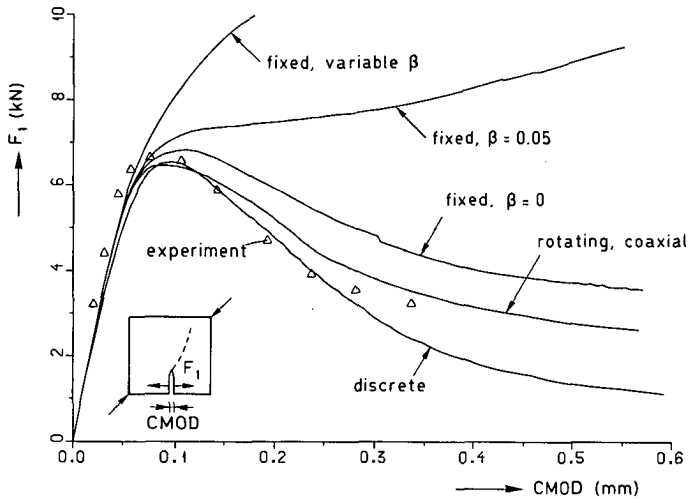

Fig. 6.1. Load-CMOD response of CLWL-DCB specimen for different crack models. The results were obtained for the mesh of Fig. 4.1 of four-node quadrilaterals.

Fig. 6.1 shows that all smeared crack results are too stiff. Only the rotating smeared cracks and the fixed smeared cracks with $\beta\approx0$ appear capable of producing a limit point with subsequent softening. Fixed cracks with significant shear retention fail in this respect. The latter statement already holds for a β value of 0.05, which is low compared to what is commonly used in engineering practice. The result for $\beta=0.05$ shows that the limit point has vanished while the response continues to shelve instead of to soften. For the variable shear retention factor that decreases with increasing crack strain, or any other high shear retention factor, the prediction becomes even worse as we observe the response to ascend steeply, even beyond a wedge load of 10kN.

The fact that fixed cracks perform adequately only in conjunction with a zero or almost zero shear retention factor is surprising, yet explainable. Such a model in which crack shear tractions remain zero or almost-zero, implies the axes of principal stress to be fixed or practically fixed after crack formation. Stress rotation is then caused by the surrounding elastic elements, while any rebuild of principal tensile stress in the cracked elements is constrained to occur parallel to the first crack. Non-zero shear retention factors provide an additional possibility of rebuilding principal tensile stress in the cracked elements, namely via rotation in an inclined direction. *Whenever such an additional opportunity of stress rebuild is given, it is eagerly utilized.* Along with the spurious stiffening from stress locking due to displacement compatibility (section 4.2), this explains the overstiff responses. This provides a straightforward extension of the conclusion from the model problem in section 3.4.

Fig. 6.2 illustrates the fracture localization for $\beta \approx 0$. It indicates that diagonal stretch bands through regular meshes can be predicted, at the expense of a number of spurious cracks. The pattern reveals a large number of orthogonal cracks, which confirms the rebuild of principal tensile stress parallel to the first crack. The experimental direction of fracture propagation (Fig. 4.1) is captured surprisingly well, and even better than by using the coaxial rotating crack concept (Fig. 4.3). This suggests that the fixed crack concept suffers less from directional bias than the coaxial rotating crack concept. Wen cracks are allowed to rotate, they apparently prefer to follow the lines of the mesh.
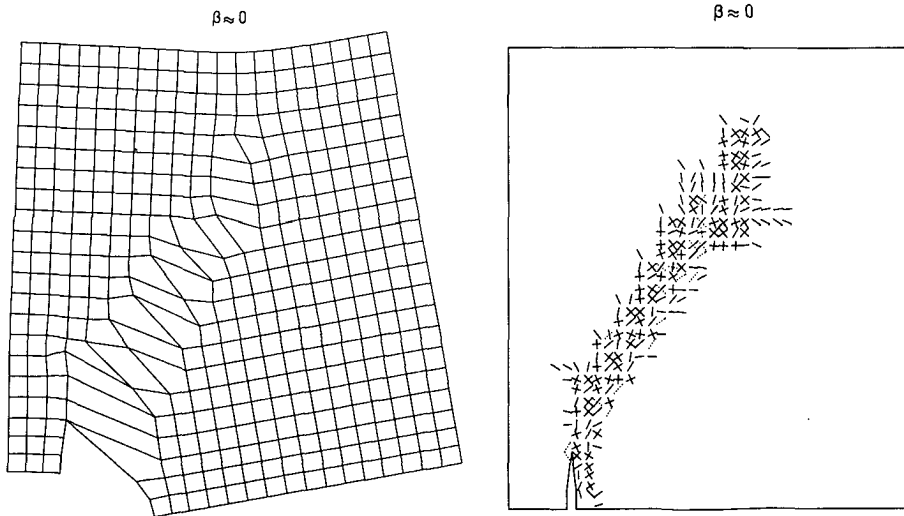

Fig. 6.2. Fracture localization in CLWL-DCB specimen for fixed smeared cracks with $\beta \approx 0$. Compare to Fig. 4.3 (rotating cracks).

For the present problem, fixed cracks with β≈0 provide less softening than rotating cracks. This is not related to any fundamental argument, but is due to the fact that the fixed-crack solution involves more "zig-zag jumps". The spurious stiffening from locked-in stresses is then emphasized. The plot of the principal tensile stresses (Fig. 6.3a) displays much more noise than the corresponding plot for rotating cracks (Fig. 4.11). Fig. 6.3b shows the principal tensile stresses for fixed cracks with β=0.05. We observe that these stresses entirely refuse to decrease, which strengthens the explanation of overstiff response. For even higher values of β or the variable β, very severe stress-locking occurred.
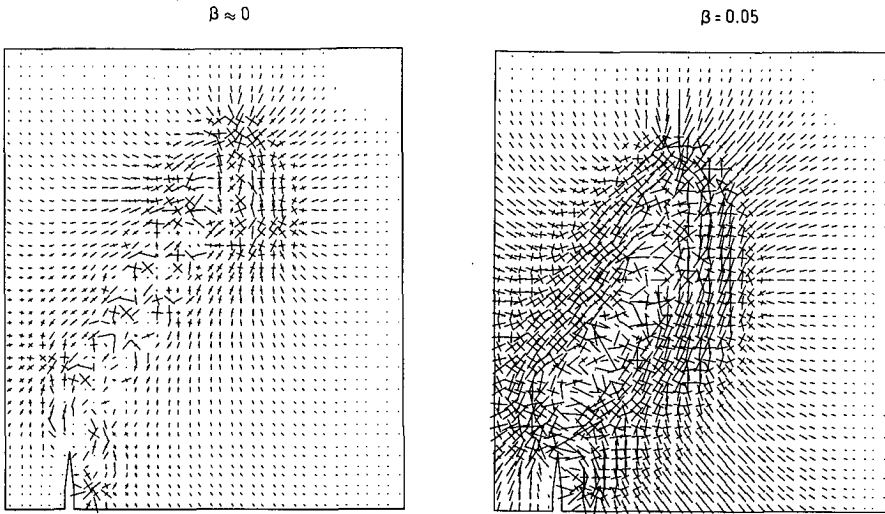

$\beta \approx 0$ $\beta = 0.05$

Fig. 6.3. Principal tensile stress trajectories for fixed smeared cracks.
(a) some stress locking for β≈0; (b) significant stress locking for β=0.05.
Compare to Fig. 4.11 (rotating cracks and discrete crack).

The high stresses, in turn, give rise to additional cracking. For β=0.05 this tendency is not yet dramatic (Fig. 6.4a), but for the variable β the final crack pattern bears similarities with a blot rather than with a sharp localization (Fig. 6.4b). Similar results were reported by e.g. van Mier[vanM 87], who employed β=0.2. It is emphasized that all\solutions depicted involve truly converged equilibrium states, i.e. the curious stress and crack patterns did *not* result from numerical inaccuracies or failure of the iterative procedure.

Having discussed the two extremes of fixed (single) cracks and coaxial rotating cracks, the next step is to investigate the intermediate option of fixed multi-directional cracks with transfer of damage memory and non-coaxiality between principal stress
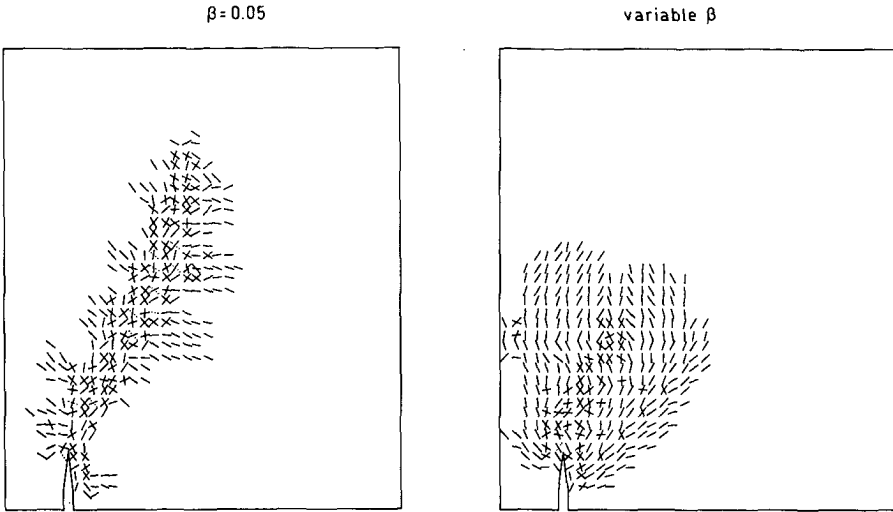
82

Fig. 6.4. Crack patterns at final stage for fixed smeared cracks.
(a) some diffusion for β=0.05; (b) significant diffusion for variable β of (3.8).
Compare to Fig. 4.3 (rotating cracks) and Fig. 6.2 (fixed cracks, β≈0).

and strain, as introduced in sections 3.2 and 3.4. To this end, the threshold angle α has been decreased from 60° to 10° (stepwise rotation) and 0° (continuous rotation). These analyses were undertaken both for β=0.05 and for the variable β of (3.18):

— stepwisely rotating cracks, non-coaxial, α=10, β=0.05 or variable β of (3.18)
— continuously rotating cracks, non-coaxial, α=0, β=0.05 or variable β of (3.18)

These combinations were not successful because the crack rotation insufficiently compensated for the above mentioned disease. The stresses again tended to remain too large. Here, the conclusion departs from the conclusion of the model problem in section 3.4, where a soft response was correctly achieved with these models.

It was experienced that crack rotation in a state of non-coaxiality between principal stress and strain magnifies problems with spurious unloading/reloading. The reason lies in the fact that initiation, closing and re-opening criteria are defined in terms of stress, while the localization is a matter of strain. The resulting state changes hamper convergence and introduce a too high degree of sophistication.

Our impression is that the power of non-coaxial, rotating crack models must be sought in the field of distributed fracture of reinforced concrete, where local unloading/reloading plays only a minor role compared to problems of localized fracture. With applications to distributed fracture also the physical basis for these models is more firm, since both stepwise rotation as well as non-coaxiality have been observed[Vecc 86,Bhid 87,Koll 87].

83

6.2 Single-notched shear beam

To investigate the generality of the statements in the preceding section, a different problem of tension-compression has been investigated. It concerns the single-notched shear beam tested by Arrea & Ingraffea[Arre 82] which failed in curved mode I fracture. Readers who are familiar with the subject may feel surprised since the beam has already been scrutinized[Glem 84,Ingr 85a ,Olde 85,Rots 85a ,deBo 86,deBo 87,Rots 87e]. However, none of the smeared crack solutions presented so far has been able to predict genuine separation and softening down to zero. In the context of the present chapter, this calls for a renewed investigation.

The mesh is shown in Fig. 6.5 and consists of three-node triangles in cross-diagonal pattern. The steel beam ACB has not been included in the mesh. Instead, the loading has been applied at the points A and B, while controlling the notch tip opening-displacement (section 4.1) in order to capture the snap-back involved[deBo 86,deBo 87]. The parameters were taken as: $E=24800\text{N/mm}^2$, $v=0.18$, $f_{ct}=2.8\text{N/mm}^2$, $G_f=100\text{N/mm}^2$, nonlinear softening (Fig. 3.1), $h=12\text{mm}$ (Table 4.I).
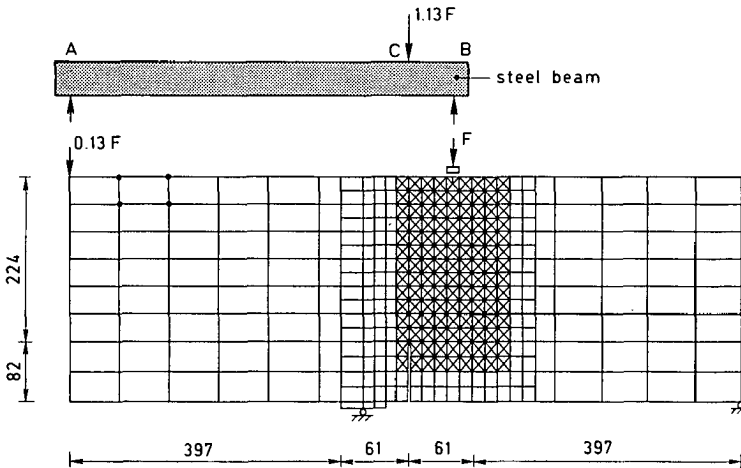
Fig. 6.5. Element mesh for smeared crack analysis of single-notched shear beam[Arre 82].

Five solutions are presented, corresponding to those of the CLWL-DCB specimen:

— fixed cracks, $\alpha=60^o$, $\beta\approx0$ (in fact 0.001 to avoid numerical problems)
— fixed cracks, $\alpha=60^o$, $\beta=0.05$
— fixed cracks, $\alpha=60^o$, variable β according to (3.8) with $p=2$
— coaxial rotating cracks, i.e. $\alpha=0$, β enforcing coaxiality according to (3.19)
— predefined discrete crack, zero shear stiffness and zero shear tractions.
Its location was adapted to the prediction by coaxial rotating cracks.

The (truly converged) solutions are summarized in Fig. 6.6, giving the load F versus the Crack Mouth Sliding Displacement, and Fig. 6.7, giving the load F versus the displacement of the master loading point C (which is recalculated from the displacements of the minor loading points A and B on the assumption that the steel beam is infinitely stiff). The curves have been terminated at the stage where convergence could no longer be achieved because of either spurious kinematic modes, or spurious state changes at places of locked-in stresses. The results for non-coaxial rotating (either stepwisely or continuously) cracks have been omitted because they were not successful for the reasons described in the preceding section.
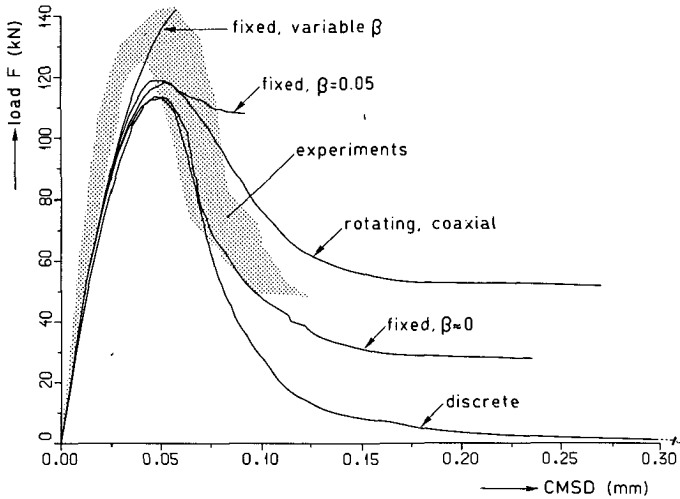

Fig. 6.6. Load F versus CMSD of single-notched shear beam of Fig. 6.5.
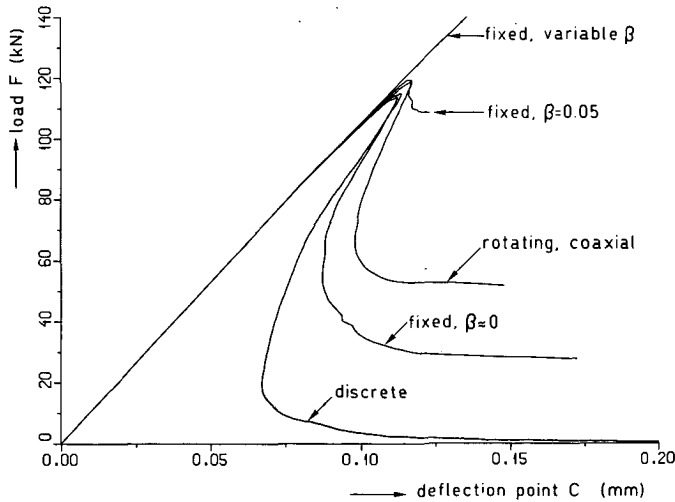

Fig. 6.7. Load F versus deflection point C of single-notched shear beam of Fig. 6.5.

85

Again, all smeared crack results are too stiff in the post-peak regime. Fixed cracks with β≈0 and coaxial rotating cracks are the only assumptions that lead to distinct softening, but the residual load does not drop below 25 and 45 percent of the limit load respectively. For the coaxial rotating crack result the principal stresses and the localization have been plotted in Figs. 6.8a and 6.9a. We observe that the number of "zig-zag" jumps remains only small because of the cross-diagonal mesh. The noise in the stress-plot is therefore less pronounced. Nevertheless, spurious stiffening from displacement compatibility definitely occurs, at either side of the localization.

For fixed cracks with β=0.05 the softening ceases to proceed already at a residual load of 90 percent of the limit load. Fixed cracks with the variable β provide no softening at all. Indeed, with these two computations severe stress rebuild in inclined directions was again encountered.
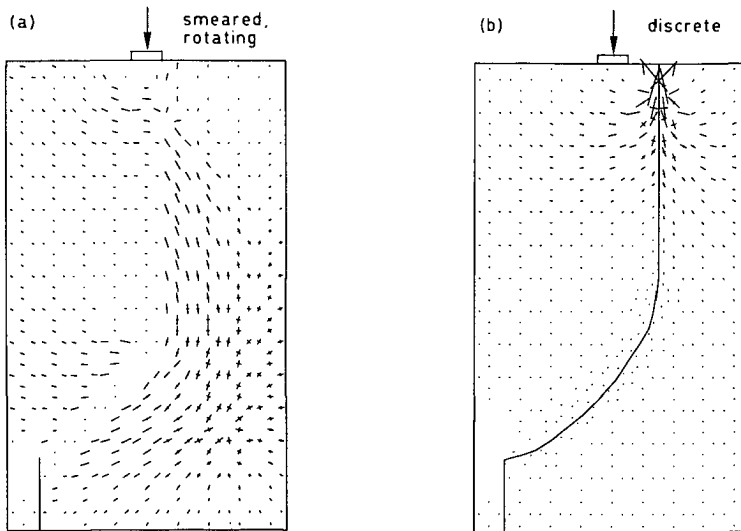
Fig. 6.8. Principal tensile stress trajectories for single-notched shear beam at final stage.
(a) Some stress-locking for rotating smeared cracks.
(b) Correct stress relief at either side of predefined discrete crack.

The tendency of the results is in line with the findings for the CLWL-DCB specimen. The phenomena have general validity. A third example that supports this assertion has been detailed separately[Rots 87e].

Only two minor discrepancies have been observed between the present shear beam and the CLWL-DCB specimen. Firstly, with the shear beam the result for β=0.05 is slightly less dramatic than with the CLWL-DCB specimen, where this assumption even failed in producing a limit load. Obviously, with problems of tension-compression stress-rebuild in inclined directions does slightly less harm than with problems of tension-tension. Secondly, with the shear beam the limit load for rotating

86
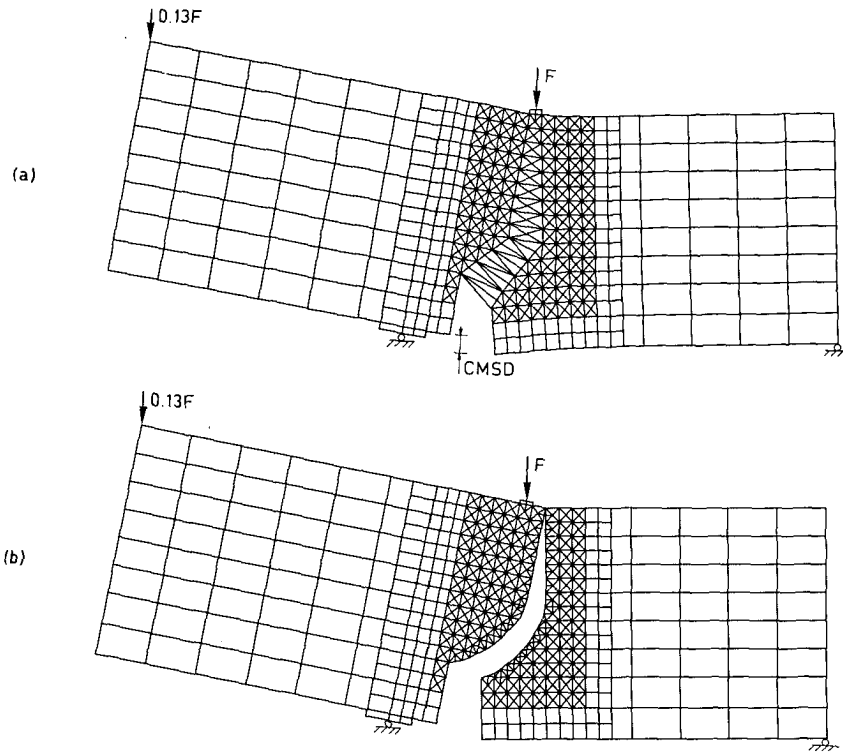
Fig. 6.9. Deformed meshes for single-notched shear beam at final stage.
(a) Localization for rotating smeared cracks.
(b) Genuine separation for predefined discrete crack.

cracks exceeds the limit load for fixed cracks with $\beta \approx 0$, whereas the converse holds true with the CLWL-DCB specimen. This is explainable from the fact that the tension-compression state for the present beam induces a different, and apparently higher value of the coaxiality-enforcing shear term $\sigma_{11}-\sigma_{22}/2(\varepsilon_{11}-\varepsilon_{22})$ than the tension-tension state for the CLWL-DCB specimen does.

The discrepancies between the two best possible smeared crack solutions, i.e. fixed cracks with $\beta \approx 0$ and coaxial rotating cracks, deserve some further attention. Firstly, analyses with the coaxial rotating crack concept generally show faster convergence than fixed crack analyses with $\beta \approx 0$. This is due to the fact that the coaxiality-enforcing shear term varies gradually after cracking, whereas the fixed cracks with $\beta \approx 0$ involve a sudden drop from elastic shear to zero shear upon cracking. Secondly, spurious kinematic modes (section 4.2) are encountered more frequently for fixed cracks with $\beta \approx 0$ than for rotating cracks. Thirdly, the rotating crack concept seems

87

more sensitive to directional bias than fixed cracks with $\beta \approx 0$. Yet, this trend was more pronounced for the square mesh of the CLWL-DCB specimen than for the present cross-diagonal mesh which minimizes bias.

The former two trends were found to be most pronounced, which argues in favor of the coaxial rotating crack concept.

With the present beam, the discrete crack solution is very illustrative since it shows softening down to zero. Indeed, *Fig. 6.9b reveals genuine separation.* Fig. 6.8b shows that the analysis does not render any locked-in stresses but, instead, the two separated parts of the beam at either side of the crack show full stress relief, which is in agreement with the physical process. The solution gives an excellent demonstration of the elastic-softening theory in that the energy supplied to the beam, which is represented by the integral of the master load $1.13F$ versus the master loading point displacement C in Fig. 6.7, precisely balances the fracture energy G_f times the surface area generated. With the smeared crack solutions such an interpretation is disturbed by the stress-locking.

The quantitative results of the experiment have been made available[Arre 82] only in terms of load-CMSD (Fig. 6.6). It appears that the discrete crack result does not fit this experimental result which shows a more stiff behavior in the post-peak regime. Aside from the fact that the responses are highly sensitive to the lay-out of the bearing platens under the rollers, this discrepancy is explainable from the fact that in the experiment energy may have been spent in compression nonlinearities and aggregate interlock in addition to creating the discontinuity.

We observe that the experimental load-CMSD curves have been terminated while the load had not yet come down to zero. Hence, it might even be claimed that some of the smeared crack results in Fig. 6.6 are not too bad. However, pictures have been published[Ingr 85b] that reveal a fully separated beam. This implies that also in the experiment the load *must* have come down to zero, which supports the essence of the discrete crack result. The fact that the shape of some of the smeared crack solutions in Fig. 6.6 fits the experimental result rather well must be regarded as a lucky coincidence since *it is incorrect to claim that stress-locking constitutes a reliable representation of e.g. aggregate interlock.* Rather, the present smeared crack results should have matched the ideal elastic-softening result for the discrete crack.

6.3 Conclusions

The possibilities and limitations of smeared crack concepts for simulating curved mode I fracture through regular meshes have been investigated. The treatment has been focused on the requirements to follow stress rotations. Table 6.I summarizes the

findings which are surprising since they cast doubt on much previous research having involved fixed cracks with shear retention.

mesh	crack concept	performance for localized fracture
regular	-fixed, smeared with significant shear retention	-dangerous, overstiff response -stress-locking from compatibility -severe stress-locking from stress-rebuild inclined to first crack
regular	-fixed, smeared with negligible shear retention	-structural softening can be predicted -stress-locking from compatibility -stress-rebuild parallel to first crack (no rotation)
regular	-rotating, smeared coaxial	-structural softening can be predicted -stress-locking from compatibility -proper stress/strain rotations
regular	-rotating, smeared non-coaxial	-stress locking from compatibility -difficulties with local unloading/reloading -difficulties in case of non-zero threshold angles -improper stress/strain rotations
predefined discontinuity	-discrete-crack-corrector	-genuine separation -softening down to zero -correct stress rotation and stress relief in adjacent elastic elements

Table 6.I. Performance of crack concepts for curved localized mode I fracture.

It is concluded that we cannot yet fully rely on smeared models for predicting localized fracture. Because of stress-locking it has been motivated to use a strategy of a smeared-crack-predictor followed by a discrete-crack-corrector (section 4.2.4). The present chapter supports this proposal and indicates that the most reliable smeared-crack-predictor is obtained using the coaxial rotating concept, or the fixed concept with negligible shear retention. Of these two concepts, the former is preferable since it leads to proper stress/strain rotations and generally shows faster convergence than fixed cracks with negligible shear retention.

7. FRACTURE AND BOND IN REINFORCED CONCRETE

To compensate for the softening of concrete, designers frequently add reinforcement. The bond between concrete and reinforcement then introduces a further complication into the fracture analysis. Some ten years ago the numerical modeling of bond-slip has received attention and various types of bond-slip elements have been proposed[Schaf 76,Dorr 78,deGr 81]. At that time the available crack models were less sophisticated, and the analysis was sometimes frustrated by shortcomings of the crack model while the bond-slip formulations were adequate[deGr 81]. To date, the reverse seems to hold true. Crack models have undergone rapid developments, but most existing simulators adopt the coarse and unsafe assumption of perfect bond[Nils 82]. Consequently, there is a need to rejuvenate bond-slip research with the achievements of crack concepts and elastic-softening models. This is the purpose of the present chapter.

The broad scope of the subject calls for a distinction into three approaches of decreasing degree of precision:

— resolution of bond-slip
   This strategy zooms at the micro-behavior in the vicinity of the reinforcing bar (rebar), where secondary transverse and longitudinal cracks are crucial mechanisms. The method aims at explaining the fundamentals of traction-slip behavior.

— bond-slip interface analysis
   This approach lumps traction-slip behavior into an interface, with a view to predicting the spacing and width of localized primary cracks in reinforced concrete members.

— tension-stiffening
   When the concrete is densely reinforced, distributed fracture occurs and even the above approach that zooms at primary cracks becomes too delicate. Tension-stiffening then accounts for the bond characteristics in an indirect manner.

7.1 Computational resolution of bond-slip

7.1.1 Modeling

-bond mechanisms-
   Confining attention to deformed rebars, the bond-slip, i.e. the tangential relative displacement between the rebar and the concrete (measured some distance away from the rebar), is controlled by four mechanisms[Rehm 61,Tepf 79,Bart 82]:

(a) elastic deformation,

(b) conical transverse cracking behind the ribs of the rebar (these secondary cracks arise internally at either side of an externally visible primary crack),

(c) longitudinal cracking in response to tensile ring-stresses,

(d) 'crushing' in compressive cones radiating out from the ribs.

Although experimental data are not decisive[Mirz 79,Gamb 85], the crushing is likely to occur only in case of lateral confinement, which is typical of anchorage bond and short-embedment pull-out tests. Such cases have been studied[Vos 83,Drag 87] and induce significant compression in front of the ribs. The present study considers long-embedment flexural bond, where the compressive stresses remain relatively small: from the output we did not observe stresses larger than 25N/mm^2, while a manual cal-culation that incorporates the rib surface characteristics provides additional justification for this assumption. For this reason, the crushing has been ignored and the analysis renders tensile cracking and elasticity.

-geometrical modeling-

We consider a tension-pull configuration, i.e. a center-placed rebar protruding from a concrete cylinder or block. The specimen is pulled at both ends and represents the conditions in the tension zone of a reinforced concrete member, between two pri-mary flexural cracks. Fig. 7.1 details the idealization which assumes axi-symmetry as well as mirror-symmetry. The dimensions correspond to a portion of the specimens tested by Dragosavić & Groeneveld[Drag 87], and also come close to the popular 6x6 inch specimens with a 1 inch diameter rebar[Nils 72,Mirz 79,Lahn 86]. The rebar is composed of four-node rectangles and the concrete of three-node triangles in a cross-diagonal pat-tern which minimizes directional bias.
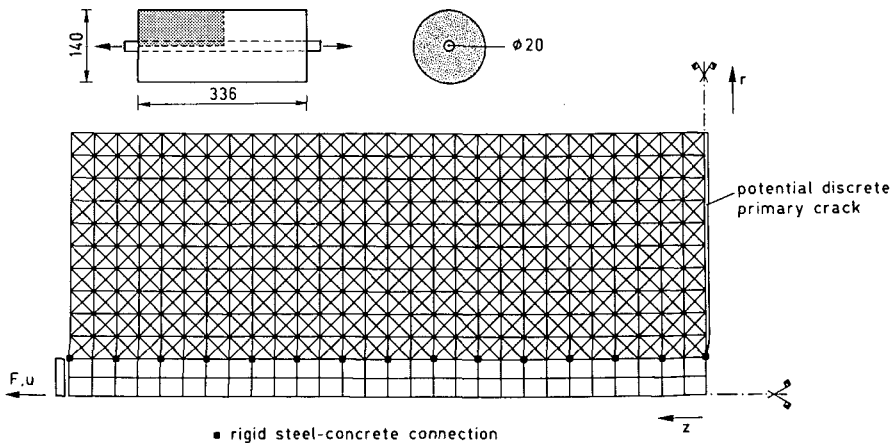

Fig. 7.1. Computational set-up to investigate bond-slip related cracks in a tension-pull configuration. The configuration is typical for a tension zone in bending.

Adhesion and friction along the steel-concrete interface have been neglected in favor of mechanical interlock provided by the ribs[Rehm 61]. The mechanical interlock was modeled by rigidly attaching the steel to the concrete at rib locations, while only partially attaching it between the ribs. The overlapping nodes at rib locations were tied to each other in the radial direction as well as in the axial direction, while the overlapping nodes at locations in between the ribs were tied to each other only in the radial direction. For a rib spacing of 12mm and an element size of 6mm this corresponds to an interchangeable tying scheme.

-material modeling-

The elastic-softening parameters were taken as E=25000N/mm^2, ν=0.2, f_{ct}=3.0N/mm^2, G_f^I=75J/m^2, nonlinear softening (Fig. 3.1), and secant unloading (Fig. 3.3). An axi-symmetric version of the smeared crack concept was adopted whereby the direction of longitudinal cracks was naturally fixed because of axi-symmetry, while transverse cracks were allowed to rotate so as to maintain coaxiality and to avoid overstiff response. The transverse cracks were assumed to localize within a band width h=6mm (Table 4.I). For the longitudinal cracks the definition of a band width was less evident, as will be discussed later.

Along the axis of mirror-symmetry discrete elements (in their lumped version) were incorporated with a view to capturing a probable primary crack. In order to activate this crack, the discrete elements were assigned a material imperfection. Although experimental researchers generally add a geometrical imperfection in the form of a starter notch[Dorr 78,Drag 87], the use of a material imperfection turned out to better suit the present study.

The investigation can be seen as an extension of the only existing computational study in this field by Ingraffea et al.[Ingr 84], which ignored longitudinal cracking and which was terminated at the onset of primary cracking.

7.1.2 Transverse cracks

-transverse secondary cracking-

The combined smeared/discrete crack analysis progressed as shown in Figs. 7.2 and 7.3, presenting the incremental deformations and crack patterns at typical load stages. Initially, transverse cracks form at the location where the steel exits the concrete (Fig. 7.2a). These cracks, discovered by Goto[Goto 71], nucleate behind the ribs and are cone-shaped. On subsequent loading, the early cracks propagate and additional secondary cracks nucleate further from the end-face. Although each rib of the rebar produces a secondary crack, Fig. 7.2b reveals that only a limited number of them survives while the others are arrested. This corresponds to experimental bond-crack

detections[Jian 84]. A further observation from Fig. 7.2b is that the earliest cracks close to the rebar show large openings in a direction perpendicular to the rebar. This suggests radial separation between the steel and the concrete, which confirms experimental findings[Goto 71] and conclusions from quasi-linear analyses[Lutz 67].
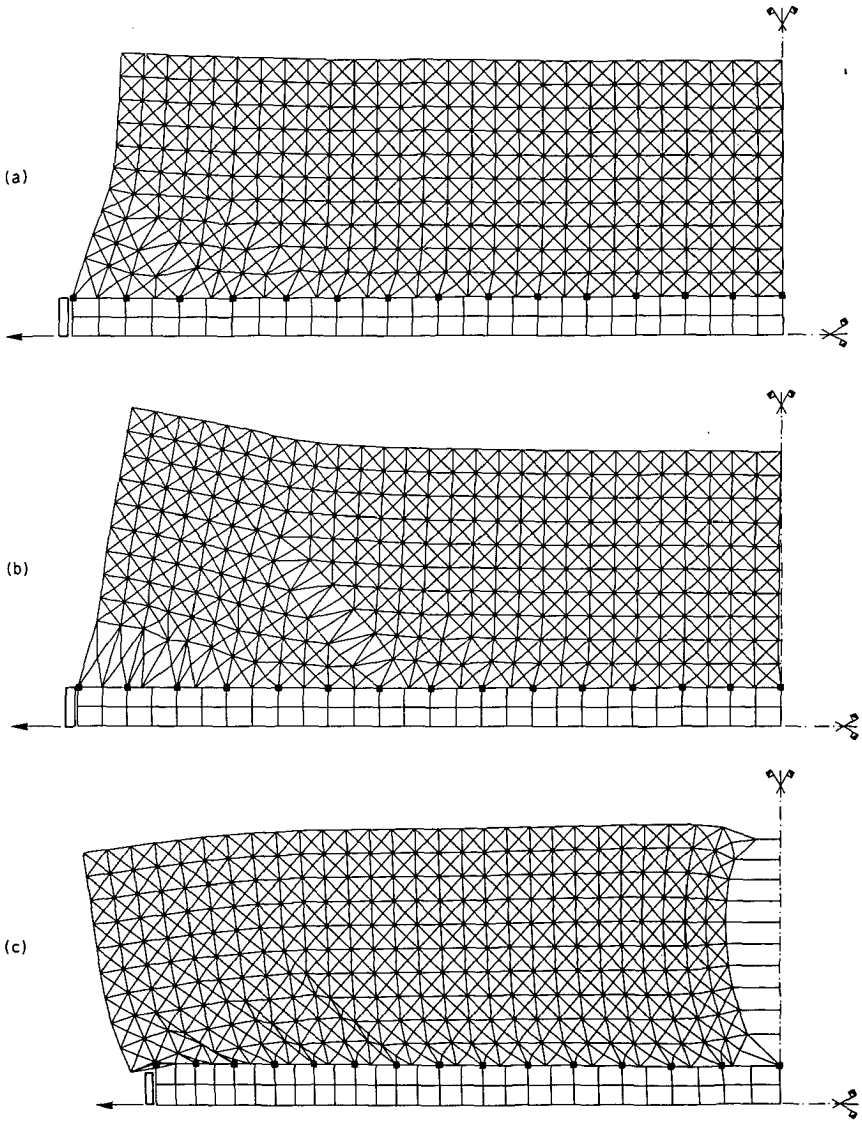

Fig. 7.2. Incremental deformations of tension-pull specimen.
      (a) early stage ($F = 32.7$kN)
      (b) at impending primary crack formation ($F = 51.4$kN)
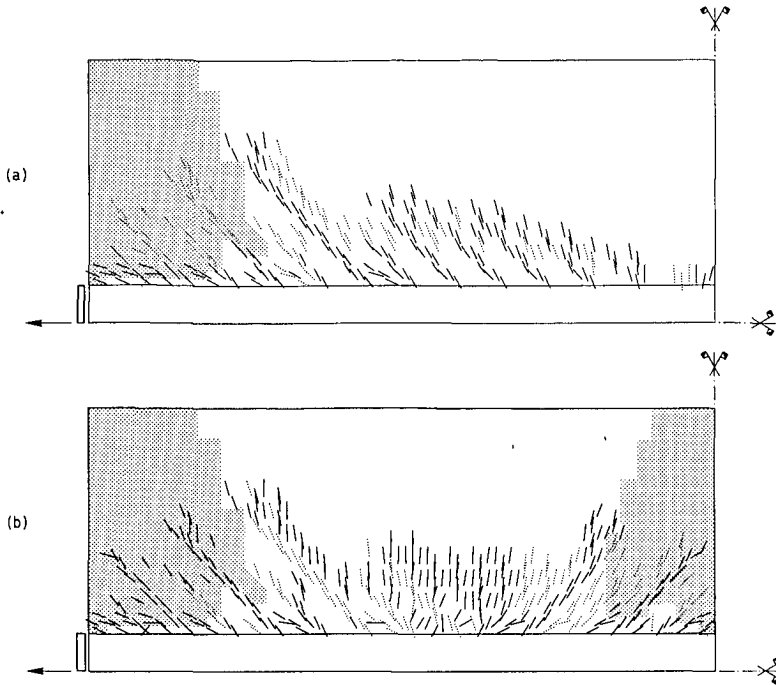   (c) at primary crack formation ($F = 51.6$kN)

Fig. 7.3. Crack formation in tension-pull specimen.
(active cracks drawn, inactive cracks dotted, longitudinal cracks shaded)
(a) at impending primary crack formation (F =51.4kN)
(b) final stage, beyond primary cracking.

-transverse primary cracking-

Although secondary cracks rapidly diminish the concrete tensile capacity, the present specimen length renders sufficient tension at mid-section to trigger the primary crack. Fig. 7.2c and the load-elongation curve of Fig. 7.4 reveal the catastrophic nature of this crack, which is in agreement with previous descriptions that call primary cracks unstable[Goto71]. While traversing the catastrophic softening regime, the existing secondary cracks near mid-section showed significant rotation in order to slant towards the free surface provided by the primary crack. When the softening of the primary crack was completed, the load could be incremented again. Secondary cracking and radial separation adjacent to the primary crack proceeded, while the early secondary cracks at the end-face started to re-load in order to finally re-soften.

-performance of crack concept-

A major observation is the potential of the coaxial rotating crack concept to accurately capture the stress/strain/crack rotations involved in primary cracking. The output did not signal any violation of the coaxiality norm of 0.1 degrees, whereby it is

noted that in total a number of 160 load-steps were performed, their size ranging from 0.03 kN in critical stages to 0.75 kN in less critical stages. Neither did the analysis noticeably suffer from spurious kinematic modes, so that a proper tangent stiffness matrix could be maintained throughout the entire iterative process. Preliminary analyses[Rots 85c] with fixed multi-directional cracks of thirty degree inclination were less successful in this respect, owing to the discontinuities involved in the interval-adaptation of the leading crack direction to the direction of principal stress, to the shear retention model producing overstiff behavior and to the occurrence of fixed spurious modes.
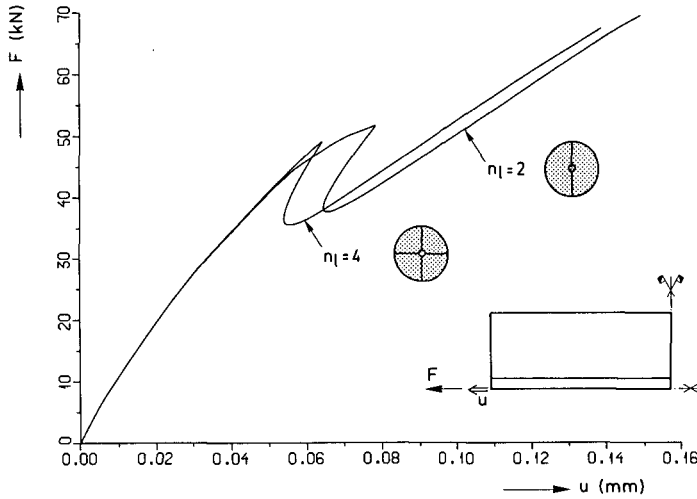
Fig. 7.4. External load versus end-displacement rebar of tension-pull specimen,
for different number n_l of localized longitudinal cracks (section 7.1.3).
The result for n_l=2 corresponds to the analysis of the present section.

7.1.3 Longitudinal cracks and the importance of their band width

Initially, the external force is transferred from the steel into the concrete primarily via axial tensile stresses. On transverse secondary cracking this type of bond action is lost and the transfer of bond forces is subsequently furnished by compressive cones that radiate out from the ribs. The radial components of the compressive cones are balanced by rings of tensile stress, as shown in Fig. 7.5a[Tepf 79]. When the ring is stressed to rupture a longitudinal crack arises and the balance against the compressive cones is lost, which causes a further break-down of bond.

Fig. 7.5. Bond mechanisms for a deformed rebar, after transverse cracking.
(a) Bond action via compressive cones and tensile rings[Tepf 79].
The tensile ring may give rise to longitudinal cracking (splitting).
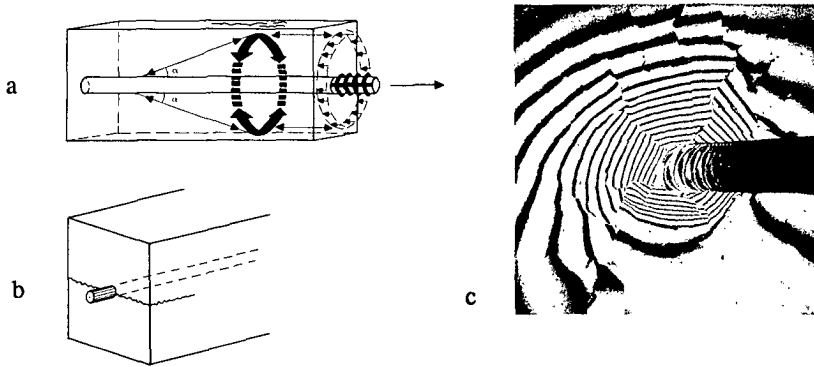(b) Bond-splitting with $n_l=2$, typical pattern from engineering practice.
(c) Bond-splitting with $n_l=4$, obtained by holographic interferometry[Bera 80].

Fig. 7.3 presents the extent of longitudinal cracking and Fig. 7.6 gives a qualitative impression of the associated ring stress with increasing stage of the loading process. Initially, ring stresses are highly concentrated near the end-face, where the steel exits the concrete (Fig. 7.6a). The first longitudinal cracks soon arise and the resulting tangential softening involves significant redistribution as we observe a front of ring stresses that gradually travels away from the end-face (Fig. 7.6b). After primary cracking this phenomenon replicates itself near mid-section, and the final distribution of Fig. 7.6c is stable as further load increments are resisted by the steel rather than by the damaged concrete, the tensile capacity of which is almost exhausted.

Because of axi-symmetry it was impossible to model localization of the longitudinal cracks, which places their band width h in an unclear position. From experimental work[Bera 80,Losb 79,Tepf 79,Schm 86] such localization is known to occur, as is exemplified by Figs. 7.5b and 7.5c revealing two respectively four localized longitudinal splitting cracks through the peripheri. This information can be transferred into an a priori assumption of the band width according to

$$h = \frac{2\pi R}{n_l} \tag{7.1}$$

where R is the distance to the axis of rotation and n_l is the imagined number of localized longitudinal cracks. The use of (7.1) implies n_l times G_f^I to be consumed in the smeared longitudinal crack.

96

The above result was obtained for $n_l=2$ which provides a safe assumption. According to (3.9), the corresponding band width for the outer integration points with $R > 48.9$mm even becomes that large that the local stress-strain relation for the present set of elastic-softening parameters displays a snap-back. To remedy this, automatic reduction of the strength limit f_{ct} was inserted (section 3.1.5). *This steep softening confirms the widespread notion that bond splitting is brittle and dangerous.*
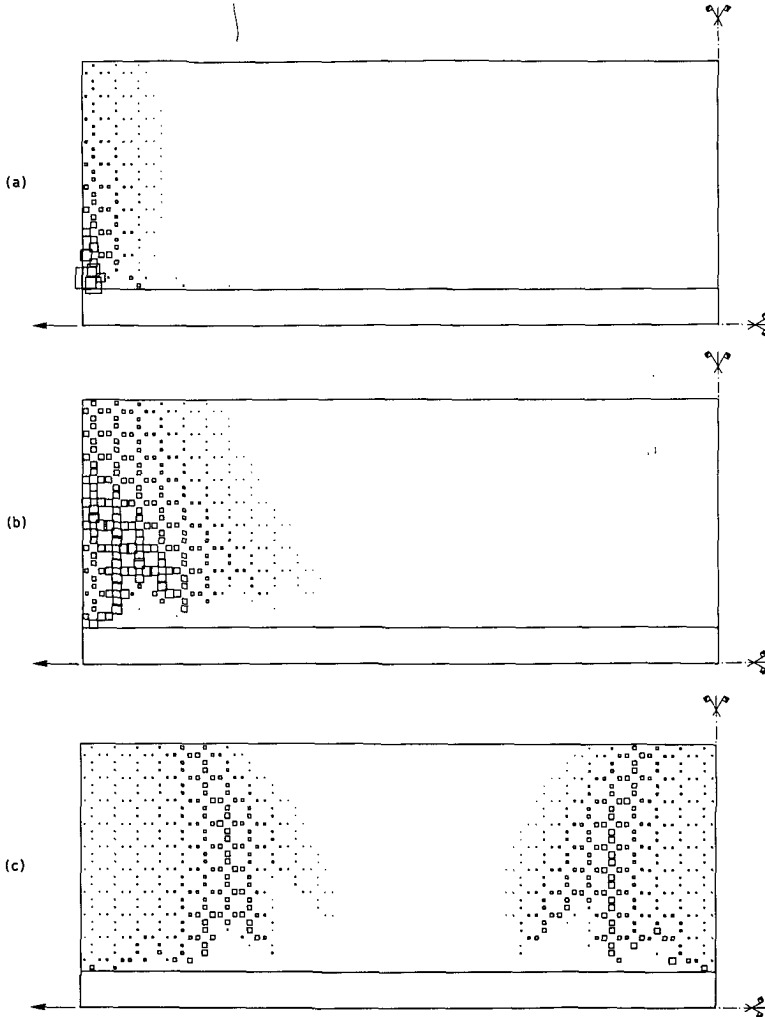

Fig. 7.6. Redistribution of tensile ring stress in tension-pull specimen.
Size of square is proportional to the magnitude of the stress.
(a) initial stage (linear-elastic)
(b) subsequent stage ($F=37.2$kN)
(c) final stage ($F=68.1$kN), beyond primary cracking.

An additional analysis was carried out for $n_l=4$, which doubles tangential toughness. Fig. 7.4 reveals a subtle discrepancy between the load-elongation curves predicted. The previous analysis with $n_l=2$ not only shows enhanced pre-peak nonlinearity, which is evident from the steeper softening in longitudinal cracks, but it also surprisingly shows the limit load at primary cracking to increase. Obviously, the rapid loss of ring stress transfer for $n_l=2$ quickly breaks down the bond action via the compressive cones and, hence, it *indirectly* accounts for a decrease in axial stress transfer to the concrete at mid-section. This postpones primary crack formation and the associated increase of the limit load is explainable from the enhanced contribution of the steel relative to the concrete in resisting the external load. A trial analysis for an even steeper softening ($n_l=2$ in conjunction with $G_f^l=37.5J/m^2$) underlined this tendency and even prevented the specimen from primary cracking at all, while it snapped on longitudinal cracking. The results reveal the integrated action of axial tensile zones, radial compressive cones and tangential tensile rings.

The bond capacity is dangerously overestimated not only when longitudinal cracks are ignored altogether[Ingr 84], but also when the band width for longitudinal cracks is quantified erroneously[Rots 85c], for instance by simply equating it to the band width for transverse cracks (6 mm) which for the outmost sampling points ($R=69mm$) would result in a 36-fold (!) overestimation of the tangential softening capacity compared to (7.1) with $n_l=2$. The issue is also relevant with other axi-symmetric problems, like punching shear, or the pull-out of an anchor (chapter 8).

Ideally, one should undertake a fully three-dimensional analysis to remove the uncertainties in the imagined value of n_l. Preliminary results thereof revealed the potential of predicting longitudinal fracture localization[Rots 87c] ‡.

7.1.4 Predicting bond traction-slip curves

Let us extract some more quantitative information from the analysis. The bond shear traction has been plotted against the bond-slip in Fig. 7.7, both for $n_l=2$ and $n_l=4$, whereby the curves have been terminated at the onset of primary cracking. The shear traction and the slip have been defined as the average values for a segment in between two ribs. The particular segment underlying Fig. 7.7 was located at a distance $0.9D$

---

‡ Caution must be exercised whenever some kind of symmetry, anti-symmetry or axi-symmetry is introduced in the model. The correct localization may be easily missed and both strength and stiffness may be overestimated. For mirror-symmetry this was exemplified by the direct tensile test of section 5.1, and for anti-symmetry an example has been published[Rots 87b].

from the end-face, with D denoting the rebar diameter. The traction was determined as the segment-average shear stress of the two integration stations at distance $1.05D$ from the axis of rotation, whereafter a surface-correction of $1.05D/0.5D$ was inserted in order to objectively relate them to the interface surface. The slip was defined as the average of the two node-sets at either side of the segment. These schemes correspond to accepted definitions from experimental research[Drag 87].
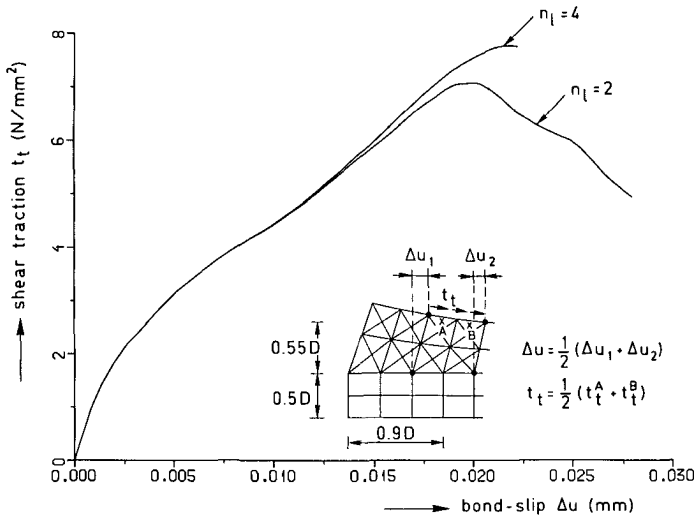

Fig. 7.7. Local shear traction versus slip in tension-pull specimen, for $n_l=2$ and $n_l=4$ (distance 18mm from end-face).
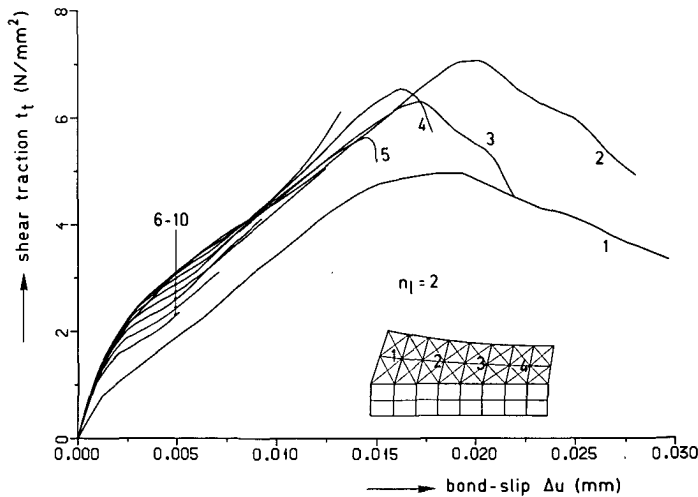

Fig. 7.8. Local shear traction versus slip in tension-pull specimen, with increasing distance from end-face ($n_l=2$).

The curves show a linear-elastic stage, a stage of decreased stiffness and a softening stage. The stage of decreased stiffness is primarily attributable to transverse secondary cracking and the softening stage to longitudinal cracking. The latter assertion is evident from the fact that n_l=2 yields far more softening than n_l=4. This underlines the importance of the indirect bond action via compressive cones in conjunction with tensile rings. The trilinear curves of Fig. 7.7 provide a justification of analytical bond-models[Drag 84] that were derived on the line of argument. The slip modulus of the second stage of the curves (k_t≈300N/mm^3) falls within experimental scatter[Dorr 78,Lahn 86].

Experimental determinations of traction-slip behavior show significant scatter[Dorr 78,Lahn 86]. A possible cause is the actual location of the sampling points where traction and slip are recorded. However, there is no consensus on this question since Nilson[Nils 72] and Dorr[Dorr 78] found the curves to depend on the distance from the loaded end-face, while Mirza & Houde[Mirz 79] report them to be location-independent. To verify this, the curves for the first twelve segments from the end-face have been collected into Fig. 7.8 for the analysis with n_l=2. Apart from the curve for the first segment, which shows very weak behavior, the curves fall within a relatively narrow band. This suggests that at least the rising portion of the traction-slip curve is location-independent. The only discrepancies relate to the peak traction and to the subsequent softening, which do not show a systematic trend for they depend on local secondary cracking which is non-uniform along the rebar axis.

For cases of bond that are not critical to longitudinal splitting, e.g. flexural bond with sufficient cover, the present results justify application of a unique traction-slip curve. In other cases, the non-local format of traction-slip laws poses a problem as information like 'distance from the primary crack' is usually not available at local integration point level. For this reason, the search for local parameters like radial pressure[Dorr 78,Drag 87,Vos 83] should be continued, although the necessity of pursuing high accuracy is doubted since the majority of practical analyses refers to plane-stress configurations where circular bars are replaced by fictitious layers such that identities like radial bond component and lateral pressure are hardly definable.

7.2 Bond-slip interface analysis

In engineering practice, the above approach becomes too delicate and it is preferable to lump the traction-slip behavior into a fictitious interface. The technique is not new. It has been introduced by Rehm[Rehm 61] in order to subsequently evolve into a powerful tool for predicting the spacing and width of primary cracks, both analytically[Noak 78,Tepf 79,Brug 87] and numerically[Groo 79,deGr 81]. Invariably, these approaches

100

adopted a sudden stress drop for the concrete after cracking. A consistent combination of the interface laws with novel softening models for the concrete has received only little attention. The purpose of this section is to present such a combination.

-modeling with interface elements-

We consider the long-embedment tension-pull specimen of Fig. 7.9[Gijs 77]. The steel is modeled by truss elements, the bond-slip layer by interface elements and the surrounded concrete by continuum elements. Linear elements were adopted and the interface elements were employed in their lumped version.

Again, axi-symmetry was assumed. In contrast to the preceding analysis the mirror-symmetry was omitted with a view to predicting primary crack spacing over the entire embedment length via random generation of tensile strength[Groo 79,Cris 82,Witt 87]. To this end, f_{ct} was assigned a Gaussian distribution with a mean value of 3.0N/mm^2, a standard deviation of 0.5N/mm^2 and a cut-off at 1.5 and 4.5 N/mm^2. In order to prevent primary cracks from zig-zagging, the Gaussian distribution was not inserted at integration point level or at element level, but it was applied at element assemblies belonging to the same z-coordinate. The coaxial rotating crack concept was adopted. The parameters were taken as $E=28000$N/mm^2, $v=0.2$, $G_f^I=100$J/m^2, $h=8.7$mm, non-linear softening (Fig. 3.1) and secant unloading (Fig. 3.3).
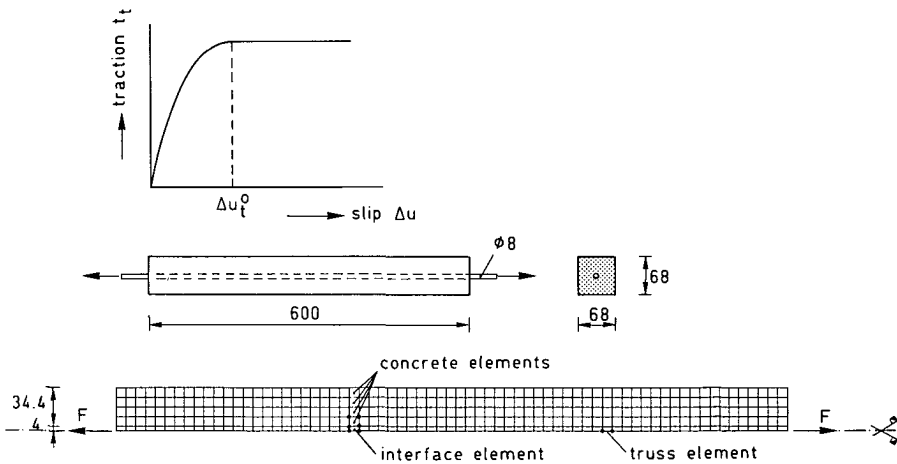
Fig. 7.9. Set-up and assumed shear traction-slip curve for interface analysis of long-embedment tension-pull specimen[Gijs 77].

To date, experimental data with respect to the normal (radial) bond component are scarce and hardly transferable into constitutive laws. For this reason, the interface normal behavior and shear-normal coupling were not incorporated, implying the interface to reduce to a mode II shear interface. The shear traction-slip $t_t-\Delta u_t$ relation has been assumed to be unique along the bar axis. Although the preceding section

101

suggests a trilinear relation, we preferred to start from a simpler relation that ignores the softening stage (a discussion is made afterwards). The following relation has been invoked[Mehl 85,Dorr 80]:

$$
t_t = \begin{cases} af_{ct} \left[5 \left[\dfrac{\Delta u_t}{\Delta u_t^0} \right] - 4.5 \left[\dfrac{\Delta u_t}{\Delta u_t^0} \right]^2 + 1.4 \left[\dfrac{\Delta u_t}{\Delta u_t^0} \right]^3 \right] & \text{if } \Delta u_t < \Delta u_t^0 \\[2ex] 1.9 af_{ct} & \text{if } \Delta u_t \geq \Delta u_t^0 \end{cases} \tag{7.2}
$$

The constants a and Δu_t^0 have been taken as 1 and 0.06 mm respectively (Fig. 7.9). Unloading and reloading of the interface shear behavior were modeled using a secant approach. Although (7.2) ignores non-local phenomena like radial separation and longitudinal cracking, these effects may be partially obtained via the concrete elements that surround the interface elements.

-global response-

Fig. 7.10 presents the load-elongation response which shows four local maxima corresponding to the successive development of four primary cracks. Beyond formation of the fourth primary crack, the crack pattern was fully developed (stable crack spacing) and the solution could be continued up to yielding of the reinforcement without further physical changes. During that stage only the width of the primary cracks, which simply equals the crack strain times their band width, increased.

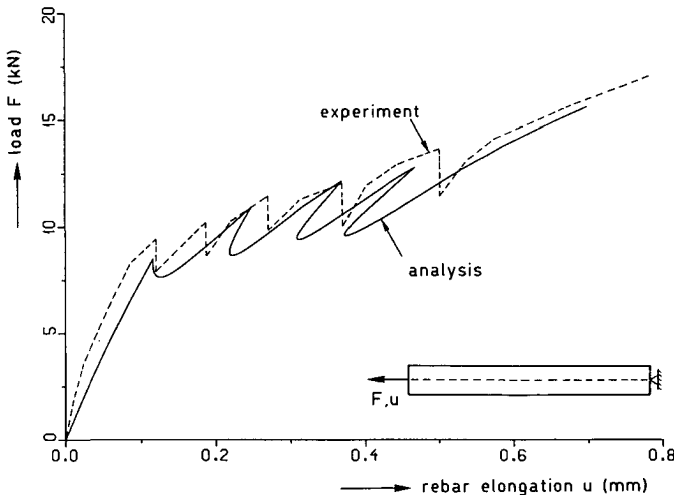
Fig. 7.10. Load-elongation response for long-embedment specimen of Fig. 7.9.

The serrated type of curve is in agreement with experimental results[Gijs 77] and justifies engineering models[e.g.Brug 87]. Experimentally, the serration peaks were jumped over in direct displacement control, whereby "the occurrence of visible cracks at the

outer surface was accompanied by a sudden drop of the load"[Gijs 77]. Although the numerical analogy thereof performed adequately in combination with a fixed crack concept[Rots 85c], it failed for the present analysis with rotating cracks since the drift from the coaxiality condition during the sudden drop of the load led to divergence. For this reason, the serration peaks and sharp snap-backs were passed under opening-displacement control of the associated primary crack (section 4.1).

-localization of primary cracks-

The primary cracks have been plotted in Fig. 7.11. We observe that the statistical distribution of strength correctly induces localization. The use of strength perturbations is consistent with the physical process in heterogeneous materials and performs adequately provided that the load increments are taken sufficiently small to prevent several local peaks from being overshooted simultaneously. If the strength perturbations are omitted and/or the load steps are too large, a wide band of elements cracks owing to the existence of an 'undisturbed zone' of homogeneous stress and geometry. In such cases serious difficulties arise from alternative equilibrium states, as pointed out by Crisfield[Cris 82].
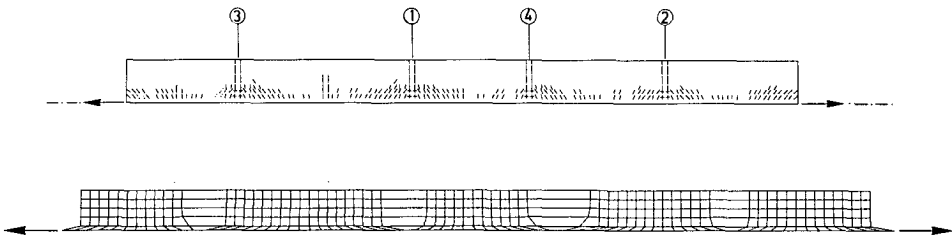
Fig. 7.11. Final configuration of primary cracks for specimen of Fig. 7.9.

Fig. 7.12 details the redistribution involved in primary cracking. Initially, interface tractions occur solely near the end-faces where the external load is transferred to the concrete (Fig. 7.12a). On primary cracking the specimen separates and the initial behavior near the end-faces repeats itself at either side of the primary crack. The final profiles after four primary cracks show significant fluctuation, which demonstrates the need for fine meshes in such an approach. The profiles of the steel stress (Fig. 7.12b) properly reveal that the reinforcement compensates for the loss of tensile load carrying capacity at places of primary cracks.

The agreement of the traction profiles with experimental measurements from internal strain gauges[Dorr 80,Lahn 86,Drag 87] is surprising, considering the simple bond-slip law adopted (without incorporation of lateral effects). The only discrepancy relates to the softening of the shear traction near primary cracks, which is evident from such experiments (especially from[Drag 87]) as well as from the micro-approach of the preceding

section, but it is not covered by the traction-slip law of (7.2). The quantification of this softening component needs attention in future.
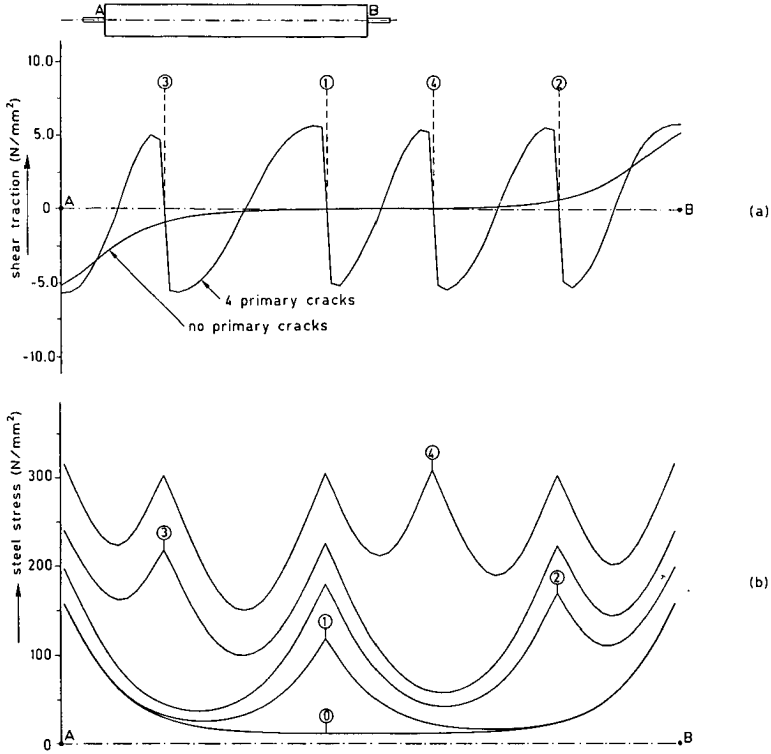
Fig. 7.12. Profiles of shear traction (a) and steel stress (b) along the interface for the long-embedment specimen of Fig. 7.9.

-is the inclusion of bond-slip essential?-

The question must be raised whether the inclusion of bond-slip is truly essential, or whether the usual assumption of perfect bond[Nils 82] also performs adequately. To gain insight, we consider a more illustrative problem of a slender beam that contains a dominant reinforcing layer and that fails in bending[Rots 85c]. Fig. 7.13 summarizes the main result in the form of a comparison between the crack patterns for perfect bond and for an analysis including bond-slip.

The perfect bond assumption gives rise to diffusion and distortion in the neighborhood of the reinforcement, whereas with bond-slip the primary cracks cross the reinforcement in a correct way. Indeed, our general experience is that *the inclusion of bond-slip improves the localization of primary cracks for problems with concentrated reinforcing layers.*

104

Fig. 7.13. Crack patterns for slender reinforced beam with dominant reinforcing layer at the tension side; (a) bond-slip included; (b) perfect bond.

A second, related disadvantage of perfect bond is that the associated tendency towards diffusion magnifies the difficulties with alternative equilibrium states[Cris 82]. The technique of strength perturbation, which aims at reducing the number of alternative equilibrium states, will consequently fail more quickly for perfect-bond analyses than for analyses including bond-slip.

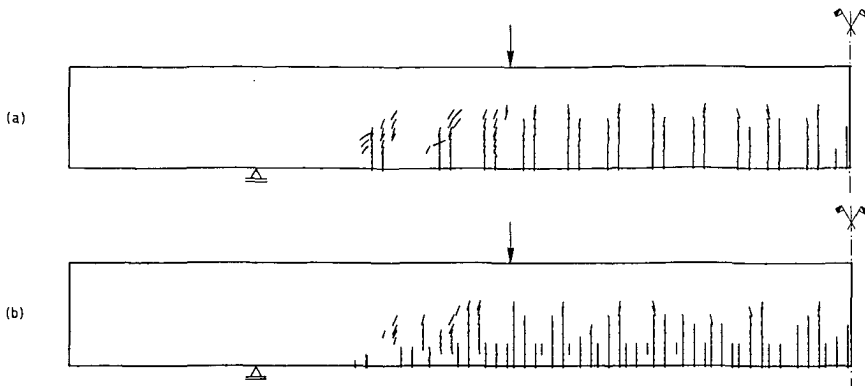Thirdly, perfect bond is incapable of making a direct distinction between, for example, plain rebars and deformed rebars. This is unacceptable if the structure is bond-critical. Although it is possible to enhance the perfect bond assumption with techniques that account for the rebar surface characteristics in an indirect manner (e.g. tension-stiffening), such techniques do not fit problems of concentrated reinforcement. This is because *it is inconsistent to start from diffuse-fracture models in the neighborhood of the reinforcement and to continue with localized-fracture models some distance away from the reinforcement.*

Bond-slip elements provide the possibility of accounting for the rebar surface characteristics in a direct manner. Another example has been published[Rots 87d], where some particular surface characteristics had to be included to simulate the pull-out of a lapped splice[Rots 87d].

7.3 Towards a unified approach of localized and distributed fracture

-statement of the problem-

The previous section considered primary cracks as "through a magnifying glass". When the primary crack pattern is densely distributed, this approach becomes unwieldy and the bond characteristics must be accounted for in an indirect manner via tension-stiffening[Gilb 78]. It is curious that such techniques have been introduced in a way that is very similar to tension-softening, namely via a descending branch in the

105

tensile stress-strain curve[Lin73]. The dualism arises from the fact that the response of a rebar surrounded by cracked concrete is *softer* than the response of a rebar surrounded by elastic concrete, while it is *stiffer* than the response of the rebar alone. This has led to some misunderstanding, culminating into a black-box character[vanM87] of the ultimate strain ε_u^{cr} of the descending branch (Fig. 3.1).

This section contributes to this topic from the viewpoint of a concrete panel that is densely reinforced in the x-direction and unreinforced in the y-direction. A tensile loading in the x-direction induces distributed fracture which calls for tension-stiffening, whereas a tensile loading in the y-direction induces localized fracture which calls for tension-softening. If shear stresses are added, cracks occur that do not coincide with the x- or y-direction. Which type of softening or stiffening has to be applied in such cases?

Novel insight in the gradual transition between the two extremes was recently provided by Bhide & Collins[Bhid87] and Kollegger & Mehlhorn[Koll87], who tested a number of such panels under various conditions of tension (in the x-direction) with shear. Incipient cracking occurred in a distributed fashion, whereas ultimate failure was governed by localized fracture after significant 'crack rotation', as reproduced in Fig. 7.14. In an effort to analytically model this behavior, it was concluded that the actual behavior is highly complex[Bhid87,Koll87] and that it "would not be realistic to try and quantify all mechanisms involved, especially since a simple expression is required"[Stev87].
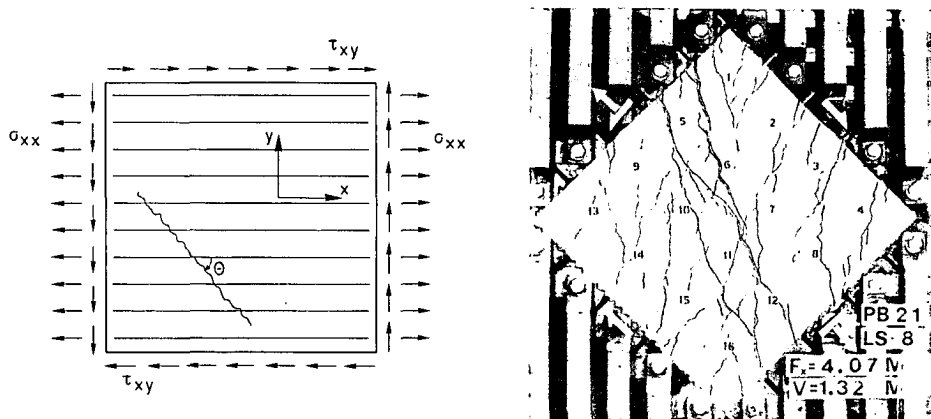

Fig. 7.14. Single-reinforced tension-shear panel PB21[Bhid87] with
tension-stiffening (distributed fracture) in the x-direction and
tension-softening (localized fracture) in the y-direction.

106

-modeling-

A first mechanism that can be eliminated is the nonlinearity of concrete in compression. This is because the tensile-shear loading was designed such that the compressive stresses remain small. Furthermore, we start to ignore dowel action and aggregate interlock. Fracture is modeled using a descending stress-strain relation. When the fracture is localized, this relation is derived from the tension-softening concept of invariant fracture energy G_f, which yields the tangent modulus D^I of (3.5),

$$D^I = -\frac{f_{ct}^2}{k}\frac{h}{G_f}$$ (7.3)

in which the crack band width h is fully determined by the finite element discretization. As the panel is intended to represent a small portion of a large structure, e.g. a shell structure, it is accordingly modeled as a single finite element so that h_l for localized fracture equals the panel dimension.

In an attempt towards unification, the postulate of invariant fracture energy may be applied also to distributed fracture. Assuming a system of n cracks of spacing s to consume n times G_f^I, we observe that the crack band width h_d for distributed fracture equals the spacing s. The key in this formulation is that the crack spacing s, which was output of the analysis of the previous section, now serves as an input parameter.

The gradual transition from localized to distributed fracture lies in a relation that lets h vary between the two extremes as a function of the inclination angle θ between fracture and rebars. Two possible choices will be examined, viz. a linear function

$$h = h_l + \frac{\theta}{\pi/2}\left[h_d - h_l\right]$$ (7.4)

which corresponds to experimental results[Bhid 87], and a sine curve inspired by a previous model[Vecc 86],

$$h = \frac{h_d}{\sin\left[\theta\dfrac{\pi/2-\theta_0}{\pi/2} + \theta_0\right]}$$ (7.5)

in which $\theta_0 = \arcsin(h_d/h_l)$. In practice, the extreme h_d for distributed fracture being based on e.g. the CEB model code[CEB 78], turns out to produce a steeper softening curve, i.e. a larger value of D^I in (7.3), than is generally measured from uniaxial tension-stiffening tests. The explanation lies in the fact that such tests involve the energy to be consumed not only in the formation of the primary crack, but also in bond-slip associated damage (secondary cracks) adjacent to the primary cracks. Hence, there is little argument to let not only h but also G_f depend on θ. Herein, we

107

will use a linear function for this purpose,

$$G_f = G_f^l + \frac{\theta}{\pi/2}\left[G_f^d - G_f^l\right] \tag{7.6}$$

in which G_f^l denotes the genuine fracture energy for localized fracture and G_f^d the enhanced fracture energy for distributed fracture in reinforced concrete. Combining (7.4) or (7.5) with (7.6) yields the quotient h/G_f that determines the steepness of the softening according to (7.3). It is depicted graphically in Fig. 7.15.
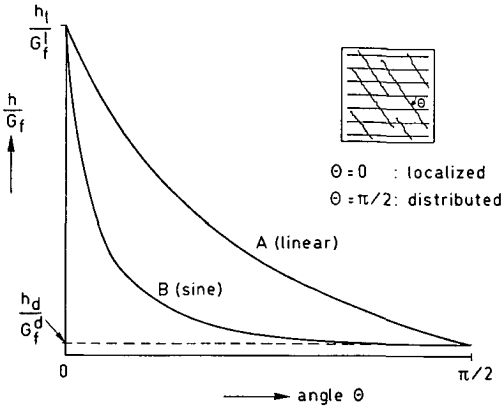
Fig. 7.15. Possible relations of h/G_f for the transition from localized to distributed fracture, as a function of the fracture-rebar inclination angle θ.

It is recognized that the transition functions imply simplifications. For instance, the interpretation of a continuously changing "fracture energy" for distinct non-orthogonal cracks is elusive compared to the interpretation of a fixed fracture energy for a single rotating crack (section 3.2.3). However, the outcome is believed to be less arbitrary and less mesh-sensitive than the empirical approaches that start from ε_u^{cr}.

The dependence of the constitutive formulation on the orientation θ fits the nature of the multi-directional crack concept since the capability of this concept to accommodate new traction-strain relations in new directions is then fully exploited. With the present panels, the multi-directional crack concept was adopted in its limiting case of the coaxial rotating crack concept, i.e. with zero threshold angle and shear modulus of (3.17).

-results-

Numerical experiments were undertaken on a panel[Bhid 87] with dimensions 890x890x70mm, a reinforcing percentage of 2.195% and a ratio of normal stress σ_{xx} versus shear stress τ_{xy} of 3.0. The panel (PB21) is one out of a series of six, but it is representative as analyses on the other five did not provide additional information. The parameters were taken as $E=20000$N/mm^2, $v=0.2$, $f_{ct}=2.0$N/mm^2, exponential

108

softening function, $G_f^l=100J/m^2$, $G_f^d=3G_f^l$, $h_l=890mm$, $h_d=50mm$ (estimated from CEB model code[CEB 78]). The reinforcing steel was given a Young's modulus $E_s=210000N/mm^2$ and a yield stress $f_s=400N/mm^2$. The analysis was performed under linearized arc-length control.

The response is shown in Fig. 7.16 in terms of the nominal shear stress τ_{xy} versus the nominal principal tensile strain ε_{11}. The linear function of (7.4) significantly underestimates both the strength and the ductility of the panel. Beyond incipient cracking at $\tau_{xy}=0.645N/mm^2$ the panel is able to sustain only a very slight increase of the external stress up to $\tau_{xy}=0.649N/mm^2$, whereafter it rapidly starts softening. The sine function of (7.5) increases the limit point up to $\tau_{xy}=1.037N/mm^2$, which gives a better match of the experimental result. With this computation also the predicted 'swing' of the crack from a rebar inclination of 71° at initiation up to 42° at limit point reasonably matches to the experimental result (66° and 31° respectively). However, the post-peak behavior is again too flexible as significant softening is calculated while the experiment shows ductile behavior without softening.

On further varying the transition functions of (7.4) to (7.6) no significant improvements were obtained in this respect since only the peak load altered but not the softening response. It is furthermore noted that the sine curve of (7.5) is already progressive in the sense that it increases the crack band width only slightly for a fairly wide range of θ-values in between 90° and 45°. Neither did variations in the other parameters or in the crack concept resort a positive effect. Apparently, the stiff and ductile response, which is typical of nearly all experiments by Bhide[Bhid 87], is *not* related to the softening/stiffening properties.
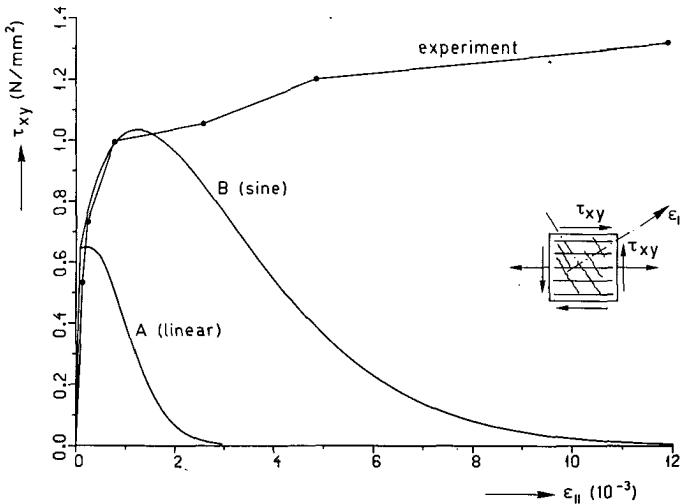

Fig. 7.16. Shear stress versus principal tensile strain for panel PB21.
"A" and "B" correspond to the transition curves A and B of Fig. 7.15.

Viewed in retrospect, the fact that the above approach fails in producing ductility for the single-reinforced panel is plausible. Since (a) there is reinforcement only in the x-direction, (b) there is no external confining pressure in the y-direction, and (c) the shear stress across the inclined crack is zero because of the ignorance of aggregate interlock and dowel action, a simple consideration of equilibrium shows that the resultant of the steel stress in the direction parallel to the crack cannot be balanced. Hence, the steel stress *must* follow the softening for the rotating crack and decrease automatically, as must the external stresses at the panel.

The clear lesson is that the embedment of unified softening/stiffening relations within smeared crack concepts is only a step towards understanding the highly complicated behavior of diffusely cracked reinforced concrete. Inevitably, the contribution of dowel action and aggregate interlock, analytical expressions of which are available[e.g.Pruy 88], has to be included in the numerical model. A similar conclusion has been recently reached with respect to shear failure in case of concentrated reinforcement[Chan 87].

A variety of researchers[e.g.Bala 87,Cris 87,Milf 84] has been able to fit the experimental results of orthogonally-reinforced panels without mentioning these phenomena. This may be due to the fact that the restraint from the orthogonal reinforcement compensates for the softening, implying such panels to be less critical to the phenomena than the present single-reinforced panels. A unified approach should cover both cases.

7.4 Summary

Three interrelated approaches have been presented that rejuvenate bond-slip research with recent developments of crack concepts and softening models.

A *detailed resolution of bond* requires proper softening laws for transverse secondary cracks and longitudinal splitting cracks as input, and produces traction-slip laws as output. The simulations provide new insight in the fundamentals of bond and give an extension to experimental research.

An *intermediate approach with bond-slip interface elements* requires traction-slip laws as input, and provides a configuration of localized primary cracks as output. For cases of concentrated reinforcement this approach fits the treatment of localization and is preferable over the use of perfect bond.

A *global strategy of unified softening/stiffening relations* requires crack spacing as input, and is applicable to structures that may fracture either in a localized or a distributed fashion. However, existing experimental data for single-reinforced panels cannot be reproduced. Extensions to include dowel action and/or aggregate interlock are inevitable for such cases.

110

# 8. PRACTICAL EXAMPLES OF LOCALIZED FRACTURE SIMULATION

This chapter concludes the study with two examples of localized fracture that integrate the aspects of crack concepts, softening models and bond-slip. The first example is a simulation of a laboratory test, whereas the second involves a case whereby the tools have been actually used for engineering purposes.

8.1 Deep reinforced beam

Since the present thesis does not incorporate aggregate interlock and dowel action, we preferred to select a bending problem rather than a shear-critical problem. The choice was fixed on a well-known deep beam that has been tested by Leonhardt & Walther[Leon66]. The beam is subjected to a distributed load and contains a main reinforcing layer at the bottom side. Failure was reported to occur in a ductile manner, due to yielding of the reinforcement in a prominent crack. Indeed, the experiment constitutes an excellent demonstration of localized fracture (Fig. 8.1).

The beam has been analyzed before by e.g. Grootenboer[Groo79], who employed a discrete crack concept and suggested that "a smeared concept is not suitably amenable to simulation of such cases". At that time, it was indeed not yet understood in which way smeared crack concepts are able to produce localization. The purpose of this section is to show that the suggestion is not correct any more and that a strategy of a smeared-crack-predictor with a discrete-crack-corrector provides a reasonable, safe solution.

The finite element mesh is shown in Fig. 8.2. Four-node quadrilaterals have been adopted for the concrete, two-node truss elements for the main reinforcement and four-node lumped interface elements for the bond-slip zone. The stress-strain diagram of the reinforcement[Leon66] was approximated multi-linearly, with hardening starting at a stress of $350N/mm^2$ up to a yield plateau at a stress of $450N/mm^2$. Young's modulus of the reinforcement was $210000N/mm^2$. The concrete parameters have been assumed as: $E=25000N/mm^2$, $\nu=0.2$, $f_{ct}=2.5N/mm^2$, $G_f=100N/mm^2$, crack band width according to Table 4.I, and bond traction-slip curve of Eq. (7.2). The fixed crack concept has been adopted with a shear retention factor $\beta=0.05$, which furnishes a compromise between preventing stress locking and keeping the computation numerically stable, as will be explained afterwards. Following the tension-pull analysis of section 7.2, the tensile strength has been perturbed in order to trigger localization. The perturbation has been applied only to the bottom row of elements, and consequently, it does not bias the analysis in an unfair way.
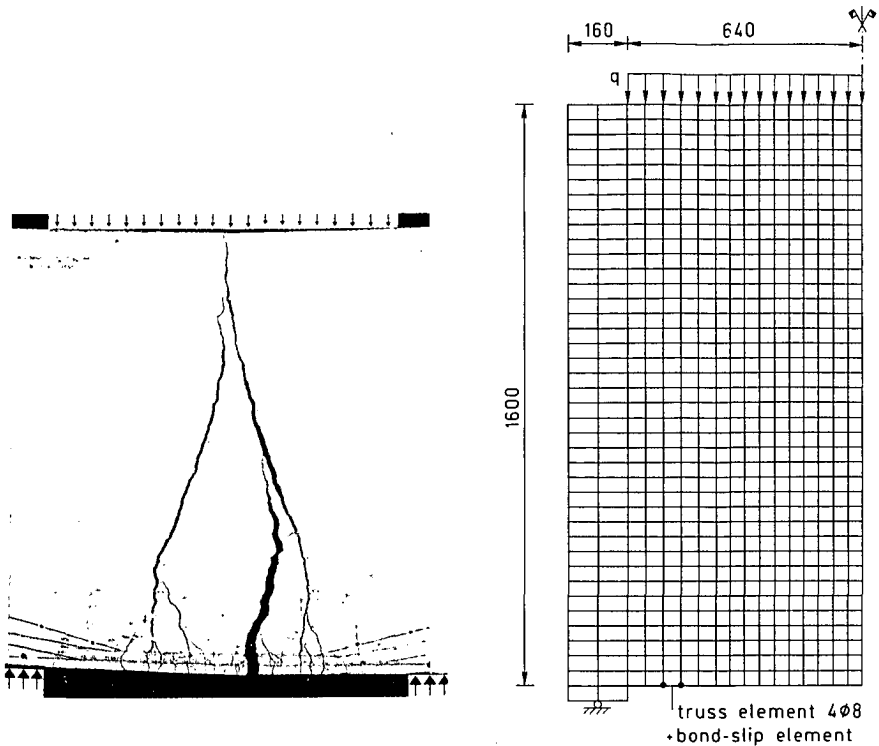
left: Fig. 8.1. Fracture localization in deep beam WT2[Leon 66].

right: Fig. 8.2. Element mesh for smeared crack analysis (dimensions in mm).

Fig. 8.3a shows the crack pattern at the final stage, when the reinforcement has reached its yield plateau. Although a certain degree of diffusion is observed, we clearly distinguish three primary cracks, the middle one of which propagates right through the beam in a manner very similar to the experiment. The diffusion mainly involves spurious cracks with only small crack strains, in the neighborhood of the reinforcement and at places of "zig-zag jumps". This is made evident in Fig. 8.3b, which renders only the full cracks with a crack strain larger than the ultimate strain ε_u^{cr} at softening completion. This figure gives an excellent match of the experimental result. It is concluded that the smeared approach in conjunction with bond-slip inter-face elements is capable of simulating the fracture localization.

Despite the fine mesh, the number of elements along the rebar is small compared to the set-up for the tension-pull analysis in section 7.2. Hence, even though strength perturbations and bond-slip have been included (which significantly promotes locali-zation compared to homogeneous strength and perfect bond), diffuse cracking in the neighborhood of the reinforcement could not be entirely avoided. Consequently,
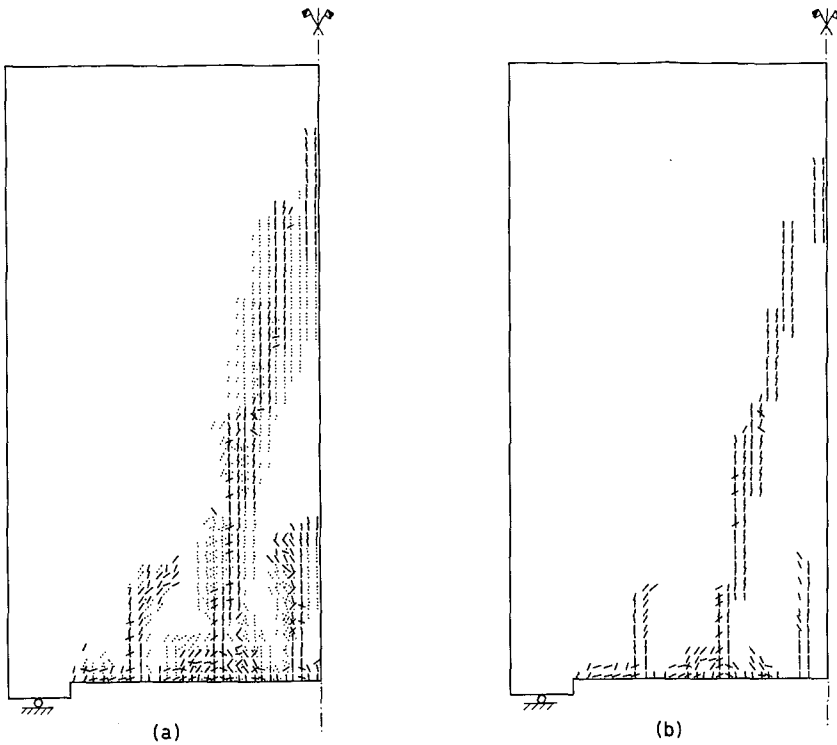
Fig. 8.3. Final crack patterns for smeared-crack-predictor of deep beam.
(a) all cracks, including spurious cracks and arrested cracks
(b) only full cracks, i.e. cracks with $\varepsilon_{nn}^{cr} \geq \varepsilon_{u}^{cr}$ (Fig. 3.1)

above a load level of approximately 60 percent of the ultimate load, multiple negative eigenvalues were found for the tangent stiffness matrix, owing to alternative equilibrium states and associated spurious modes near the reinforcement[Cris 82, Cris 86]. When the coaxial rotating crack concept with implicit shear softening, or the fixed crack concept with zero shear retention is employed, as is ideal according to chapter 6, these problems are magnified because the condition of the stiffness matrix further deteriorates. With the present analysis, (slow) convergence beyond such stages could only be achieved by switching from arc-length control with the proper stiffness matrix to load control with some improper, positive definite stiffness matrix. However, it cannot be proven that the solution then corresponds to the "lowest equilibrium path"[deBo 86], and a possible snap-back may have even been missed.

To investigate the consequences, a discrete-crack-corrector analysis has been made, whereby an arc-length scheme with tangential stiffness could be maintained throughout the entire process. The smeared crack result served as a predictor of the crack path. Only the main primary crack was incorporated, while the other two have
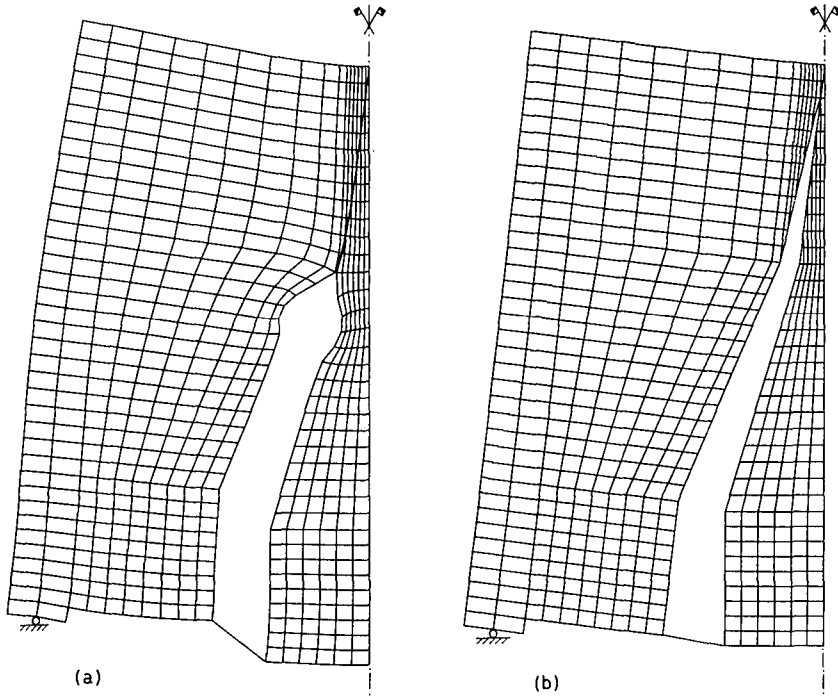
Fig. 8.4. Discrete-crack-corrector analysis of deep beam.
(a) incremental deformations at $q=0.5$N/mm
(b) incremental deformations at final stage when the reinforcement yields

been omitted. Again, bond-slip was included and the parameters were taken the same as above, aside from the shear transfer across the crack which could now be assumed to be zero. The discrete crack propagates in a nice manner, and prior to yielding of the reinforcement the main activity occurs at its tip (Fig. 8.4a). The final configuration (Fig. 8.4b) shows two separated and unloaded blocks that are connected by a yielding reinforcing layer, which correctly resembles the experimental result.

The analysis detected a few, tiny snap-backs during an early loading stage. These snap-backs arose from cracking of the first discrete elements, and were passed by constructing the constraint equation (4.9) from the associated crack tip opening displacement. The corresponding drops in the load, however, were only of the order 0.01 N/mm. These tiny snap-backs were very steep, because the structure is relatively large (the accumulated elastic energy is significant, which implies the size-independent fracture energy to be consumed quickly). Consequently, one cannot even notice them from the load-deflection curve, presented in Fig. 8.5. The conclusion therefore reads that the corrector analysis does *not* detect an important snap-back of a physical nature. This justifies that the beam can be truly loaded until yielding of the reinforcement.

114
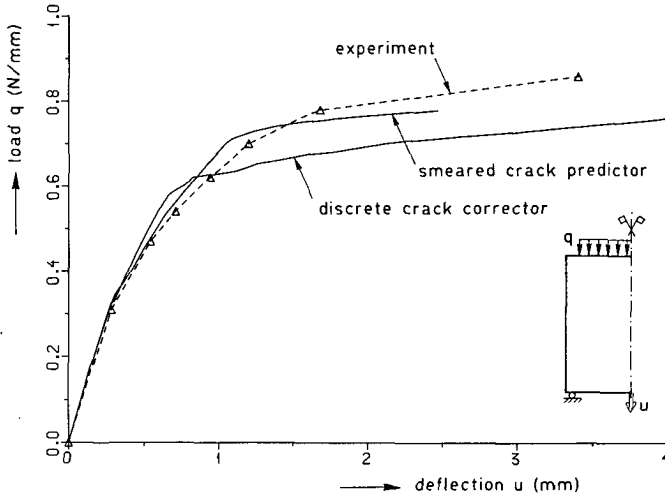
Fig. 8.5. Load versus midspan deflection of deep beam of Fig. 8.1.

The failure load of the smeared crack analysis is 10 percent higher than the failure load of the discrete crack analysis. This suggests that spurious stiffening and stress-locking as imposed by β=0.05 has occurred. The fact that the discrete crack result produces an ultimate load that is 15 percent lower than the experimental failure load may be explained from the fact that (a) the stirr-ups, which were present in the specimen, have not been included in the analysis, (b) aggregate-interlock has been neglected, (c) the hardening diagram adopted for the steel is only an approximation of the true characteristics, (d) the bond-slip curve of (7.2) is conservative. The fact that the smeared crack result fits the experimental result much better must be regarded as a coincidence, since it would be incorrect to claim that the stiffening involved in stress locking constitutes a reliable representation of aggregate-interlock. The discrete crack corrector is essential for providing safe quantitative solutions.

The interesting extension lies in those cases where a structure with dominant reinforcement fractures in a brittle, explosive manner. Gustafsson[Gust 85] is one of the few who has been able to predict a genuine limit load and associated snap-back for such cases. He adopted predefined discrete cracks, in a fashion similar as the present analysis. For smeared cracking, most existing results either show divergence, or continue in an overstiff manner until yielding of the reinforcement.

8.2 Anchorage structure[‡]

The second example concerns the anchorage structure of Fig. 8.6, which consists of a steel plate embedded in a massive concrete block. The steel plate is pulled out of the concrete by a vertical load F which is applied via an anchor bolt. As the structure is unreinforced, diffusion of the crack pattern and the associated difficulties are less likely to occur. The problem has been selected because it illustrates the capabilities of numerical tools to simulate the dangerous, brittle fractures to which traditional design codes do not give a definite answer for they exclude fracture mechanics.
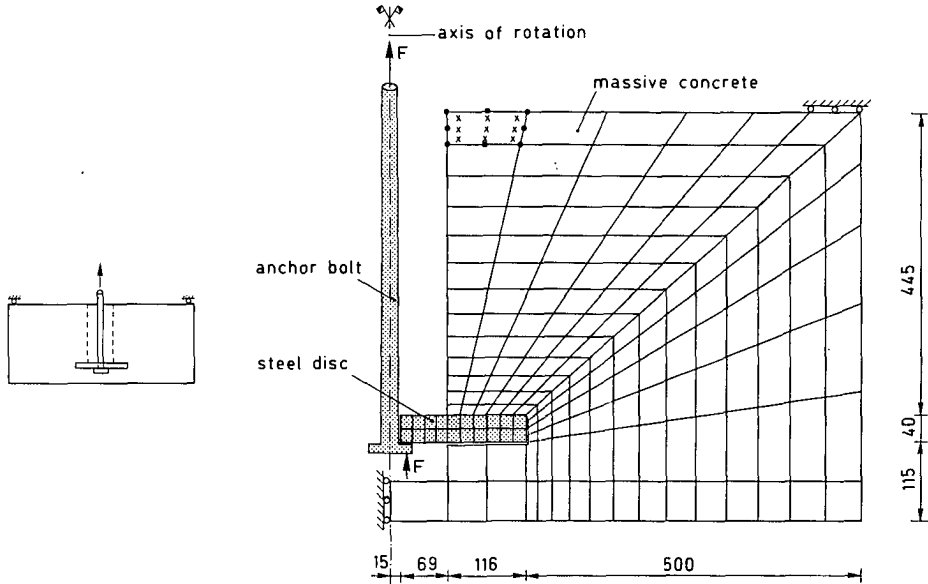
Fig. 8.6. Axi-symmetric finite element idealization of anchorage structure (dimensions in mm).

An axi-symmetric schematization with eight-node elements has been adopted. Although the actual configuration involved an inner tube injected with mortar, this tube has been ignored in the analysis. Hence, the left boundary of the concrete in Fig. 8.6 is unconstrained, which provides a safe assumption. The anchor bolt has been excluded from the analysis, and the load has been directly applied at the bottom of the steel disc. The steel disc has been assumed to be rigidly connected to the concrete only at its top edge, whereas no contact has been assumed along its bottom and side edge. The counterpressure against the pull-out load has been assumed at the upper right corner of the mesh.

---

‡   This study has been originally carried out for Kraftwerk Union AG by TNO-IBBC within a study dedicated to nonlinear analyses of an anchorage for mechanical components. The results are presented by permission of both companies.

The coaxial rotating smeared crack concept has been adopted. The parameters were taken as: $E=30000N/mm^2$, $v=0.2$, $f_{ct}=2.5N/mm^2$, $G_f=100J/m^2$ and linear softening. The crack band width for transverse cracks was taken from Table 4.I. The structure included some reinforcement in the direction normal to the plane of Fig. 8.6. Instead of modeling this reinforcement directly, we preferred to incorporate its effect indirectly, via a somewhat large value $n_l=10$ for the imagined number of localized longitudinal cracks (section 7.1.4). Hence, the crack band width for longitudinal cracks follows from inserting this value into (7.1). The effect of the parameter will be investigated by an additional analysis for $n_l=5$. Preliminary analyses[Rots 85b] showed that the effect of plastic deformation above the steel disc was overruled by the effect of tensile cracking. Nonlinearity in compression has therefore been ignored in the present analysis. The analysis has been performed using the opening displacement over the crack as the control parameter of (4.9).
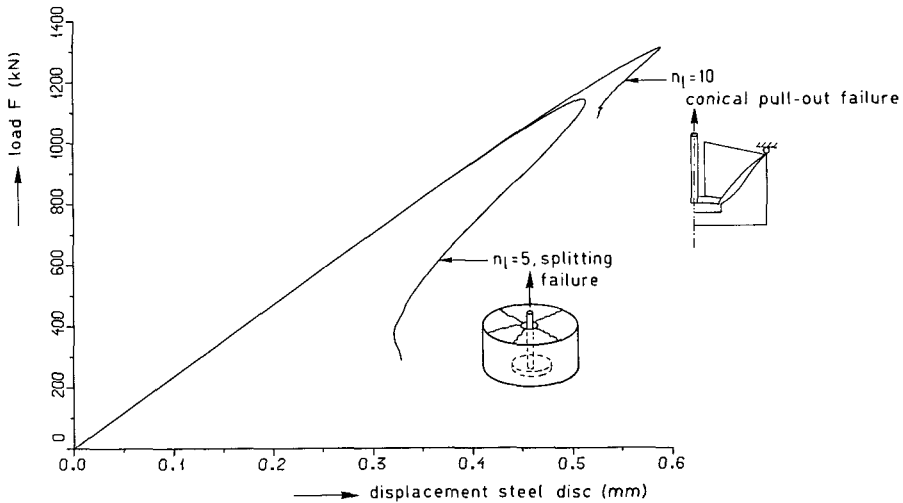
Fig. 8.7. Load F versus vertical displacement of steel disc of anchorage structure.

Fig. 8.7 presents the response in terms of load versus loading point displacement. Prior to the peak, the nonlinearity in the curve is negligible. The peak load occurs very sudden, whereafter a rapid drop of the load is observed. This suggests a dangerous, brittle type of fracture.

Figs. 8.8 and 8.9 confirm the suggestion. These figures show the incremental deformation fields and the crack patterns, both at the peak load and at the residual load of Fig. 8.7. At peak load, the fracture has developed only partially. Beyond peak load it rapidly propagates towards the upper-right corner and shows strong localization in the form of the pull-out of a conical frustum. Fig. 8.9b provides an excellent interpretation of the elastic-softening theory. We observe that the steel disc and the concrete

117
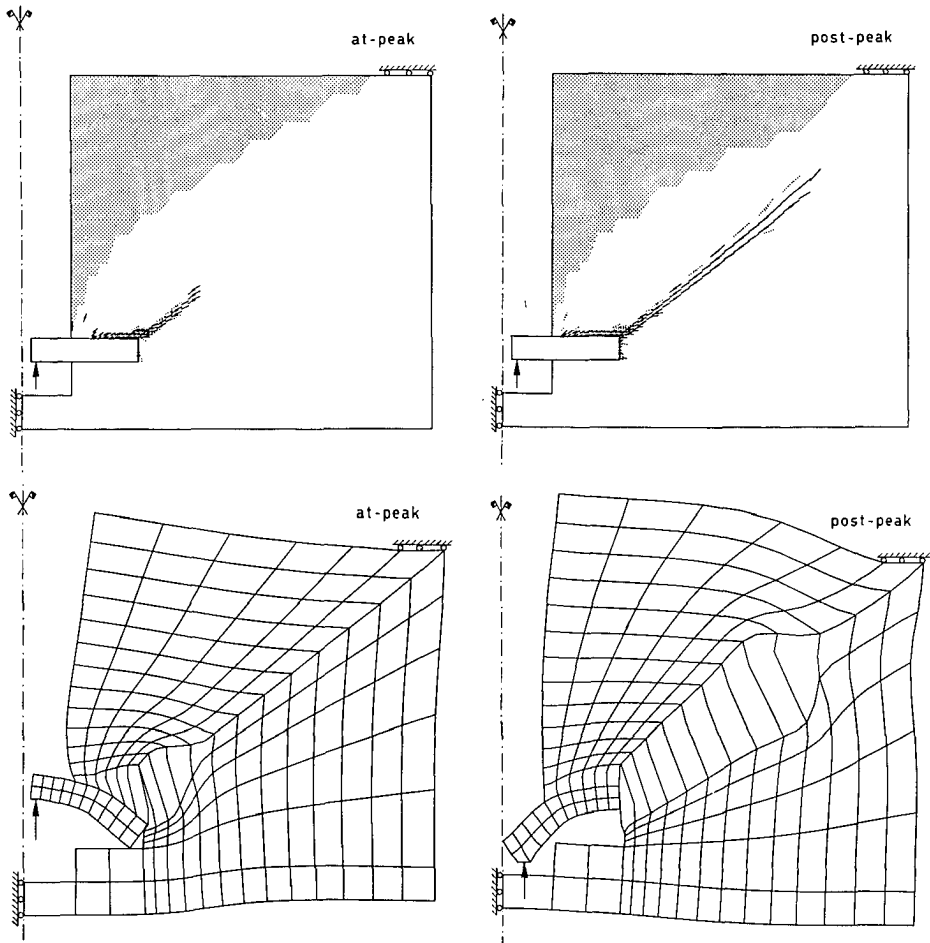
top: Fig. 8.8. Crack patterns at peak load and residual load (longitudinal cracks shaded).
bottom: Fig. 8.9. Incremental deformations at peak load and at residual load.
(the results correspond to the analysis with $n_l = 10$)

that surrounds the fracture surface drastically unload while the fracture propagates, *i.e.*
the available elastic energy stored in the structure at peak load is suddenly released
in the softening for creating the conical fracture surface.

The use of the rotating crack concept provides a reasonable prediction of the ultimate load. This is because the strong stress and strain rotations in the neighborhood of the steel disc are captured with realism. When a fixed crack concept with non-zero shear retention would have been adopted, significant rebuild of the principal tensile stress would have occurred in this area. This would have postponed the fracture, since the decrease of principal tensile stress near the steel disc acts as a nucleus for the

118

catastrophic fracture. Furthermore, the present solution has not been significantly disturbed by locked-in stresses, because the fracture is approximately aligned with the lines of the mesh. The only complication was a spurious kinematic mode that occurred at the residual load level in Fig. 8.7. Fortunately, the behavior beyond this stage was not of interest and the computation was terminated. For these three reasons, a discrete-crack-corrector analysis was not considered to be essential.

The crack patterns of Fig. 8.8 reveal significant longitudinal cracking. It is recalled that the imagined number of *localized* longitudinal cracks in the underlying 3D situation, which determines the crack band width for the *smeared* longitudinal crack in the axi-symmetric simulation, was assumed to be $n_l=10$. With this assumption the predicted extent of longitudinal cracking was not critical and on creating the conical pull-out all existing longitudinal cracks unloaded.

An additional analysis was performed for $n_l=5$, which doubles the crack band width of (7.1) and makes the softening in longitudinal cracking twice as steep. With this analysis the converse occurred as the structure snapped on longitudinal splitting while the conical cracks unloaded. This solution was obtained using the standard constraint equation (4.8), and is included in Fig. 8.7. The snap-back is somewhat less sharp as it is for the pull-out type fracture and the limit load has decreased. The solution could now be continued down to 25 percent of the limit load, at which stage the transverse cracks started to reload and a spurious mode occurred. In analogy to the bond-splitting analysis of section 7.1, further improvements are achieved by a fully 3D analysis which eliminates the uncertainties in the imagined number of n_l.

8.3 Conclusions

Two practical examples of localized fracture have been worked out that illustrate the integrated action of elastic-softening models, crack concepts and computational aspects. The three components have evolved that far that the final outcome is consistent with the essentials of the elastic-softening theory. The examples correctly reveal that the elastic energy stored in a structure is released for creating the fracture surface.

This conclusion holds especially for problems of *un*reinforced concrete, where a variety of dangerous fractures can be simulated, ranging from conical pull-outs to longitudinal splitting. For localized fracture in reinforced concrete the combination of the tools with bond-slip elements has significantly enhanced the numerical possibilities, but difficulties owing to diffusion of the crack pattern and alternative equilibrium states[Cris 82] still exist. A strategy of a smeared-crack-predictor followed by a discrete-crack-corrector leads to safe and converged solutions also for these types of problems.

REFERENCES

Arrea M., Ingraffea A.R., "Mixed-mode crack propagation in mortar and concrete", *Report 81-13*, Dept. Struct. Engng., Cornell Univ., Ithaca, New York (1982)

Balakrishnan S., Murray D.W., "Prediction of response of concrete beams and panels by nonlinear finite element analysis", *IABSE Reports* 54, Coll. Comp. Mech. of Reinforced Concrete, Delft Univ. Press, 393-404 (1987)

Bartos P. (Ed.), *Bond in concrete*, Applied Science Publishers, London (1982)

Bathe K.J., *Finite element procedures in engineering analysis*, Prentice-Hall, New Jersey (1982)

Batoz J.L., Dhatt G., "Incremental displacement algorithms for nonlinear problems", *Int. J. Num. Meth. Engng.* 14, 1262-1267 (1979)

Bazant Z.P., Cedolin L., "Blunt crack band propagation in finite element analysis", *J. Engng. Mech. Div.*, ASCE, 105(2), 297-315 (1979)

Bazant Z.P., Gambarova P., "Rough cracks in reinforced concrete", *J. Struct. Div.*, ASCE, 106(4), 819-842 (1980)

Bazant Z.P., Oh B.H., "Crack band theory for fracture of concrete", *Materials and Structures*, RILEM, 16(93), 155-177 (1983a)

Bazant Z.P., "Comment on orthotropic models for concrete and geomaterials", *J. Engng. Mech.*, ASCE, 109(3), 849-865 (1983b)

Bazant Z.P., Cedolin L., "Finite element modeling of crack band propagation", *J. Struct. Engng.*, ASCE, 109(1), 69-92 (1983c)

Bazant Z.P., Pfeiffer P.A., "Shear fracture tests of concrete," *Materials and Structures*, RILEM, 19(110), 111-121 (1986a)

Bazant Z.P., "Mechanics of distributed cracking" *Appl. Mech. Rev.*, ASME, 39(5), 675-705 (1986b)

Bazant Z.P., Prat P.C., "Measurement of mode III fracture energy of concrete", *Nuclear Engng. and Design* 106, 1-8 (1988)

Beranek W.J., "Experimental techniques for the analysis of deformation", *Documentation-Page* 119, Inst. TNO for Building Mat. and Struct., Delft (1980)

Bergan P.G., "Some aspects of interpolation and integration in nonlinear finite element analysis of reinforced concrete structures", *Computer-Aided Analysis and Design of Concrete Structures* 1, F. Damjanic et al. (Eds.), Pineridge Press, Swansea, 301-316 (1984)

Bhide S.B., Collins M.P., "Reinforced concrete elements in shear and tension" *Publication 87-02*, Univ. of Toronto, Dept. of Civil Engng. (1987)

Blaauwendraad J., Grootenboer H.J., "Essentials for discrete crack analysis", *IABSE Reports* 34, Coll. Advanced Mech. of Reinforced Concrete, Delft Univ. Press, 263-272 (1981)

Blaauwendraad J., "Realisations and restrictions - Application of numerical models to concrete structures" *Finite element analysis of reinforced concrete structures*, Proc. US-Japan Seminar, (Meyer C., Okamura H. Eds.), ASCE, 557-578 (1985)

de Borst R., Nauta P., "Non-orthogonal cracks in a smeared finite element model", *Engng. Computations* 2, 35-46 (1985)

de Borst R., "Non-linear analysis of frictional materials", *Dissertation*, Delft Univ. of Techn. (1986)

de Borst R., "Computation of post-bifurcation and post-failure behavior of strain-softening solids", *Computers & Structures* 25(2), 211-224 (1987a)

de Borst R., "Smeared cracking, plasticity, creep and thermal loading - a unified approach", *Comp. Meth. Appl. Mech. Engng.* 62, 89-110 (1987b)

de Borst R., "Numerical methods for bifurcation analysis in geomechanics", *Ingenieur-Archiv,* in press (1988a)

de Borst R., Blaauwendraad J., "Stability and spurious kinematic modes in strain-softening concrete", *Computational Mechanics '88* 1, S.N. Atluri et al. (Eds.), Springer-Verlag, Berlin (1988b)

Broms B.B, Raab A., "The fundamental concepts of the cracking phenomenon in reinforced concrete beams", *Report 310,* Dept. Struct. Engng., Cornell Univ., Ithaca (1961)

Bruggeling A.S.G., "Structural concrete: Science into practice", *HERON* 32(2), 1-67 (1987)

Budnik J., "Bruch- und Verformungsverhalten harzmodifizierter und faserverstärkter Betone bei einachsiger Zugbeanspruchung", *Dissertation,* Ruhr-Universität Bochum, Bochum (1985)

Carpinteri A., DiTomasso A., Fanelli M., "Influence of material parameters and geometry on cohesive crack propagation", *Fracture Toughness and Fracture Energy of Concrete,* F.H. Wittmann (Ed.), Elsevier Science Publ., Amsterdam, 117-135 (1986)

CEB-FIP Model Code for Concrete Structures, *CEB-FIP* (1978)

Cedolin L., Dei Poli S., "Finite element studies of shear-critical R/C beams", *J. Engrg. Mech. Div.,* ASCE, 103(3), 395-410 (1977)

Cervenka V., "Inelastic finite element analysis of reinforced concrete panels under in-plane loads", *Dissertation,* Univ. of Colorado, Boulder (1970)

Chana P.S., "Investigation of the mechanism of shear failure of reinforced concrete beams" *Mag. of Concrete Research* 39(104), 196-204 (1987)

Cope R.J., Rao P.V., Clark L.A., Norris P., "Modelling of reinforced concrete behaviour for finite element analysis of bridge slabs", *Numerical Methods for Nonlinear problems* 1, Taylor C. et al. (Eds.), Pineridge Press, Swansea, 457-470 (1980)

Crisfield M.A., "A fast incremental/iterative solution procedure that handles 'snap-through'", *Computers & Structures* 13, 55-62 (1981)

Crisfield M.A., "Local instabilities in non-linear analysis of reinforced concrete beams and slabs", *Proc. Inst. of Civil Engineers* 2(73), 135-145 (1982)

Crisfield M.A., "Snap-through and snap-back response in concrete structures and the dangers of under-integration", *Int. J. Num. Meth. Engng.* 22(3), 751-768 (1986)

Crisfield M.A., Wills J., "Numerical comparisons involving different 'concrete-models'", *IABSE Reports* 54, Coll. Comp. Mech. of Reinforced Concrete, Delft Univ. Press, 177-187 (1987)

Cundall P.A., Strack O.D.L., "A discrete numerical model for granular assemblies", *Geotechnique* 29, 47-65 (1979)

Dems K., Mróz Z., "Stability conditions for brittle-plastic structures with propagating damage surfaces", *J. Struct. Mech.* 13(1), 95-122 (1985)

Diamond S., Bentur A., "On the cracking in concrete and fibre-reinforced céments", *Application of Fracture Mechanics to Cementitious Composites,* Shah S.P. (Ed.), Martinus Nijhoff Publ., Dordrecht, 87-140 (1985)

Dodds R.H., Darwin D., Smith J.L., Leibengood L.D., "Grid size effects with smeared cracking in finite element analysis of reinforced concrete", *SM Report 6,* Univ. of Kansas, Lawrence (1982)

Dörr K., "Bond behaviour of ribbed reinforcement under transverse pressure", Final Report *IASS Symp. Darmstadt,* G. Mehlhorn et al. (Eds.), Werner-Verlag, Dusseldorf, Vol. 1, 13-24 (1978)

Dörr K., "Ein Beitrag zur Berechnung von Stahlbetonscheiben unter besonderer Berücksichtigung des Verbundverhaltens", *Dissertation,* Univ. of Darmstadt (1980)

Dragosavić M., "Bond model for concrete structures", *Computer-Aided Analysis and Design of Concrete Structures* 1, F. Damjanić et al. (Eds.), Pineridge Press, Swansea, 203-214 (1984)

Dragosavić M., Groeneveld H., "Concrete mechanics - Local bond", Part I: "Physical behaviour and constitutive consequences", *Report BI-87-18,* Part II: "Experimental research", *Report BI-87-19,* TNO Inst. for Building Mat. and Struct., Delft (1988)

Gambarova P.G., Giuriani E., Discussion of "Study of transfer of tensile forces by bond" by Jiang D.H. et al., *J. Am. Concrete Inst.,* 381-383 (1985)

Gergely P. (Ed.), Proc. ACI Symp. "Interaction between Steel and Concrete", *J. Am. Concrete Inst.* 76(1/2) (1979)

Gilbert R.I., Warner R.F., "Tension stiffening in reinforced concrete slabs", *J. Struct. Div.,* ASCE, 104(12), 1885-1899 (1978)

Gijsbers F.B.J., Hehemann A.A., "Some tensile tests on reinforced concrete", *Report BI-77-61,* TNO Inst. for Building Mat. and Struct., Delft (1977)

Glemberg R., "Dynamic analysis of concrete structures", *Publ. 84:1,* Dept. of Struct. Mech., Chalmers Inst. of Tech., Göteborg (1984)

Goodman R.E., Taylor R.L., Brekke T.L., "A model for the mechanics of jointed rock", *J. Soil Mech. and Foundation Div.,* ASCE, 94(3), 637-659 (1968)

Gopalaratnam V.S., Shah S.P., "Softening response of plain concrete in direct tension", *J. Am. Concrete Inst.* 82(3), 310-323 (1985)

Goto Y., "Cracks formed in concrete around deformed tension bars", *J. Am. Concrete Inst.* 68(4), 244-251 (1971)

de Groot A.K., Kusters G.M.A., Monnier Th., "Numerical modelling of bond-slip behaviour", *HERON* 26(1B), 1-90 (1981)

Grootenboer H.J., "Finite element analysis of two-dimensional reinforced concrete, taking account of nonlinear physical behavior and development of discrete cracks", *Dissertation,* Delft Univ. of Techn. (1979)

Gupta A.K., Akbar H., "Cracking in reinforced concrete analysis", *J. Struct. Engng.,* 110(8), ASCE, 1735-1746 (1984)

Gustafsson P.J., "Fracture mechanics studies of non-yielding materials like concrete", *Rep. TVBM-1007,* Div. Build. Mat., Lund Inst. of Techn. (1985)

Harmsma R.E., Nijhout J.M., "Het gedrag van betonplaten onder explosieve belastingen", *Graduate thesis,* Koninklijke Militaire Academie, Section of Civil Engng., Tilburg (1982)

Hillerborg A., Modeer M., Petersson P.E., "Analysis of crack formation and crack growth in concrete by means of fracture mechanics and finite elements", *Cement and Concrete Research* 6(6), 773-782 (1976)

Hillerborg A., "Results of three comparative test series for determining the fracture energy G_f of concrete", *Materials and Structures,* RILEM, 18(107), 407-413 (1985a)

Hillerborg A., "The theoretical basis of a method to determine the fracture energy G_f of concrete", *Materials and Structures,* RILEM, 18(106), 291-296 (1985b)

Hilsdorf H.K., Brameshuber W., "Size effects in the experimental determination of fracture mechanics parameters" *Application of Fracture Mechanics to Cementitious Composites,* Shah S.P. (Ed.), Martinus Nijhoff Publ., Dordrecht, 361-397 (1985)

Hordijk D.A., Reinhardt H.W., Cornelissen H.A.W., "Fracture mechanics parameters of concrete from uniaxial tests as influenced by specimen length", *Proc. SEM-RILEM Int. Conf. on Fracture of Concrete and Rock,* S.P. Shah and S.E. Swartz (Eds.), SEM, Bethel, 138-149 (1987)

Ingraffea A.R., Gerstle W.H., Gergely P., Saouma V., "Fracture mechanics of bond in reinforced concrete", *J. Struct. Engng.* 110, 871-889 (1984)

Ingraffea A.R., Saouma V., "Numerical modelling of discrete crack propagation in reinforced and plain concrete", *Fracture Mechanics of Concrete,* Sih G.C., DiTomasso A. (Eds.), Martinus Nijhoff Publishers, Dordrecht, 171-225 (1985a)

Ingraffea A.R., Panthaki M.J., "Analysis of 'shear fracture' tests of concrete beams", *Finite element analysis of reinforced concrete structures,* Proc. US-Japan Seminar, (Meyer C., Okamura H. Eds.), ASCE, 151-173 (1985)

Jenq Y.S., Shah S.P., "Mixed-mode fracture of concrete", *Int. J. of Fracture* (1988)

Jiang D.H., Shah S.P., Andonian A.T., "Study of the transfer of tensile forces by bond", *J. Am. Concrete Inst.* 81(3), 251-259 (1984)

Kobayashi A.S., Hawkins M.N., Barker D.B., Liaw B.M., "Fracture process zone of concrete", *Application of Fracture Mechanics to Cementitious Composites,* Shah S.P. (Ed.), Martinus Nijhoff Publ., Dordrecht, 25-50 (1985)

Kollegger J., Mehlhorn G., "Material model for cracked reinforced concrete", *IABSE Reports* 54, Coll. Comp. Mech. of Reinforced Concrete, Delft Univ. Press, 63-74 (1987)

Kolmar W., Mehlhorn G., "Comparison of shear stiffness formulations for cracked reinforced concrete beams", *Computer-Aided Analysis and Design of Concrete Structures* 1, F. Damjanïc et al. (Eds.), Pineridge Press, Swansea, 133-147 (1984)

Kormeling H.A., Reinhardt H.W., "Determination of the fracture energy of normal concrete and epoxy modified concrete", *Rep. 5-83-18,* Stevin Lab., Delft Univ. of Techn. (1983)

Kotsovos M.D., "Effect of testing techniques on the post-ultimate behaviour of concrete in compression", *Materials and Structures* 16(91), 3-12 (1983)

Kupfer H., Hilsdorf H.K., Rusch H., "Behaviour of concrete under biaxial stresses", *J. Am. Concrete Inst.* 66(8), 656-666 (1969)

Labuz J.F., Shah S.P., Dowding C.H., "Experimental analysis of crack propagation in granite", *Int. J. Rock Mech. Min. Sci. & Geomech. Abstr.* 22(2), 85-98 (1985)

Lahnert B.J., Houde J., Gerstle K.H., "Direct measurement of slip between steel and concrete" *J. Am. Concrete Inst.* 974-982, Nov.-Dec. (1986) (1986)

Leibengood L.D., Darwin D., Dodds R.H., "Parameters affecting FE analysis of concrete structures", *J. Struct. Engng.* 112(2), 326-341 (1986)

Leonhardt F., Walther R., "Wandartige Träger", *Deutscher Ausschuss für Stahlbeton* 178, Berlin (1966)

Lin C.S., Scordelis A.C., "Nonlinear analysis of RC shells of general form", *J. Struct. Div.,* ASCE, 101(3), 523-538 (1975)

Litton R.W., "A contribution to the analysis of concrete structures under cyclic loading," *Dissertation,* Univ. of California, Berkeley (1974)

Lorig L.J., Cundall P.A., "Modeling of reinforced concrete using the distinct element method", *Proc. SEM-RILEM Int. Conf. on Fracture of Concrete and Rock,* S.P. Shah and S.E. Swartz (Eds.), SEM, Bethel, 459-471 (1987)

Losberg, A., Olsson P., "Bond failure of deformed reinforcing bars based on the longitudinal splitting effect of the bars", *J. Am. Concrete Inst.* 76(1), 5-18 (1979)

Lutz A.L., Gergely P., "Mechanics of bond and slip of deformed bars in concrete", *J. Am. Concrete Inst.* 64(11), 711-721 (1967)

Martin H., "Zusammenhang zwischen Oberflachenbeschaffenheit, Verbund und Sprengwirkung von Bewehrungsstahlen unter Kurzzeitbelastung", *Deutscher Ausschuss für Stahlbeton* 228 (1973)

Mehlhorn G., Keuser M., "Isoparametric contact elements for analysis of reinforced concrete structures", *Finite Element Analysis of Reinforced Concrete Structures*, (Meyer C., Okamura H., Eds.), ASCE, New York, 329-347 (1985)

van Mier J.G.M., "Strain-softening of concrete under multiaxial loading conditions", *Dissertation*, Eindhoven Univ. of Techn. (1984)

van Mier J.G.M., "Fracture of concrete under complex stress", *HERON* 31(3), 1-90 (1986)

van Mier J.G.M. (Ed.), "Examples of non-linear analysis of reinforced concrete structures with DIANA", *HERON* 32(3), 1-147 (1987)

Milford R.V., Schnobrich W.C., "Numerical model for cracked reinforced concrete", *Computer-Aided Analysis and Design of Concrete Structures* 1, F. Damjanić et al. (Eds.), Pineridge Press, Swansea, 261-273 (1984)

Millard S.G., Johnson R.P., "Shear transfer across cracks in reinforced concrete due to aggregate interlock and to dowel action", *Mag. of Concrete Research* 36(126), 9-21 (1984)

Mirza S.M., Houde J., "Study of bond stress-slip relationships in reinforced concrete", *J. Am. Concrete Inst.* 76, 19-46 (1979)

Ngo D., Scordelis A.C., "Finite element analysis of reinforced concrete beams", *J. Am. Concrete Inst.* 64(14), 152-163 (1967)

Nilson A.H., "Nonlinear analysis of reinforced concrete by the finite element method", *J. Am. Concrete Inst.* 65(9), 757-766 (1968)

Nilson A.H., "Internal measurement of bond-slip", *J. Am. Concrete Inst.* 69, 439-441 (1972)

Nilson A.H. et al. (Eds.), State-of-the-Art Report *"Finite Element Analysis of Reinforced Concrete"*, ASCE, New-York (1982)

Noakowski P., "Die Bewehrung von Stahlbetonbauteilen bei Zwangbeanspruchung infolge Temperatur", *Deutscher Ausschuss für Stahlbeton* 296 (1978)

Oldenburg M., "Finite element analysis of tensile fracturing structures", *Licentiate Thesis 1985:010L*, Lulea Univ. of Techn. (1985)

Onate, E., Oller S., Oliver J., Lubliner J., "A constitutive model for cracking of concrete based on the incremental theory of plasticity", *Computational Plasticity* 2, D.R.J. Owen et al. (Eds.), Pineridge Press, Swansea, 1311-1329 (1987)

Ottosen N.S., Dahlblom O., "Smeared crack analysis using a nonlinear fracture model for concrete", *Numerical Methods for Nonlinear Problems* 3, C. Taylor et al. (Eds.), Pineridge Press, Swansea, 363-376 (1986)

Petersson P.E., "Crack growth and development of fracture zones in plain concrete and similar materials", *Rep. TVBM-1006*, Div. Build. Mat., Lund Inst. of Techn. (1981)

Pruyssers A.F., "Aggregate interlock and dowel action under monotonic and cyclic loading", *Dissertation*, Delft Univ. of Techn. (1988)

Ramm E., "The Riks/Wempner approach - an extension of the displacement control method in nonlinear analyses", *Recent Advances in Non-Linear Computational Mechanics"*, E. Hinton et al. (Eds.), Pineridge Press, Swansea, 63-86 (1982)

Rashid Y.R., "Analysis of prestressed concrete pressure vessels", *Nuclear Engng. and Design* 7(4), 334-344 (1968)

Read H.E., Hegemier G.A., "Strain-softening of rock, soil and concrete - A review article", *Mechanics of Materials* 3, 271-294 (1984)

Rehm G., "On the essentials of bond between concrete and reinforcement", *Deutscher Ausschuss fur Stahlbeton* 138 (1961)

Reinhardt H.W., "Fracture mechanics of an elastic softening material like concrete", *HERON* 29(2), 1-42 (1984)

Reinhardt H.W., Cornelissen H.A.W., Hordijk D.A., "Tensile tests and failure analysis of concrete", *J. Struct. Engng.*, ASCE, 112(11), 2462-2477 (1986)

Riggs H.R., Powell G.H., "Rough crack model for analysis of concrete", *J. Engng. Mech.*, ASCE, 112(5), 448-464 (1986)

Riks E., "An incremental approach to the solution of snapping and buckling problems", *Int. J. Solids and Structures* 15, 529-551 (1979)

Roelfstra P.E., Sadouki H., Wittmann F.H., "La béton numerique", *Materials & Structures* RILEM, 107, 327-335 (1985)

Rokugo K., Ohno S., Koyanagi W., "Automatic measuring system of load-displacement curves including post-failure region of concrete specimens" *Fracture Toughness and Fracture Energy of Concrete*, F.H. Wittmann (Ed.), Elsevier Science Publ., Amsterdam, 403-411 (1986)

Rots J.G., Nauta P., Kusters G.M.A., "Variable reduction factor for the shear stiffness of cracked concrete", *Rep. BI-84-33*, Inst. TNO for Building Mat. and Struct., Delft (1984)

Rots J.G., Nauta P., Kusters G.M.A., Blaauwendraad J., "Smeared crack approach and fracture localization in concrete", *HERON* 30(1), 1-48 (1985a)

Rots J.G., Kusters G.M.A., "Nonlinear finite element analysis of an anchorage structure", *Rep. B-85-145*, Inst. TNO for Building Mat. and Struct., Delft (1985b)

Rots J.G., "Bond-slip simulations using smeared cracks and/or interface elements", *Res. Report 85-01*, Struct. Mech., Dept. of Civil Engng., Delft Univ. of Techn. (1985c)

Rots J.G., "Strain-softening analysis of concrete fracture specimens", *Fracture Toughness and Fracture Energy of Concrete*, F.H. Wittmann (Ed.), Elsevier Science Publ., Amsterdam, 137-148 (1986)

Rots J.G., Hordijk D.A., de Borst, R., "Numerical simulation of concrete fracture in 'direct' tension", Proc. Fourth Int. Conf. *Numerical Methods in Fracture Mechanics*, A.R. Luxmoore et al. (Eds.), Pineridge Press, Swansea, 457-471 (1987a)

Rots J.G., Kusters G.M.A., Blaauwendraad J., "Strain-softening simulations of mixed-mode concrete fracture", *Proc. SEM-RILEM Int. Conf. on Fracture of Concrete and Rock*, S.P. Shah and S.E. Swartz (Eds.), SEM, Bethel, 226-240 (1987b)

Rots J.G., Kusters G.M.A., Blaauwendraad J., "Significance of crack models for bond-slip studies", *IABSE Reports 54*, Coll. Comp. Mech. of Reinforced Concrete, Delft Univ. Press, 121-129 (1987c)

Rots J.G., "Tunnel section", *HERON* 32(3), van Mier J.G.M. (Ed.), 57-67 (1987d)

Rots J.G., de Borst R., "Analysis of mixed-mode fracture in concrete", *J. Engng. Mech.*, ASCE, 113(11), 1739-1758 (1987e)

Rots J.G., de Borst R., "Analysis of concrete fracture in 'direct' tension", submitted for publication (1988)

Schäfer H., "A contribution to the solution of contact problems with the aid of bond elements", *Comp. Meth. Appl. Mech. Engng.* 6, 335-354 (1975)

Schmidt-Thrö G., Stöckl S., Kupfer H., "Influence of the shape of the pull-out specimen and of the arrangement of the slip measurement on the results of pull-out tests", *Deutscher Ausschuss für Stahlbeton* 378, 111-169 (1986)

Schnobrich W.C., Discussion of "Nonlinear stress analysis of reinforced concrete" by Valliapan S. and Doolan T.F., *J. Struct. Div.* ASCE, 98(10), 2237-2328 (1972)

Simons J.W., Bergan P.G., "A finite element formulation of three-dimensional contact problems with slip and friction" *Comp. Mech.* 1(2), 153-164 (1986)

Stevens N.J., Uzumeri S.M., Collins M.P., "Analytical modelling of reinforced concrete subjected to monotonic and reversed loadings", *Publication,* Univ. of Toronto, Dept. of Civil Engng. (1987)

Suidan M., Schnobrich W.C., "Finite element analysis of reinforced concrete," *J. Struct. Div.,* ASCE, 99(10), 2109-2122 (1973)

Tait R.B, Garret G.G., "In situ double-torsion fracture studies of cement mortar and cement paste inside a scanning electron microscope", *Cement, Concr. Res.* 16(2), 143-155 (1986)

Tepfers R., "Cracking of concrete cover along anchored deformed reinforcing bars", *Mag. of Concr. Res.* 31(106), 3-12 (1979)

Valliappan S., Doolan T.F., "Nonlinear stress analysis of reinforced concrete", *J. Struct. Div.,* ASCE, 98(4), 885-897 (1972)

Vecchio F.J., Collins M.P., "The modified compression-field theory for reinforced concrete elements subjected to shear", *J. Am. Concrete Inst.* 83(2), 219-231 (1986)

Vintzeleou E.N., Tassios T.P., "Mathematical models for dowel action under monotonic and cyclic conditions", *Mag. of Concrete Research* 38(134), 13-22 (1986)

Walraven J.C., "Aggregate interlock: a theoretical and experimental analysis", *Dissertation,* Delft Univ. of Techn. (1980)

Vos E., "Influence of loading rate and radial pressure on bond in reinforced concrete", *Dissertation,* Delft Univ. of Techn. (1983)

Willam K., Bićanić N., Sture S., "Composite fracture model for strain-softening and localised failure of concrete", *Computational Modelling of Reinforced Concrete Structures,* Hinton E., Owen D.R.J. (Eds.), Pineridge Press, Swansea, 122-153 (1986)

Willam K., Pramono E., Sture S., "Fundamental issues of smeared crack models", *Proc. SEM-RILEM Int. Conf. on Fracture of Concrete and Rock,* S.P. Shah and S.E. Swartz (Eds.), SEM, Bethel, 192-207 (1987)

de Witte F.C., Nauta P., Kusters G.M.A., *DIANA - Finite Element Method,* Lecture Notes, Inst. TNO for Building Mat. and Struct., Delft (1987)

de Witte F.C. (Ed.), *DIANA User-Manual,* Inst. TNO for Building Mat. and Struct., Delft (1988)

Wittmann F.H., Roelfstra P.E., "Constitutive relations for transient concrete", *IABSE Reports* 54, Coll. Comp. Mech. of Reinforced Concrete, Delft Univ. Press, 239-260 (1987)

Zienkiewicz O.C., *The Finite Element Method,* McGraw-Hill, London (1977)

CURRICULUM VITAE

12 augustus 1958	Geboren te Aalten.
1970-1976	Christelijke Scholengemeenschap te Aalten, afgesloten met Atheneum-B diploma.
1976-1983	Studie Civiele Techniek aan de Technische Universiteit te Delft. Afstudeerwerk lag op het gebied van de betonmechanica en werd uitgevoerd bij het Instituut TNO voor Bouwmaterialen en Bouwconstructies.
1983-heden	Wetenschappelijk medewerker aan de Technische Universiteit te Delft, Faculteit der Civiele Techniek, voor onderzoek van de Stichting voor de Technische Wetenschappen. Sedert 1985 in combinatie met het Instituut TNO voor Bouwmaterialen en Bouwconstructies, afdeling Numerieke Mechanica.

SUMMARY

The numerical modeling of fracture in concrete and similar materials calls for proper crack concepts, constitutive formulations and discretizations as well as a versatile combination thereof. This is the subject of this dissertation. Attention is focused on cases of localized fracture whereby separation prevails over friction.

Chapter 2 categorizes *crack concepts*. After introducing the discrete crack concept that defines potential geometrical discontinuities, an extensive treatment is given of the smeared crack concept that starts from the notion of a continuum. A decomposition of strain permits fixed, multi-directional and rotating smeared crack concepts to be put into one framework. The three variants involve the crack orientation, which is either kept fixed, updated in a stepwise manner or updated continuously. In this way the rotating crack concept is re-interpreted as the limiting case of the multi-directional crack concept with a special provision that enforces coaxiality between principal stress and strain.

Chapter 3 describes *constitutive models*. The assumption of elasticity for the concrete and softening for the crack leads to a transparent formulation. The softening involves the tensile behavior normal to the crack (mode I). For the shear behavior across the crack (mode II) several modifications of the classical shear retention models are put forward. Extensions to cover multi-directional and rotating cracks are outlined. A tension-shear model problem illustrates the performance of the elastic-softening models within the various concepts. The verification is focused on the possibilities to capture stress rotations beyond cracking.

Chapter 4 formulates guidelines for the use of *finite element discretizations* in fracture analysis of softening materials. The implications of element shape, size, orientation, interpolation and integration are investigated. For smeared cracking, attention is given to the danger of locked-in stresses as a consequence of displacement compatibility. Two classes of interface elements for discrete cracking and bond are put forward and verified. Simple interface elements that lump the tractions to the nodes turn out to be superior to advanced elements that distribute the tractions along the interface.

In the remaining part of the thesis, the tools are combined to scrutinize structural fracture in concrete.

Chapter 5 is devoted to uncurved mode I fracture in unreinforced concrete. A new approach towards the research problem of direct tension is presented, which gives rise to a fundamental discussion of the softening phenomenon. A solution is presented to the question of material behavior versus structural behavior in case of non-homoge-

neous deformation during the tensile softening regime. The concave shape of the softening diagram plays an important role. Further insight in the role of the softening parameters is provided by a parametric study of indirect tension problems.

Chapter 6 considers curved mode I fracture in unreinforced concrete. As the lines of the mesh do not coincide with the lines of the fracture, local mode II effects occur. The resulting stress rotations pose strong demands on the crack concept. A surprising conclusion is that from the class of smeared crack concepts only the coaxial rotating concept and the fixed concept with negligible shear retention perform adequately. With the other versions any attempt to build up shear stress along the crack is punished with overstiff behavior. The discrete crack concept with a predefined fracture surface unfolds the ideal solution with genuine separation (discrete-crack-corrector).

In structural practice, designers add reinforcement to compensate for the fracture sensitivity of concrete. Chapter 7 describes numerical tools for simulating bond between concrete and reinforcement. First, the bond is resolved in detail with prime attention to the transverse and longitudinal cracks around a reinforcing bar. This leads to a good, qualitative understanding of traction-slip experiments. Next, the resolved behavior is lumped in an interface element. The combination with softening models for the concrete is able to predict crack spacing and crack width. Thirdly, a brief excursion is made into the field of distributed fracture for diffusely reinforced panels.

The thesis is concluded with two practical examples that integrate the achievements of crack concept, softening behavior and bond. The examples illustrate the possibility of predicting localized fracture in concrete structures.

Major conclusions are:
- A unification of the fixed single, the fixed multi-directional and the rotating smeared crack concept has been accomplished.
- The use of fixed cracks with significant shear retention leads to a dangerous overestimation of strength and stiffness if the stresses rotate. Crack rotation provides a solution, especially when coaxiality between principal stress and strain is imposed.
- In this thesis it has been thoroughly demonstrated that a certain degree of stress-locking cannot be prevented when employing smeared softening models within a finite element discretization. For this reason a discrete-crack-corrector analysis is recommended.
- The discussion of material behavior versus structural behavior in tensile softening has been clarified. The application of elastic-softening models to tensile fracture in heterogeneous materials is justified.
- The research of bond between concrete and reinforcement significantly benefits from the on-going developments in crack concepts and softening models.

SAMENVATTING

NUMERIEKE MODELLERING VAN BREUK IN BETON

De numerieke modellering van breuk in beton en soortgelijke materialen vereist een werkbare combinatie van scheurconcepten (mechanica-raamwerken), constitutieve formuleringen (beschrijvingen van het materiaalgedrag) en discretisatietechnieken (elementen-methoden). Dat is het onderwerp van dit proefschrift. De aandacht gaat met name uit naar vormen van gelocaliseerde breuk waarbij scheiding domineert over afschuiving.

Hoofdstuk 2 katalogiseert *scheurconcepten*. Na de invoering van het discrete scheurconcept met potentiele geometrische discontinuiteiten, volgt een uitvoerige behandeling van het uitgesmeerde scheurconcept dat uitgaat van een continuum-benadering. Een decompositie van de rek maakt het mogelijk gefixeerde, meervoudig gefixeerde en roterende scheurconcepten binnen één kader te plaatsen. De drie varianten hebben betrekking op de scheurrichting, welke respectievelijk constant wordt verondersteld, stapsgewijs wordt bijgesteld of continu wordt bijgesteld. Aldus wordt het gangbare roterende scheurconcept op een nieuwe wijze geïnterpreteerd, als een limietgeval van het meervoudig gefixeerde scheurconcept met een speciale voorziening die coaxialiteit tussen hoofdspanning en hoofdrek vastlegt.

Hoofdstuk 3 beschrijft *constitutieve modellen*. De onderstelling van elasticiteit voor het beton en 'softening' voor de scheur leidt tot een heldere formulering. De softening heeft voornamelijk betrekking op het trekgedrag loodrecht op de scheur (mode I), terwijl voor het afschuifgedrag parallel aan de scheur (mode II) diverse modificaties van de klassieke reductiemodellen worden voorgesteld. De procedures worden uitgebreid ten behoeve van meervoudige en roterende scheuren. Een trek-schuif modelprobleem illustreert de werking van de elastisch-softening modellen binnen de diverse concepten. In de beoordeling wordt gelet op de mogelijkheid spanningsrotaties na scheurinitiatie correct te volgen.

Hoofdstuk 4 formuleert richtlijnen voor het gebruik van *eindige elementen discretisaties* in breukanalyses voor softening materialen. De implicaties van element vorm, afmeting, orientatie, interpolatie en integratie worden onderzocht. Voor uitgesmeerde scheurvorming wordt gewezen op het gevaar van opgesloten spanningen als gevolg van continuiteit in de verplaatsingsen. Ten behoeve van discrete scheurvorming en aanhechting worden twee klassen van grenslaagelementen ten tonele gevoerd en getest. Eenvoudige grenslaagelementen die de krachtsoverdracht concentreren tussen de knopen blijken superieur aan geavanceerde elementen waarbij de kracht verdeeld langs de grenslaag wordt overgedragen.

In het vervolg van dit proefschrift worden de gereedschappen gecombineerd voor een kritisch onderzoek van breuk in betonconstructies.

Hoofdstuk 5 richt zich op rechtlijnige mode I breuk in ongewapend beton. Een nieuwe aanpak van het directe trekprobleem wordt gepresenteerd, welke de aanleiding vormt tot een fundamentele discussie rondom het fenomeen softening. De kwestie van materiaalgedrag versus constructiegedrag bij niet-homogene deformaties gedurende het softening traject wordt opgelost. De concave vorm van het softening diagram speelt daarbij een belangrijke rol. Verder inzicht in de rol van de softening parameters wordt verschaft via een parameterstudie voor indirecte trekproblemen.

Hoofdstuk 6 beschouwt kromlijnige mode I breuk in ongewapend beton. Omdat de lijnen van het elementennet niet overeenstemmen met de lijnen van de breuk, treden locale mode II effecten op. De resulterende spanningsrotaties stellen hoge eisen aan het toe te passen scheurconcept. Een verrassende conclusie is dat van de uitgesmeerde concepten slechts het gefixeerde met een zo laag mogelijke schuifreductiefactor, en het coaxiaal roterende goede prestaties leveren. Bij de overige varianten van het concept wordt iedere poging tot spanningsopbouw langs de scheur afgestraft met overstijf gedrag. Het discrete scheurconcept met een vooraf gedefinieerd breukvlak onthult de ideale oplossing met werkelijke separatie (discrete-scheurcorrector analyse).

In de constructiepraktijk voegt men doorgaans wapening toe ter compensatie van de breukgevoeligheid van het beton. Hoofdstuk 7 is gewijd aan de vereiste numerieke gereedschappen voor de aanhechting tussen wapening en beton. Eerst wordt het aanhechtgedrag in detail ontleed, met bijzondere aandacht voor de transversale en longitudinale scheuren rondom een wapeningsstaaf. Dit leidt tot een goed kwalitatief begrip van experimenten ter bepaling van aanhechtkarakteristieken. Vervolgens wordt het detailgedrag geimplementeerd binnen een grenslaagelement. De combinatie met softening modellen voor het beton is in staat scheurwijdte en scheurafstand correct te voorspellen. Tenslotte wordt nog kort aandacht besteed aan verdeelde breuk bij diffuus gewapende panelen.

Het slothoofdstuk geeft twee voorbeelden waarin de bereikte resultaten van scheurconcepten, softening gedrag en aanhechting geintegreerd zijn. Ze illustreren de mogelijkheid locale breuk in betonconstructies numeriek te voorspellen.

Belangrijke conclusies zijn:
— Een unificatie van het enkelvoudig gefixeerde, het meervoudig gefixeerde en het roterende uitgesmeerde scheurconcept is tot stand gebracht.
— Het gebruik van gefixeerde scheuren met significante schuifstijfheid leidt tot een gevaarlijke overschatting van sterkte en stijfheid indien de spanningen roteren. Scheurrotatie levert een oplossing, vooral wanneer coaxialiteit tussen hoofdspanning en hoofdrek wordt opgelegd.

— In dit proefschrift is grondig aangetoond dat een zekere mate van spannings-opsluiting niet kan worden voorkomen bij de toepassing van uitgesmeerde softeningmodellen binnen een eindige elementen discretisatie. Om deze reden wordt een discrete-scheur-corrector analyse aanbevolen.

— De discussie inzake materiaalgedrag versus constructiegedrag bij softening onder trek is opgehelderd. De toepassing van elastisch-softening modellen voor trekbreuk in heterogene materialen is stellig gerechtvaardigd.

— Het onderzoek van de aanhechting tussen wapening en beton profiteert significant van de voortgaande ontwikkeling van scheurconcepten en softe-ningmodellen.